

https://dspace.org/

Interpretation of aeromagnetic data from the Kuruman Military Area, Northern Cape, South Africa - through the use of structural index independent methods: a description of three depth and structural index inversion techniques for application to potential field data

Whitehead, Robert

2016
http://hdl.handle.net/10539/19305

Downloaded from a DSpace repository. https://dspace.org/

Interpretation of Aeromagnetic Data from the Kuruman Military Area, Northern Cape, South Africa - Through the use of structural index independent methods:

- *A description of three depth and structural index inversion techniques for application to potential field data*

Robert Whitehead



Supervised by Prof. G. R. J., Cooper and Prof. E., Stettler, E.

A dissertation submitted to the Faculty of Science,

University of the Witwatersrand, Johannesburg,

in fulfilment of the requirements for the degree of Master of Science

Johannesburg, 2015

DECLARATION

I declare that this dissertation is my own, unaided work. It is being submitted for the degree of Master of Science in the University of the Witwatersrand, Johannesburg. It has not been submitted before for any degree or examination in any other University.

_____

Robert Cameron Whitehead

____th day of October 2015

ABSTRACT

Three new methods for determining the structural index and source distance for magnetic field data are presented. These methods require only the calculation of the first and second order analytic signal amplitudes of the total field and are applicable to both profile and gridded data. The three methods are first tested on synthetic data and then on two real datasets to test for applicability and repeatability. It was found that each method had different strengths and weaknesses and thus one method cannot be favoured over the others.

Cooper (2014) describes how to calculate the distance to source over both profile and gridded data given a user defined structural index. Often however, particularly in the case of real data, the structural index is not known or varies over the surveyed area. These three new methods however do not require any user input since the structural index is calculated thus making them more applicable to regions of unknown geology.

It was found that the first of the three new methods, the multi-distance inversion method, was best used as an edge-detection filter, since the use of higher order derivatives resulted in increased noise levels in the distance to source calculation. The third of these new methods, the unconstrained inversion method, discussed in Chapter 7, not only solves for the structural index but also determines the depth of the source. In that particular case, the structural index is used as a rejection filter, whereby, depth solutions associated with structural index values outside of the expected range are deemed to be invalid. Unlike the third new method, the first two methods require the distance to source to be calculated via the approach described by Cooper (2014) (which requires the user to define the structural index), the results of which are later rescaled by the calculated structural index to yield what is termed a rescaled distance to source. All three of the new methods are fully automatic and require no user control.

The techniques were first tested on both profile and gridded theoretical data over sources with known structural index values. All of the methods were able to estimate the structural index of each of the particular sources and give depth estimates that varied from the true depth by less than 20 percent (with deeper sources being more inaccurate). Noise was also added to the theoretical data in an attempt to assess how the methods can be expected to perform with real data. It was found that when applied to noisy data, these methods performed equally well to slightly worse, than when the method developed by Cooper (2014) was used.

As a real world case study these three new methods were tested on aeromagnetic data collected over the Kuruman Military Area, Northern Cape, South Africa. Regional deformations as well as later intrusive dykes and cross cutting faults were imaged by the chosen depth determination procedures. The dolerite dykes in the area were found to occur between 20 to 60 m deep. While the sand cover was estimated to be between 30 to 40 m thick. Overall, the techniques yield distance to source estimates that differ by less than 15 m, over sources, to the results obtained by using the source distance method (Cooper, 2014). To test for repeatability a second aeromagnetic dataset, collected over a dyke swarm within the Bushveld Complex, South Africa was considered. Again comparable (less than 15 m over sources) depth estimates were made between the unconstrained and constrained inversions. Since the distance to source estimates produced by these new unconstrained inversion methods are comparable to those produced by constrained inversion (Cooper, 2014) the project can be deemed successful.

Dedicated to my Dad

Robert Francis Whitehead

(28/10/1943 – 16/06/2014)

ACKNOWLEDGEMENTS

This work could not have been possible without the guidance and freedom granted to me by Prof. Gordon Cooper. His ability to simplify the work and present solutions in a simple and clear way is inspiring and I hope to always remember “that the simplest solution is often the best” as I move further into the field of geophysics. He is also thanked for always being available for consultation, be it related to this work or for general career advice.

Golder Associates Pty (Ltd), represented by Prof. Edgar Stettler and Anglo Platinum, represented by Mr. Gordon Chunnet are also thanked for providing the real data used in this work. Prof. Edgar Stettler must also be thanked for kick-starting this MSc. project as well as providing guidance with regards to several of the contract jobs I participated in whilst completing this work.

Finally and most importantly, my heartfelt thanks must be expressed to my family for their continuous support throughout my academic career.

TABLE OF CONTENTS

DECLARATION i
ABSTRACT ii
ACKNOWLEDGEMENTS v
LIST OF FIGURES ix
Chapter 1: Introduction 1
Chapter 2: Derivative Based Depth Determination Methods 4
2.1 Euler Deconvolution 4
2.1.1 Definition of the structural index 4
2.1.2 Euler's homogeneity equation 5
2.1.3 Application of Euler's homogeneity equation 5
2.2 The Tilt-Depth Method 8
2.2.1 Application of the Tilt-Depth method to theoretical contacts 9
2.2.2 Application of the Tilt-Depth method to theoretical dyke models 10
2.2.3 Application of the Tilt-Depth method to gridded data 11
2.3 Discussion on the Tilt-depth Vs Euler Deconvolution Depth Determination Procedures 12
Chapter 3: Analytic Signal Amplitude Based Depth Determination Methods 14
3.1. Depth and structural index determination from known horizontal positions 14
3.2 Distance-Source determination 16
3.3 Note on the calculation of the second order analytic signal amplitude 16
3.4 Calculation of the vertical derivative of the analytic signal amplitude applied to noisy data 21
3.5 Application of the analytic signal amplitude for depth/distance determination 22
3.6 Discussion on the Presented Analytic Signal Amplitude Depth Determination Methods 25
Chapter 4: Estimating the Structural Index - Depth from Extreme Points 27
4.1 Theoretical background of the DEXP method 28
4.2 Application of the DEXP method 30
4.2.1 Application of the DEXP method to profile data 30
4.2.2 Application of the DEXP method to gridded data – Extended DEXP 32
Chapter 5: New Method: Multi-directional distance and structural index determination from analytic signal amplitude variation recorded at two different elevations 35
5.1 Multi-Directional distance inversion - Theoretical background 35

5.2 Application of the multi-directional distance to source method 37

Chapter 6: New Method: Structural index estimation from the analytic signal amplitude fall-off rate 39

6.1 Analytical signal amplitude fall-off - Theoretical background 39

6.2 Application of the analytic signal amplitude fall-off method 40

6.3 The effect of interfering anomalies on the results 43

6.4 The effect of noise in the signal on the results 45

6.5 Improved Euler solutions based on employing the estimated structural index 46

Chapter 7 – Unconstrained depth and structural index inversion, using the variation in distance to source observed from two different elevations 49

7.1 Structural index independent depth determination 49

7.2 Unconstrained structural index determination 50

7.3 Application of the distance to source variation method to theoretical data 50

7.4 The effect of noise on determining the depth to source 51

Chapter 8: Application to Total Magnetic Intensity Data Collected Over the Kuruman Military Area, Northern Cape South Africa (Description of the Geology and Available Geophysical Datasets) 53

8.1 Regional geology of the Kuruman Military Area – The Transvaal Supergroup 53

8.1.1 Nature of ore occurrence 55

8.2 Geophysical datasets pertaining to the Kuruman Military Area 56

8.2.1 Magnetic Data Collection Parameters 56

8.2.2 Interpretation of the TMI data over the primary and secondary blocks 57

8.2.3 Identification of cultural noise in the TMI data 59

8.2.4 Topography of the Kuruman Military Area correlated to the mapped geology 60

Chapter 9: Application of the distance/ depth and structural index determination methods to the TMI data of the Kuruman Military Area, Northern Cape, South Africa 63

9.1 Application of the discussed methods to the Primary Area 63

9.1.1 Distance to source after Cooper (2014) 63

9.1.2 Structural index estimation over the primary region 66

9.2 Application of the discussed methods to the Secondary Area 70

9.2.1 Initial interpretation of the TMI dataset 70

9.2.2 Secondary Area - Calculation of distance to source and rescaled distance to source on profile data 72

9.2.3 Secondary Area - Calculation of distance to source and rescaled distance to source on gridded data 76

9.3 Three dimensional imaging of the magnetic subsurface under the secondary region 83
Chapter 10: Ensuring Repetition of Results 86
10.1 Justification and presentation of second dataset 86
10.2 Distance to source and structural index determination over secondary dataset 87
10.3 Three dimensional subsurface images showing the magnetic depths of the secondary dataset 91
Chapter 11: Conclusions 93
APPENDIX A 98
APPENDIX B 104
REFERENCES 116

LIST OF FIGURES

Figure 2.1 Theoretical structural indices for magnetic data for some simple shapes. All shapes have an infinite strike into and out of the page except for the sphere and vertical cylinder (the 3D shaded bodies). The thin lines from each body indicate the magnetic field lines due to each source Adapted from Durrheim and Cooper (1997). 4

Figure 2.2 Application of Euldph to synthetic data calculated over a vertical contact located at x = 500 m, z = -50 m with a field inclination of -60° , the profile strikes south-north. a) Calculated magnetic anomaly. b) Resultant depth solutions after the application of Euler deconvolution, showing a good clustering around the correct depth locality. A window size of 30 samples and a structural index of 0 were used. 6

Figure 2.3 Application of Euldph to data calculated over a vertical dyke (150 m, 5 m) and a vertical contact (500 m, -30 m) with a field inclination of -60° , the profile runs south-north. a) Calculated magnetic anomaly. b) Resultant depth solutions after the application of Euldph, using a window size of 10 sample points and a structural index of 0 7

Figure 2.4 a) Calculated magnetic field over a contact located at (500 m, -50 m). b) Calculated tilt angle, red lines indicate the ±45° intersections, green lines indicate where the tilt-angle is equal to ±45°. The distance between the green lines is equal to 2 z (twice the depth to the contact). 10

Figure 2.5 Calculated R values over a thin dyke. a) Magnetic field over a thin dyke located at x = 500 m, z = 30 m. b) Horizontal and vertical derivatives. c) Calculated R values (Matlab source code given in Appendix B – Chapter 2)..... 11

Figure 2.6 Application of the Tilt-Depth method to gridded data. a) Data was calculated over a vertical prism located at a depth of 10 m. b) The tilt angle is given with the -45°, +45° and 0° contours overlain. The depth of the contact is given by calculating the perpendicular distance between the -45° and +45° contours 12

Figure 3.1 Difference between theoretical and calculated upward continued components of the Analytic Signal Amplitude. a) Difference between upward continued horizontal gradient (dx) and theoretical value of dx at the upward continued height. b) Difference between upward continued vertical gradient (dz) and theoretical value of dz at upward continued height. c) Difference between upward continued analytic signal amplitude (As) and theoretical value of As at upward continued height. 19

Figure 3.2 Difference between the analytic signal amplitude at the lower datum and at the higher datum. Note the negative values either side of the peak. 20

Figure 3.3 Vertical derivative of the analytic signal amplitude derived by upward continuing each component of the analytic signal amplitude compared to upward continuing the analytic signal amplitude. The results are compared to the analytic derivation (black line). 20

Figure 3.4 Calculation of the vertical derivative of the analytic signal amplitude over a thin dyke via three different methods. First via the theoretical expression for the derivative (given in black), secondly by upward continuing each of the components of

the analytic signal amplitude (given in red), lastly by upward continuing the analytic signal amplitude (given in green) before applying the finite difference method. 22

Figure 3.5 Application of the analytic signal amplitude depth determination method to profile data following Cooper (2014). a) Calculated magnetic field for model shown in red. b) Forward model (in red) and calculated distance/depth solutions. Cooper (2014) - solid lines, Euler solutions – crosses 23

Figure 3.6 Application of the method proposed by Cooper (2014) to gridded data. a) Calculated magnetic field over a 100 m by 100 m magnetic prism with infinite depth extent at a depth of 5 m with a magnetic field inclination of -60° and a declination of 30°. b) Calculated distances to source, overlaid with magnetic prism boundary (black line) 24

Figure 3.7 Application of the method proposed by Ma and Du (2012). a) Magnetic field over a vertical dyke located at (300 m, 17 m) with a magnetic field inclination of 60° and a declination of 0°. b) First order analytical signal amplitude. c) second order analytical signal amplitude. d) Ratio of the first and second order analytical signal amplitudes. (Adapted from Ma and Du (2012)) 24

Figure 3.8 Resultant depth and structural index after the application of the method proposed by Ma and Du (2012) plotted against distance from the known horizontal position of the source. a) Estimated depth of the source (true depth 17 m). b) Estimated structural index of the source (true value 1)..... 25

Figure 4.1 Simplified representation of the depth from extreme points method. The local maxima within the 3D volume is located at (x,y,z) while the source (indicated in black) is located at (x_0, y_0 and z_0). (x,y,z) and (x_0, y_0 and z_0) are symmetric about the x-y plane as indicated by the dotted line. 27

Figure 4.2 log(f 1)+log(z) as a function of observation height (z) for fixed values of z 0 (5m, 10m, 15 m) calculated directly over the source (x = x_0, y = y_0). The function reaches a maximum value where z = -z_0 . f 1 is calculated from equation 4.1..... 29

Figure 4.3 Application of the DEXP method over a dyke located at x_0 = 500 m z_0= 30 m with a local field inclination of -90°. The top subplot shows the total magnetic field as a function of upward continuation height for the profile. The bottom function shows the scaled output after using a scaling exponent of 0.5 (appropriate for a dyke). The white dot indicates the position of the maximum of the scaled output and is located at (x = 503 m, z = 30 m). 31

Figure 4.4 Application of the DEXP method to non-RTP data. Scatter points represent the position of the maximum in the scaled outpoint after applying the appropriate scaling exponent. As input the total field, the vertical derivative and the analytic signal amplitude were used. The structural index was first assumed to be equal to 1 and then equal to 0.The closest grouping (red green and blue dots) occurred when a structural index of 1 was assumed (appropriate for a dyke). 32

Figure 4.5 Summary of the workflow procedure implemented when applying the extended DEXP method to gridded data. 33

Figure 4.6 Application of the extended DEXP method to solve for the structural index and depth to source over three synthetic sources. Column 1: Magnetic field, structural index and depth to source calculated over a contact. Column 2: Equivalent values calculated over a dyke. Column 3: Equivalent values calculated over a point source. The contact was located at a depth of 10 m whilst the dyke and point source are located at a depth of 20 m. RTP-source was used..... 34

Figure 5.1 Multi-directional distance to source and structural index estimation over a thin (5 m) vertical dyke and contact located at a depth of 20 m. a, b) Calculated magnetic field over the dyke and contact. c, d) Estimated structural index values with the contour line of $R_h = 0$ overlaid. e, f) Rescaled distance to source estimations. 37

Figure 6.1 Conceptual application of the analytic signal fall-off rate method applied to contacts. a, b, c: The total magnetic field, the analytic signal amplitude and the distance to source of the contact located at a depth of 30 m respectively. d, e f: The total magnetic field, the analytic signal amplitude and the distance to source of the contact located at a depth of 20 m respectively. g Structural index estimation. The local magnetic field inclination was set at -60° and the declination was set to 0° . For both distance to source estimates a structural index of 0 was used. 41

Figure 6.2 Conceptual application of the analytic signal fall-off rate method applied to two vertical (5 m thick) dykes. a, b, c: The total magnetic field, the analytic signal amplitude and the distance to source of the dyke located at a depth of 30 m respectively. d, e f: The total magnetic field, the analytic signal amplitude and the distance to source of the contact located at 20 m depth respectively. g Structural index estimation. 42

Figure 6.3 Estimation of the structural index over both a contact (a) and a dyke (b) located at a depth of 20 m by making use of the analytic signal fall-off method. An upward continuation height of 5 m was used between the two data elevations. 42

Figure 6.4 Rescaled distance to source and structural index estimation for gridded data over a contact and dyke. a) Rescaled distance to source over a contact located at 20 m below the surface. b) Estimated structural index over the contact (true N = 0). c) Corrected distance to source over a dyke located at a depth of 20 m. d) Estimated structural index over the dyke (true N=1). The local inclination was set to -70° with a declination of 0° 43

Figure 6.5 Rescaled distance to source estimations over two contacts separated by 500m. The local field inclination and declination were set to -80° and 0° respectively. a) Calculated magnetic field. b) The distance to source via the analytic signal amplitude based method (Cooper, 2014) is given in black for comparison. c) Filtering was based on rejecting distance to source solutions associated with calculated structural index values outside of the range of [0, 3]. The thick black line shows the outline of the two contacts. 44

Figure 6.6 Rescaled distance to source estimations over two contacts separated by 100m. The local field inclination and declination were set to -80° and 0° respectively. a) Calculated magnetic field. b) Rescaled distance to source estimations, the distance to

source via the analytic signal amplitude based method (Cooper, 2014) is given in black for reference. c) Filtered rescaled distance to source estimations. 45

Figure 6.7 The effect of adding 0.1% random noise to the calculated two contact model previously discussed. The corrected distance to source (given in a) after applying the filtering (given in b) based on the structural index (valid solutions in the range 0 to 3) clearly shows two clusters roughly around the true location of the 46

Figure 6.8 Euler deconvolution using calculated structural index values. a) the calculated magnetic field over a magnetic dyke located at a depth of 15 m and a contact located at a depth of 30 m with a local magnetic field inclination of -90°. b) Variation of the estimated structural index along the profile using Equation 4. c) Euler solutions using a window length of 12 samples, black crosses – convention Euler deconvoulution using a structural index of 0, red crosses - Euler solutions based on calculated structural indices for the profile (given in b). The black lines indicate the outlines of the bodies. 47

Figure 6.9 Semi-automatic and automatic Euler deconvolution applied to theoretical gridded data. a) Structural index estimation over the corner of an infinite prism located at a depth of 30 m with a field inclination of -80°. b) Automatic Euler solutions showing moderate to tight clustering around the edge of the prism. c) Euler solutions generated with an assumed structural index of 1. d) Euler solutions generated with an assumed structural index of 0. The outline of the body is given in black whilst magnetic field of the prism is shown in the background in gray. 49

Figure 7.1 Application of the variation in distance to source method over a thin dyke located at a depth of 20 m. a) magnetic field with an inclination and declination of - 60° and 0° respectively over the dyke. b) non-filtered depth of source. c) structural index variation with acceptable structural index values contained within the dotted lines. d) filtered depth solutions (filtering based an rejection of depth solutions associated with structural index values outside of the range of 0 to 3), shown in black, and distance to source (Copper, 2014), shown in blue (calculated with a structural index of 1). 51

Figure 7.2 The effect of adding random 0.02% noise to the model previously discussed. The blue line indicates the distance to source estimate using the method proposed by Cooper (2014) with a structural index value of 1 (appropriate for a dyke). The black line indicates the unconstrained unfiltered depth solutions obtained by making use of equation 4. 52

Figure 8.1 Simplified geology of the Transvaal Supergroup. Deposition of the Transvaal group occurred in the Transvaal basin to the east, whilst in the west it occurred in the Griqualand basin, division into the two basins occurred along the north south trending Lobatse arch. The boundary of the Kuruman Military Area is given in red (Cairncross et al. 1997). S, D, P show the locations of Sishen, Dimoten syncline and Postmasburg respectively while the dotted line indicates the Maremane dome axis. ... 54

Figure 8.2 Geological map of the region indicating the extent of the western (red block) and eastern (green block) manganese belts. Geological map obtained from the Council of Geosciences, South Africa, (2014). 55

Figure 8.3 Total magnetic intensity map of the Kuruman Military Area, overlain on the geological map of the region, showing the location of the two survey blocks, namely the primary and secondary blocks. 56

Figure 8.4 a) Occurrence of slump structures that host the economic Blinkklip and Wolhaarkop breccias that form part of the Manganore deposits (given in red on the geology map). b) Total magnetic intensity map of area indicated by the black rectangle, showing two north east trending dykes as well as scattered circular to semicircular features associated with the Manganore deposits. c) Geological map of the region under discussion, with the Manganore deposits given in red. d) satellite image of the region, showing circular topographic highs in association with the mapped geology (Google Earth, 2014). 59

Figure 8.5 The electric railway line connecting Sishen to Saldahna causes considerable localised noise. In the secondary region this is clearly seen by the high frequency noise in the TMI data directly along the path of the railway line. 59

Figure 8.6 Shuttle Radar Topography Mission (SRTM) data of the region. The primary region of the Kuruman Military Area is outlined in black. 60

Figure 8.7 Surface elevation with the geology overlaid for the primary region. The outline of the primary region is given in black. Geological map obtained from the Council of Geosciences, South Africa (2014). 61

Figure 8.8 Elevation of the secondary region, data was collected in-flight through the use of a Optech/King laser altimeter. Several liner features can be identified that correlate to features on the TMI image of the region (Identified with black arrows). 62

Figure 9.1 Distance to source estimation calculated via the method proposed by Cooper (2014) assuming all sources have a structural index of 1. The data was upward continued by 60 m prior to the calculation to reduce the effect of high frequency noise which was later subtracted from the output. 63

Figure 9.2 Distance to Source estimations over the two most prominent north south striking dykes in the primary region. The location of this figure with respect to the survey block is indicated in Figure 9.1 by the dashed box. 65

Figure 9.3 Structural index values estimated by making use of the analytic signal fall-off method over the primary region of the Kuruman Military Area, South Africa. 66

Figure 9.4 Structural index values estimated by making use of the extended DEXP method over the primary region of the Kuruman Military Area, South Africa. 67

Figure 9.5 Depth image over the primary region using the non-constrained inversion method (presented in Chapter 7). 68

Figure 9.6 R h calculated over the primary region delineating the complex nature of the dyke swarms over the Maramane dome. Solutions in excess of 30 m were rejected. 69

Figure 9.7 Total magnetic intensity (TMI) recorded over the secondary area, showing N-S, NW-SE and NE-SW propagating dyke swarms (1), paleo-river channel (2) and cultural noise due to an electric railway line (3). 70

Figure 9.8 Geology map of the secondary region showing the mapped lithology and occurrence of dolerite dykes, drainage systems and cultural features. The outline of the secondary area given in black (map obtained from the Council of Geosciences). 71

Figure 9.9 Location of the extracted profiles used for calculating the distance to source and the rescaled distance to source. A structural index of 1 was assumed for the distance to source method while the structural index was calculated by making use of the analytic signal fall-off method to rescale the distance to source. .. 72

Figure 9.10 Profile 1 extracted from the secondary area. a) TMI (blue) and upward continued TMI (red). b) Distance to source using a structural index of 1 (blue) and the distance to source using the calculated structural index (red). c) calculated structural index..... 73

Figure 9.11 Profile 2 over the secondary area. a) TMI (blue), and upward continued TMI (red). b) Distance to source using a structural index of 1 (blue) and the distance to source using the calculated structural index (red). c) Calculated structural index 73

Figure 9.12 Inverse modelling of profile 1. The observed magnetic field is given by the dashed green line, while the modelled response is given in black. The depth of the dykes was set to the calculated values given by the distance to source method (Cooper, 2014) with a structural index of 1. The dykes all had a thickness of 2 m, with the susceptibility (S.I) of each of the dykes given alongside the appropriate dyke. 75

Figure 9.13 Inverse modelling of profile 2. The observed magnetic field is given by the dashed green line, while the modelled response is given in black. The depth of the dykes was set to the calculated values given by the distance to source method (Cooper, 2014) with a structural index of 1. The dykes all had a thickness of 2 m, with the susceptibility (S.I) of each of the dykes given alongside the appropriate dyke. 75

Figure 9.14 Distance to source over the secondary area calculated using a structural index of 1. The black outline indicates the boundary of the recent sand cover, estimated depths are deeper in this area. 76

Figure 9.15 Estimated structural index values over the secondary area. Values calculated by making use of the analytic signal fall-off method. Calculated structural index values outside of the range of 0 to 3 were rejected and shaded in grey. 77

Figure 9.16 Rescaled distance to source over the secondary area. Although there is an increase in noise levels the overall distance to source trends are preserved. 78

Figure 9.17 The absolute difference between the distance to source with a structural index of 1 and the rescaled distance to source (with the structural index calculated by the analytic signal fall-off method) over the secondary area. On average the absolute difference is less than 30 m between the two methods over the dykes. 79

Figure 9.18 Filtered depth of magnetic sources contained within the secondary region. Filtering was based on rejecting depth solutions associated with structural index values outside of the range of [0, 3]. 80

Figure 9.19 Structural index estimation over the secondary area after the application of the extended DEXP method. Values less than 0 or greater than 3 were rejected and shaded in grey. 81

Figure 9.20 Rescaled distance to source over the secondary area using structural index values calculated by making use of the extended DEXP method. 82

Figure 9.21 The absolute difference between the distance to source assuming a structural index of 1 and the rescaled distance to source (with the structural index calculated by the extended DEXP method) over the secondary area. Significant variation in the depth of the dykes is observed under the sand cover where the structural index is poorly estimated due to increased noise. 82

Figure 9.22 R h calculated over the secondary region. R_h tends to 0 directly over the multiple dykes present in the region. 83

Figure 9.23 Location of subset of the secondary region used for calculating the 3D surface images of the magnetic subsurface. 84

Figure 9.24 Three dimensional images of the magnetic subsurface under the southern portion of the secondary region. a) 3D plot showing the depth of the magnetic dykes calculated by making use of the distance to source method after Cooper, (2014) with N=1. b) Rescaled distance to source after scaling the distance to source by the structural index calculated by making use of the analytic signal fall-off method. c) Depth of magnetic bodies calculated by the non-constrained inversion method presented in Chapter 7. 85

Figure 10.1 Total magnetic intensity image over part of the Bushveld Complex, South Africa. 86

Figure 10.2 Distance to source calculated using a structural index of 1 over part of the Bushveld Complex, South Africa. The resultant image is equivalent to that found in Cooper, (2014). 87

Figure 10.3 Structural index image produced by making use of the analytic signal fall-off method (Chapter 6) dykes in the Bushveld Complex, South Africa. Structural index values outside of the range of [0, 3] were considered to be invalid and rejected (shaded in grey on the image). 88

Figure 10.4 Rescaled distance to source after scaling the distance to source by the structural index values calculated by making use of the analytic signal fall-off method over dykes in the Bushveld Complex, South Africa. 89

Figure 10.5 Depth to source calculated by making use of the non-constrained inversion method (Chapter 7) over dykes in the Bushveld Complex, South Africa. 90

Figure 10.6 R_h values calculated over dykes in the Bushveld Complex, South Africa clearly delineating the magnetic dykes in the area. 90

Figure 10.7 Three dimensional images of the magnetic subsurface under part of the Bushveld Complex, South Africa. a) 3D plot showing the depth of the magnetic dykes calculated by making use of the distance to source method after Cooper, (2014) with N=1. b) Rescaled distance to source after scaling the distance to source by the structural index calculated by making use of the analytic signal fall-off method. c) Depth of

magnetic bodies calculated by the non-constrained inversion method presented in Chapter 7. 92

Chapter 1: Introduction

The purpose of any geophysical survey is to gain a better understanding of the geology of a particular area. In the case of potential field applications, data is collected in the field and later interpreted, through modelling, to account for the local geology. Two types of modelling exist, namely forward and inverse modelling. Forward modelling calculates the response over a theoretical body which is representative of the expected geology. The forward model is calculated prior to the survey being conducted and aides in survey planning (station and line spacing, line orientation etc.) to optimize the process of data acquisition in the field. The inverse model is constructed post-survey and attributes the measured data to a geological model of the region. Due to non-uniqueness inherent in potential field data, resultant inverse models often need to be constrained by local geological knowledge if they are to have real world significance.

There exist multiple mathematical procedures that aid the modeller in constructing a first pass interpretation of the subsurface geology. For magnetic data inversion (such as that described in this dissertation) these methods are often based on describing the measured data by an arrangement of theoretical sources such as poles and dipoles. This is done through a factor referred to as the structural index of the source. The structural index describes the source shape and the fall-off rate of the total field with distance from that source. Hence care must be taken in choosing the correct structural index to describe the causative body. Traditionally, solving for the structural index during the inversion process is a complex task and is difficult to implement (Cooper, 2006) and hence is not often done.

There exist several depth determination methods that make use of the first order derivatives of the measured total magnetic field, for example the well known Euler homogeneity approach and the less commonly used Tilt-Depth method (Salem et al., 2007). Recent developments by Ma and Du (2012) and Cooper (2014) provide simple to implement techniques that invert for the source-depth without the users input if the structural index of the source is known / assumed.

A simple structural index determination procedure, the depth from extreme points (extreme points being local maxima) (DEXP) method has been proposed by Fedi (2007). The DEXP method involves the construction of a three dimensional scaled (where the values at each datum have been multiplied by a constant i.e. linear scale) volume above the source where the scaling function applied to the data is dependent on the height of

observation, the structural index of the source and the dataset used (E.g. the analytic signal amplitude, vertical derivative of the field etc.) (Fedi, 2007). Local maxima within this constructed volume are then symmetric about the x-y plane with the location of the source beneath the surface. Under the correct choice of structural index, local maxima within the volume will occur in the same location irrespective of the choice of input dataset, however if the incorrect structural index is selected then the maxima, calculated from different datasets, will be more disperse (Fedi, 2007).

So while there already exist methods for determining the structural index of a source and another set of methods for determining the depth of the source, any method that attempts to solve for both, as stated before, is generally complex and so not usually implemented. One of the aims of this project was to formulate a simple to use technique that could solve for the structural index and depth of the source. The other aim of this project was to asses if the aforementioned technique can be used on real data and to compare its results with the results given by implementing the depth determination traditional methods.

Three new methods for determining the structural index for potential field data are presented (Chapters 5, 6 and 7). All three methods rely on analysing the field at a minimum of two different elevations. Data need not be acquired on two elevations however since, through the process of upward continuation, data recorded on one level can be transformed into what would be expected had the data been acquired at a higher level. The first of these methods simultaneously solves for the structural index and each of the three principle directions (namely x, y and z) to the source. However due to the higher order derivatives used and associated increase in noise levels it was found that this method is best used as an edge-detection filter. The second method calculates the analytic signal fall-off rate between the two data elevations. Again due to higher order derivatives noise levels in the data need to be minimal. The advantage of the method is that it produces a structural index map of the region and is not constrained to non-remnantly magnetised bodies. The third method is based on assessing the difference in distance to source estimations between the two data elevations, directly over the body, hence invalid solutions are obtained away from the body and hence the need for filtering. The third method varies from the previous two in that the structural index is not needed to determine the depth of the source in any manner but is rather used as a filter to identify these valid solutions. The estimated structural index values from the first two methods can be used as input into the structural index dependant method for determining the distance to source (Cooper, 2014) thus providing more accurate depth estimates, in areas

where the structural index is not known. In the third method the depth of the source is determined independently of the structural index, thus there is no need for this correction. Whilst each of the three methods presented are progressively more easily applicable and more stable than the previous each has specific advantages over the others and so are all presented for discussion.

The above methods were tested on real data collected over the Kuruman Military Area, Northern Cape, South Africa. The region is composed of rocks of the Transvaal Supergroup and hosts vast reserves of iron and manganese ore that are of significant economic importance to South Africa. The airborne data were collected as part of a ground water project over two survey blocks, namely the Primary and Secondary regions. For the Primary region the data were only available on a 125 m grid spacing thus the estimated distance/depth to the magnetic sources was only representative of the regional geology and structures. Regional deformation of the area is an important factor that aided in upgrading and preserving the economic reserves of the region. The raw data were available for the secondary region, thus the data were gridded on a 20 m grid spacing yielding significantly more detailed results compared to the primary region. Of interest in the Secondary region is the imaging of a preserved ancient river channel, formed by the deposition of localised banded ironstones along the river bed. The depth of this ancient river channel was determined by making use of the depth / distance determination methods and was found to be ~ 60 m deep. There are also several dolerite dykes in the region that occur both exposed and under later sand cover. By noting the apparent increase in depth of these dykes as they propagate beneath the sand cover, an estimate of the thickness of the sand cover can be calculated (found to be between 30 and 40 m thick).

In Chapter 2 the traditional first order derivative based methods that attempt to solve for the location of the source are presented. This is followed by, in Chapter 3, a discussion about the distance to source methods developed by both Ma and Du (2012) and Cooper (2014). Chapters 5, 6, and 7 present the three new methods for determining the structural index and the distance / depth of the source. In Chapter 8 a brief geology of the Kuruman Millitary Area, South Africa is given as well as a discussion of the available aeromagnetic datasets. Chapters 9 and 10 describe the performance of the aforementioned methods to the aeromagnetic data from both the Kuruman Military area and the Bushveld Complex, South Africa. Final conclusions are presented in Chapter 11.

Chapter 2: Derivative Based Depth Determination Methods

2.1 Euler Deconvolution

2.1.1 Definition of the structural index

The fall-off rate of potential fields describes the attenuation of the measured field with distance from the source, and was first explicitly used in the field of geophysics by Smellie (1956). The structural index describes this fall-off rate due to theoretical sources, such as magnetic poles and dipoles (Briener, 1973, Thompson, 1982, Grauch et al., 2006). The basic premise is that the magnetic anomaly measured over a magnetic source can often be equivalent to the theoretical anomaly derived from a simple shaped magnetic body such as a monopole (Smellie, 1956). Furthermore, a distribution of magnetic poles or dipoles has a characteristic fall off rate with distance where the measured field f at a point (x, y, z) due to such an arrangement is given by (Thompson, 1982).

$$f(x, y, z) = \frac{M}{r^N} \tag{2.1.1}$$

where M is the maximum magnetic field strength of the source, r is the distance to the source and N is the structural index describing the source.

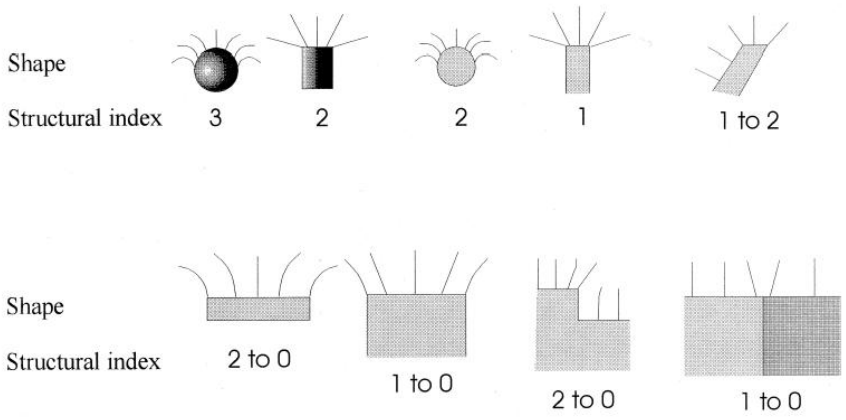


Figure 2.1 Theoretical structural indices for magnetic data for some simple shapes. All shapes have an infinite strike into and out of the page except for the sphere and vertical cylinder (the 3D shaded bodies). The thin lines from each body indicate the magnetic field lines due to each source Adapted from Durrheim and Cooper (1997).

2.1.2 Euler's homogeneity equation

The relationship between the measured field, the structural index and the location of the source is given by Euler's homogeneity equation (equation 2.1.2). That is any function $f(x, y, z)$ is said to be homogeneous of degree N if the following relation is satisfied (Thompson, 1982), where N is an integer:

$$f(tx, ty, tz) = t^N f(x, y, z) \tag{2.1.2}$$

where t is a proportionality factor. In theory measured fields around both magnetic and gravity sources are homogeneous. Furthermore it can be shown that if the function; $f(x, y, z)$ is homogenious of order N, then the following relationship holds (Thompson, 1982):

$$x\frac{\partial f(x,y,z)}{\partial x} + y\frac{\partial f(x,y,z)}{\partial y} + z\frac{\partial f(x,y,z)}{\partial z} = Nf(x, y, z) \tag{2.1.3}$$

where, in the case of potential field data, x, y and z are the two horizontal distances and the vertical distance to the source respectively and $\frac{\partial f}{\partial x}, \frac{\partial f}{\partial y}$ and $\frac{\partial f}{\partial z}$ are the horizontal and the vertical derivatives of the measured field respectively.

2.1.3 Application of Euler's homogeneity equation

In general the structural index is defined by the user and the x, y and z positions of the source are solved for in a least squares sense from data contained within a moving window of user selected size. This is the approach used in the original Euler deconvolution method described by Thompson (1982) used for profile data and by Reid (1990) for map data. However later developments of the method have allowed for the structural index to be solved for concurrently with the position (Mushayandebvu et al., 2001), though these methods are often difficult to apply since the inversion processes is computationally quite extensive (Cooper, 2006).

Thompson (1982) developed a procedure termed Euldph to perform Euler deconvolution on a measured signal. This procedure considers data from within a moving window and

performs least squares inversion to solve for the location of the source under the assumption of a certain structural index. The window is then moved one station spacing along the profile and the procedure in then repeated. The final result after the entire profile has been considered are clusters of location solutions with the tightest grouping of solutions representing the most likely location of the source.

The Euldph method was applied to theoretical profile data to ascertain its ease of use and stability of solutions (Matlab code in Appendix B). The method was applied to a forward model calculated over a contact located midway along a 1000 m long profile at a depth of 50 m. The contact was modelled with a susceptibility of 0.01 (S.I.). The magnetic field inclination was -90^o and the profile was orientated in a south-north direction perpendicular to the strike of the contact with a station spacing of 1 m. A window of 30 samples was used together with a structural index of 0 ($N = 0$, appropriate for a contact). Figure 2.2a shows the calculated magnetic field whilst the calculated location solutions are given in Figure 2.2b. The solutions show good clustering near the true location of the contact.

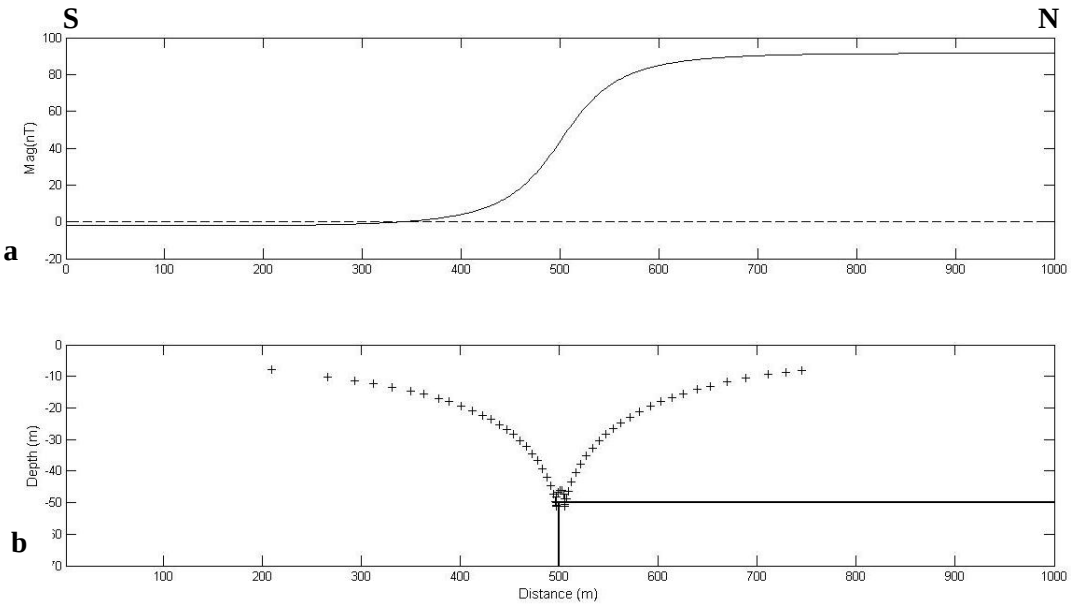


Figure 2.2 Application of Euldph to synthetic data calculated over a vertical contact located at x = 500 m, z = -50 m with a field inclination of -60^o, the profile strikes south-north. a) Calculated magnetic anomaly. b) Resultant depth solutions after the application of Euler deconvolution, showing a good clustering around the correct depth locality. A window size of 30 samples and a structural index of 0 were used.

Since real data, more often than not, contains multiple sources of different types, the anomalous field over a vertical dyke located at 150 m, at a depth of 5 m and a vertical contact located at 700 m, at a depth of 30 m was then calculated (Figure 2.3a). The susceptibility of both the contact and the dyke was set to 0.01 (S.I.), while the profile was again orientated south-north perpendicular to the strike of the bodies. A local inclination and declination of -60^0 and 0^0 respectively were used together with a station spacing of 1 m. A structural index of 0 was used in calculating the Euler solutions with a window size of 10 samples, which resulted in a good clustering of solutions around the correct location of the contact whilst the solutions related to the location of the dyke were more disperse (most likely due to using a too large window size) and located at a depth of approximately half the true depth. The poor depth estimation around the dyke is due to the incorrect structural index being employed. Care must therefore be taken in choosing the correct window size (usually smaller than half the expected width of the source (Thompson, 1982)) and structural index for individual anomalies when applying this method to obtain optimal results.

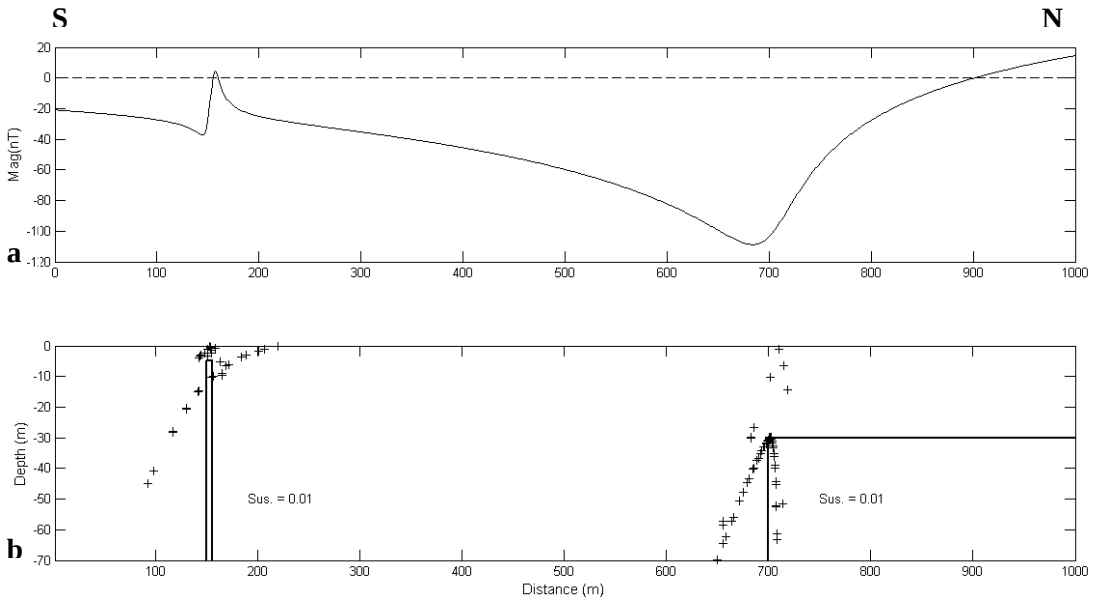


Figure 2.3 Application of Euldph to data calculated over a vertical dyke (150 m, 5 m) and a vertical contact (500 m, -30 m) with a field inclination of -60^o, the profile runs south-north. a) Calculated magnetic anomaly. b) Resultant depth solutions after the application of Euldph, using a window size of 10 sample points and a structural index of 0.

2.2 The Tilt-Depth Method

Another method for determining the location of magnetic sources was developed by Salem et al. (2007) and termed the Tilt-Depth method. This method utilises the ratio of the vertical derivative of the magnetic anomaly to the total horizontal derivative, hence the Tilt-Depth is independent of the local magnetic field strength, declination and susceptibility of the body (Salem et al., 2007) since such terms are common to both derivatives. This transformation behaves in a similar way to an automatic gain control filter where small amplitude anomalies are given equal weighting to larger ones (Salem et al., 2007) thereby increasing noise levels.

For contact models the vertical and horizontal derivatives of the anomalous field are given by (Nabighain, 1972):

$$\frac{\partial M}{\partial x} = 2KFC\sin(d)\frac{(z-z_0)\cos(\beta)+(x-x_0)\sin(\beta)}{(x-x_0)^2+(z-z_0)^2} \qquad (2.2.1)$$

$$\frac{\partial M}{\partial z} = 2KFC\sin(d)\frac{(x-x_0)\cos(\beta)-(z-z_0)\sin(\beta)}{(x-x_0)^2+(z-z_0)^2} \qquad (2.2.2)$$

where, F is the magnetic field strength of the inducing field, K is the susceptibility contrast of the source, $\frac{\partial M}{\partial x}$ and $\frac{\partial M}{\partial z}$ are the horizontal and vertical derivatives of the measured anomaly respectively, $\beta = 2I - d - 90^{\circ}$ with $I = \text{atan}(\tan(i)/\cos(A))$, and $C = 1 - cos^2 I \sin^2 A$, where i is the inclination of the field, A is the angle between the positive x axis and magnetic north, and d is the dip of the contact. $(x,\ z)$ is the point of observation of the field and $(x_0,\ z_0)$ are the coordinates of the source.

Taking the ratio of the vertical to the horizontal derivative (Equation 2.2.2 divided by Equation 2.2.1) of the measured anomaly gives:

$$\frac{\frac{\partial M}{\partial z}}{\frac{\partial M}{\partial x}} = \frac{(x-x_0)\cos(\beta)-(z-z_0)\sin(\beta)}{(z-z_0)\cos(\beta)+(x-x_0)\sin(\beta)} \qquad (2.2.3)$$

This eliminates terms describing the susceptibility of the body, local magnetic field strength and orientation of the profile. Assuming that the magnetisation direction is vertical ($I = 90^{\circ}$) and that the dip of the contact is vertical (I.e.$\beta = 0^{\circ}$) equation 2.2.3 simplifies to (Salem et al, 2007):

$$\frac{\frac{\partial M}{\partial z}}{\frac{\partial M}{\partial x}} = \frac{(x - x_0)}{(z - z_0)} \tag{2.2.4}$$

As an image processing filter Miller and Singh (1994) defined the tilt angle as the arctangent of the ratio of the vertical to horizontal derivative of the magnetic signal:

$$\text{tilt angle} = \tan^{-1}\left[\frac{\frac{\partial M}{\partial z}}{\frac{\partial M}{\partial x}}\right] \tag{2.2.5}$$

Therefore substituting equation 2.2.4 into equation 2.2.5 yields,

$$\text{tilt angle} = \tan^{-1}\left[\frac{(x - x_0)}{(z - z_0)}\right] \tag{2.2.6}$$

Therefore for positions directly above the vertical contact i.e. $(x - x_0) = 0$, the tilt angle is equal to 0° and for positions where the point of observation is a horizontal distance away from the source equal to the depth of the source ($(x - x_0) = (z - z_0)$) the tilt angle is equal to ±45° Hence for vertical contacts with vertical magnetisation direction (I.e. RTP data) and no remanence both the position and depth of the contact can be found from the tilt angle alone (Salem et al., 2007) by measuring the distance between the appropriate tilt angle values.

2.2.1 Application of the Tilt-Depth method to theoretical contacts

The Tilt-Depth method was applied to synthetic RTP data (refer to code in Appendix B) calculated over a vertical contact located 500 m along a 1000 m profile at a depth of 50 m. The Matlab source code used for this calculation is given in Appendix B – Chapter 2 of this dissertation and was developed by the author. The results after the application of the Matlab program to the theoretical data are shown in Figure 2.4. A calculated position of 500 m and a depth of 48.4 m were obtained after determining the distance between the -45°, +45° and 0° tilt angle positions, this is in good agreement with the actual value of 50 m.

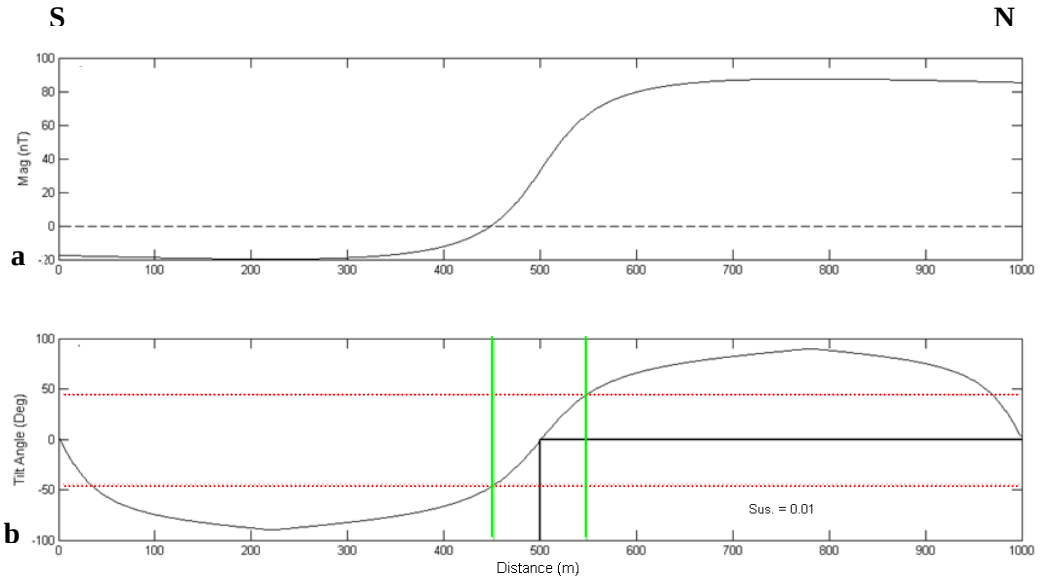


Figure 2.4 a) Calculated magnetic field over a contact located at (500 m, -50 m). b) Calculated tilt angle, red lines indicate the ±45° intersections, green lines indicate where the tilt-angle is equal to ±45°. The distance between the green lines is equal to 2z (twice the depth to the contact).

2.2.2 Application of the Tilt-Depth method to theoretical dyke models

Cooper (2012) describes the application of the Tilt-Depth method to vertical magnetic dyke anomalies. Instead of using the tilt angle Cooper (2012) makes use of the ratio, R, of the vertical to horizontal derivatives of the field alone. The depth of the dyke is then given by half of the distance between the $R = 0$ intercepts. While the location of the dyke is given where *R* tends to infinity.

As an example, *R* was calculated from synthetic data calculated over a thin (5 m) vertical dyke located 500 m along a 1000 m long profile, at a depth of 30 m, in accordance with the method proposed by Cooper (2012) with a local field inclination of -90°. The results are shown in Figure 2.5. A position and depth of 500 m and 29.9 m were obtained for the dyke, again this is in good agreement with the actual values. The code for this example can be found in Appendix B – Chapter 2.

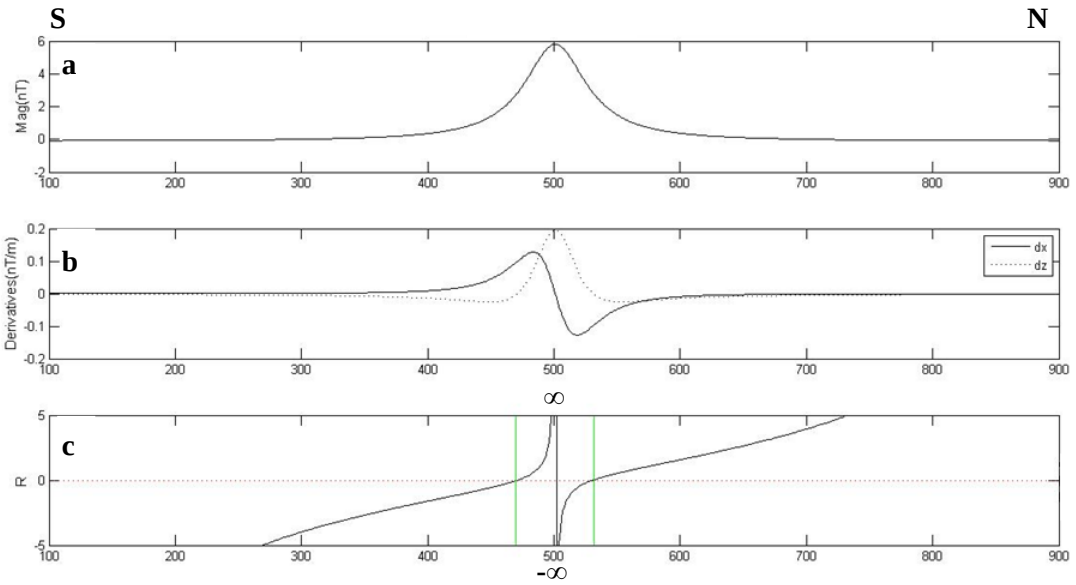


Figure 2.5 Calculated R values over a thin dyke. a) Magnetic field over a thin dyke located at x = 500 m, z = 30 m. b) Horizontal and vertical derivatives. c) Calculated R values (Matlab source code given in Appendix B – Chapter 2).

2.2.3 Application of the Tilt-Depth method to gridded data

The horizontal location and depth of different sources can also be calculated for gridded data by making use of the tilt angle for gridded data, given by (Miller and Singh, 1994):

$$T = \tan^{-1}\left[\frac{\frac{\partial M}{\partial z}}{\sqrt{\left(\frac{\partial M}{\partial x}\right)^2 + \left(\frac{\partial M}{\partial y}\right)^2}}\right] \qquad (2.2.7)$$

where the denominator contained within the arctangent term has been expanded to include the derivatives in both horizontal directions (namely the x and y directions). For gridded data the resultant of applying this operator is a contour map (Figure 2.6). Half the distance between $\pm 45^0$ contours yields the depth while the location of the 0^0 contour traces out the location of the source. The majority of the computation time taken, when applying the Tilt-Depth method to gridded data, is spent calculating the correct distances

between contours, a complex task when applied to multiple cross-cutting bodies since it would often be done by hand or require the employment of contouring software.

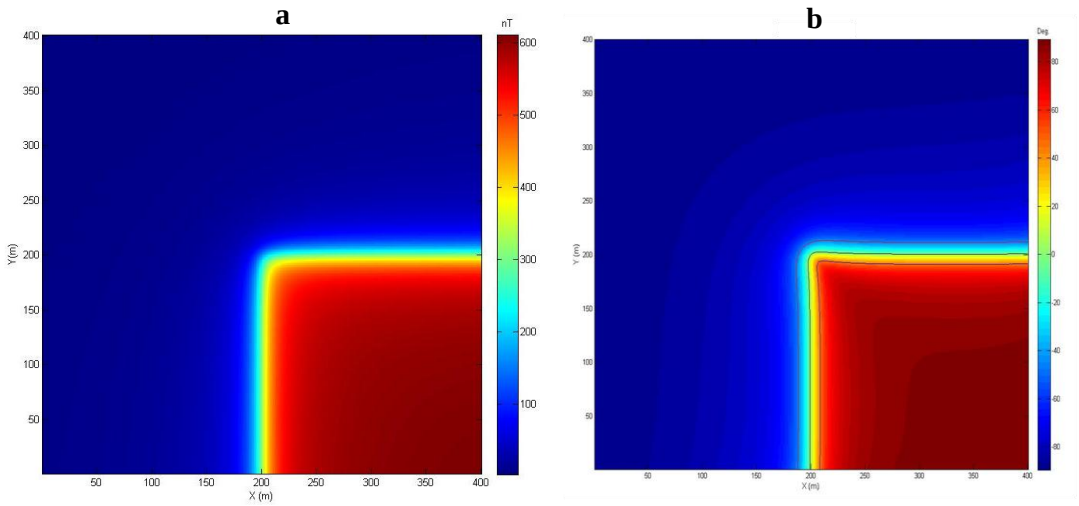


Figure 2.6 Application of the Tilt-Depth method to gridded data. a) Data was calculated over a vertical prism located at a depth of 10 m. b) The tilt angle is given with the -45°, +45° and 0° contours overlain. The depth of the contact is given by calculating the perpendicular distance between the -45° and +45° contours.

2.3 Discussion on the Tilt-depth Vs Euler Deconvolution Depth Determination Procedures

Estimating the location of the source based on either Euler deconvolution or the tilt-depth method yields results that need further interpretation. For example, Euler deconvolution through the Euldph implementation or similar approach leads to a spray of values in the solution space. Evaluation of this solution space to obtain correct solutions based on either clustering or similar filtering procedures is required, with the criteria being subjective at best. Furthermore, multiple iterations of Euler deconvolution need to be implemented if the structural index of the source is unknown. The tightest grouping, defined through some criteria, of solutions from these multiple iterations will then identify the correct choice of structural index. Determining the correct structural index in this way is avoided if extended Euler deconvolution is applied, however depth solutions still need to be identified. Lastly different solutions can be obtained if the user makes use of a different window sizes in the inversion process (Thompson, 1982) as was identified in the multiple source example given above. Euler deconvolution is applied to the

measured total magnetic intensity (TMI) and derivatives thereof hence not requiring transformation of the dataset (such as pole reduction) and no limitations are made on the source orientation or source type, making the method widely applicable.

The Tilt-Depth method is computationally simple, however the assumptions that the data are pole reduced and that the causative body has a vertical dip makes the true application of the method limited. After calculation of the tilt angle, the depth is calculated by measuring the distance between specific contours which can be a complex task (for example for gridded data with multiple intersecting and interfering bodies). The Tilt-Depth method does not require a moving window and inversion unlike Euler deconvolution hence the results do not depend on user defined parameters such as window size and choice of inversion procedure.

A simple and widely applicable depth determination procedure that can be simply applied to the whole dataset without the need for additional user input, such as defining a window size (as in the Tilt-Depth method) and can be applied to data without limitations made about the source (as in Euler deconvolution) is thus still needed.

Chapter 3: Analytic Signal Amplitude Based Depth Determination Methods

Unlike Euler deconvolution and the tilt-depth method the following two methods, depth from known points (Ma and Du, 2012) and the source-distance method (Cooper, 2014) generate depth / distance results that do not require further user interpretation. They are presented here as they form the framework of the newly developed methods presented later.

3.1. Depth and structural index determination from known horizontal positions

There exist other methods for determining the location of the source that require less user input and control than either Euler deconvolution or the tilt-depth method, however they still require that the source type (the structural index) to be known. For completeness, two methods based on the first and the second order analytic signal amplitude are therefore presented. Salem et al. (2004) defines the analytic signal, As, for profile data, as:

$$As = \frac{k}{((x - x_0)^2 + (z - z_0)^2)^{(N+1)/2}} \tag{3.1}$$

where k is a constant related to the magnetisation of the source, N is the structural index of the source and $(x - x_0)$ and $(z - z_0)$ are the horizontal and vertical distances to the source respectively. Using the analytic signal amplitude in depth determination methods is advantageous since equation 3.1 shows that the positional terms are independent of the inclination, and dip of the body. Taking the horizontal and vertical derivatives of equation 3.1 gives (Appendix A, Ma and Du, 2012):

$$\frac{\partial As}{\partial x} = k\frac{(N+1)((x - x_0))}{((x - x_0)^2 + (z - z_0)^2)^{\frac{N+3}{2}}} \tag{3.2}$$

$$\frac{\partial As}{\partial z} = k\frac{(N+1)((z - z_0))}{((x - x_0)^2 + (z - z_0)^2)^{\frac{N+3}{2}}} \tag{3.3}$$

Furthermore, defining the second order analytic signal, As_2, by equation 3.4 and substituting the derivatives given in equations 3.2 and 3.3 into equation 3.4 gives equation 3.5 (Ma and Du, 2012).

$$As_2 = \sqrt{\left(\frac{\partial As}{\partial x}\right)^2 + \left(\frac{\partial As}{\partial z}\right)^2} \tag{3.4}$$

$$As_2 = k\frac{(N+1)}{((x-x_0)^2+(z-z_0)^2)^{(N+2)/2}} \tag{3.5}$$

Taking the ratio of equation 3.5 to equation 3.1 gives:

$$\frac{As_2}{As} = \frac{(N+1)}{((x-x_0)^2+(z-z_0)^2)^{\frac{1}{2}}} \tag{3.6}$$

thereby eliminating terms describing the inducing magnetic field in much the same was as is presented in the discussion of the Tilt-Depth method (Salem et al., 2007).

Equation 3.6 shows how the ratio of the second order analytic signal amplitude to the analytic signal amplitude is only dependant on the structural index and the location of the source. Ma and Du (2012) solve for the depth to the source and structural index of the source explicitly by noting that for positions directly above the source $(x-x_0)=0$ the ratio reduces to:

$$\frac{As_2}{As}\Big|_{x=x_0} = \frac{(N+1)}{((\mathrm{z}-\mathrm{z}_0)^2)^{\frac{1}{2}}} \tag{3.7}$$

Taking two positions, one directly above the source and another a horizontal distance a from the source, the depth to the source z can be solved for explicitly (Ma and Du, 2012):

$$z = \sqrt{\frac{(a)^2}{\left(\frac{\frac{As_2}{As}\Big|_{x=0}}{\frac{As_2}{As}}\right)^2 - 1}} \tag{3.8}$$

Positions directly above the source are given (profile data) by the maximum position of the analytic signal amplitude (Ma and Du, 2012). Furthermore if the reciprocal of the squares of equations 3.6 and 3.7 are calculated and the latter subtracted from the former the structural index can be solved for independently of the depth to the source (Ma and Du, 2012) and is given by:

$$\mathrm{N} = \sqrt{\frac{(\mathrm{a})^2}{\left(\frac{\mathrm{As}}{\mathrm{As}_2}\right)^2 - \left(\frac{\mathrm{As}}{\mathrm{As}_2}\Big|_{(\mathrm{x}-\mathrm{x}_0)=0}\right)^2}} - 1 \tag{3.9}$$

Further investigation of Equations 3.8 and 3.7 illustrates why this methodology can only be applied to profile data. For positions $x=-a$ and $x=a$ from the source, equal depths and structural index estimations will only be obtained if the first and second order

analytic signal amplitudes are equal at those positions. That is, the analytic signal amplitude needs to be symmetrical about the maximum, whilst this is always the case for profile data, the analytic signal amplitude of gridded magnetic data retains a component of the magnetisation direction resulting in an asymmetric signal (Ma and Du, 2012). Furthermore, if the analytic signal amplitude was assumed to be symmetric for gridded data, the task of finding appropriate evaluation positions perpendicular to the strike of the body is a complex task similar to finding the correct distance between contours in the application of the Tilt-Depth method (Salem et al., 2007), which has already been noted as unattractive.

3.2 Distance-Source determination

Since the distance R between the source $(x_0,\ z_0)$ and the measurement point (x, z) is given by $R = \sqrt{(\mathrm{x} - \mathrm{x}_0)^2 + (\mathrm{z} - \mathrm{z}_0)^2}$ Cooper (2014) rearranges equation 3.6 into:

$$R = \frac{(N+1)As}{As_2} \tag{3.10}$$

Equation 3.10 is then directly applied to both profile and gridded data. Furthermore since R is the distance to the source, local minima values of R , by definition, will be located directly above the source with a value equal to the depth of the top of the body. The shortcoming of this method is that the user needs to define the structural index of the source prior to its application. The incorrect choice of structural index will lead to a static shift in the estimated distance to source. However apart from the structural index, no other assumptions need to be made about the source or inducing field (Cooper, 2014) (as is true in the application of Euler deconvolution). Furthermore no complex analysis of the results needs to be done since the correct depth solutions are identified by local minima on the resultant profile or image.

3.3 Note on the calculation of the second order analytic signal amplitude

Since the analytic signal is not a harmonic function (Florio et al., 2006, Ma and Du, 2012, Cooper, 2014) calculating the vertical derivative of the analytic signal through methods such as the fast Fourier transform is not technically valid. Florio et al. (2006) propose two different methodologies to account for this when working out the second order analytic signal amplitude. The first method is through the calculation of the vertical derivative of the analytic signal analytically, this approach is used by Cooper (2014). The second

method involves upward continuing (using the fast Fourier transform i.e. in the frequency domain) the analytic signal by a finite distance subtracting this elevated analytic signal amplitude from the original and dividing by the upward continuation height. The second approach is used by Ma and Du (2012).

To derive the analytical expression for the second order analytical signal amplitude (as used by Cooper 2014) the first order analytic signal is firstly defined as (Nabighian, 1972):

$$As = \sqrt{\left(\frac{\partial f}{\partial x}\right)^2 + \left(\frac{\partial f}{\partial y}\right)^2 + \left(\frac{\partial f}{\partial z}\right)^2} \tag{3.11}$$

where $\frac{\partial f}{\partial x}$, $\frac{\partial f}{\partial y}$ and $\frac{\partial f}{\partial z}$ are the horizontal and vertical derivatives of the measured signal respectively. This is in contrast to the structural index dependant expression of the first order analytic signal amplitude presented in Equation 3.1.

Again the second order analytic signal amplitude is defined as the analytic signal of the analytic signal and hence the grid equivalent of equation 3.4 is given by (Cooper, 2014):

$$As_2 = \sqrt{\left(\frac{\partial As}{\partial x}\right)^2 + \left(\frac{\partial As}{\partial y}\right)^2 + \left(\frac{\partial As}{\partial z}\right)^2} \tag{3.12}$$

Taking the appropriate derivatives of the field and substituting for As as per equation 3.11 yields:

$$As_2 = \sqrt{\left(\frac{\frac{\partial f}{\partial x}\frac{\partial^2 f}{\partial x^2} + \frac{\partial f}{\partial y}\frac{\partial^2 f}{\partial x \partial y} + \frac{\partial f}{\partial z}\frac{\partial^2 f}{\partial x \partial z}}{\sqrt{\left(\frac{\partial f}{\partial x}\right)^2 + \left(\frac{\partial f}{\partial y}\right)^2 + \left(\frac{\partial f}{\partial z}\right)^2}}\right)^2 + \left(\frac{\frac{\partial f}{\partial x}\frac{\partial^2 f}{\partial x \partial y} + \frac{\partial f}{\partial y}\frac{\partial^2 f}{\partial y^2} + \frac{\partial f}{\partial z}\frac{\partial^2 f}{\partial y \partial z}}{\sqrt{\left(\frac{\partial f}{\partial x}\right)^2 + \left(\frac{\partial f}{\partial y}\right)^2 + \left(\frac{\partial f}{\partial z}\right)^2}}\right)^2 \ldots}$$

$$\sqrt{\ldots + \left(\frac{\frac{\partial f}{\partial x}\frac{\partial^2 f}{\partial x \partial z} + \frac{\partial f}{\partial y}\frac{\partial^2 f}{\partial y \partial z} + \frac{\partial f}{\partial z}\frac{\partial^2 f}{\partial z^2}}{\sqrt{\left(\frac{\partial f}{\partial x}\right)^2 + \left(\frac{\partial f}{\partial y}\right)^2 + \left(\frac{\partial f}{\partial z}\right)^2}}\right)^2} \tag{3.13}$$

Where f is the measured field and $\frac{\partial^2 f}{\partial z^2}$ can be calculated from Laplace's equation (Florio et al. 2006, Cooper, 2014):

$$\frac{\partial^2 f}{\partial x^2} + \frac{\partial^2 f}{\partial y^2} + \frac{\partial^2 f}{\partial z^2} = 0$$

Florio et al. (2006) state that since the analytical method (Equation 3.13) requires the computation of second order derivatives, whilst the finite difference method only requires first order derivatives, the latter approach is less susceptible to noise and hence should be used with real world data. It will be shown that the amount of noise produced by making use of the finite difference method depends on how the analytic signal amplitude at the elevated datum is calculated. That is if the analytic signal is upward continued or each of its components are upward continued and then recombined at the higher elevation. This is since the difference between the upward continued analytic signal amplitude and the base analytic signal amplitude is expected to be small, due to the finite upward continuation height used. Hence any inaccuracy in the application of the upward continuation operator is more detrimental to the resultant than it would be if the upward continuation height used was larger.

In the following discussion it is suggested that upward continuing each component of the analytic signal (dx and dz) prior to calculating the analytic signal amplitude at the elevated datum produces improved results compared to upward continuing the analytic signal amplitude alone.

In order to illustrate this, two forward models were produced. The first was of a thin magnetic dyke located at 500 m along a 1000 m profile at a depth of 10 m with a station spacing of 1 m. The second forward model was of a thin dyke located at 500 m along a 1000 m profile at a depth of 10.001 m. The vertical and horizontal derivatives of the two fields due to the two models were calculated and used to calculate the analytic signal amplitude of each field. The derivatives and the analytic signal amplitude of the shallower model were then upward continued by a height of 0.001 m and compared to their equivalent values calculated over the deeper model. Figure 3.1 shows the difference between the upward continued data components and the calculated responses over the deeper dyke. The difference between both the upward continued and the modelled derivatives (Figures 3.1a and 3.1b) are three orders of magnitude less than the difference between the upward continued analytic signal amplitude and the modelled analytic signal amplitude (Figure 3.1c).

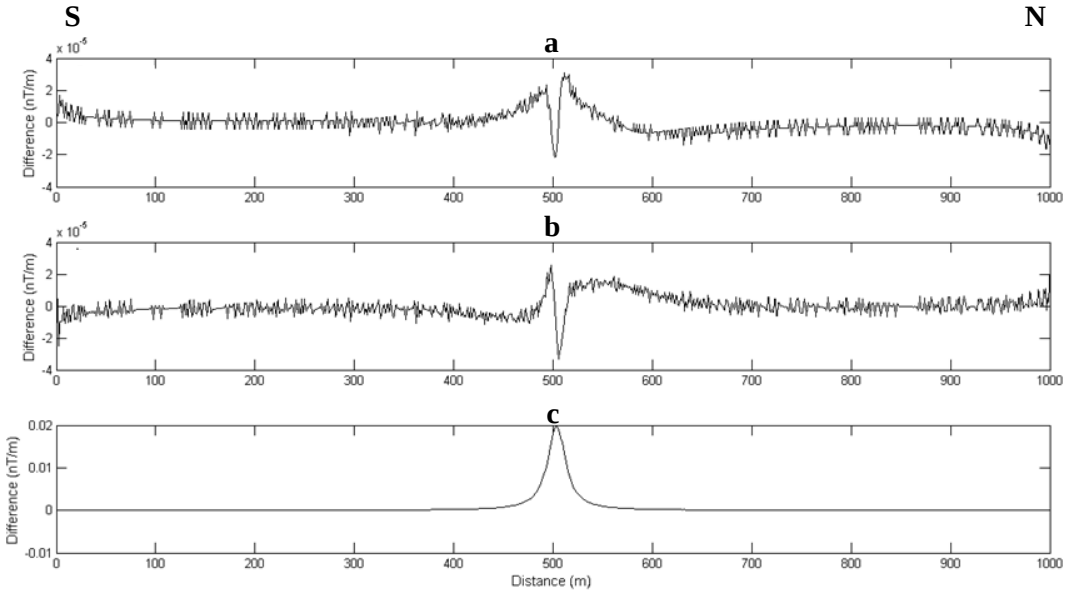


Figure 3.1 Difference between theoretical and calculated upward continued components of the Analytic Signal Amplitude. a) Difference between upward continued horizontal gradient (dx) and theoretical value of dx at the upward continued height. b) Difference between upward continued vertical gradient (dz) and theoretical value of dz at upward continued height. c) Difference between upward continued analytic signal amplitude (As) and theoretical value of As at upward continued height.

Figure 3.2 shows the difference between the analytic signal amplitude of the shallower model and the analytic signal amplitude at the elevated datum (after an upward continuation of 0.001 m). Two important features should be noted, firstly the maximum difference between the analytic signals calculated at the two different elevations is of equal magnitude to the noise envelope calculated in Figure 3.1c, and secondly the difference at some positions is negative. The second point implies that for those regions the upward continued analytic signal amplitude is greater than the original analytic signal. This cannot be the case since the analytic signal should fall-off with distance from the source. The noise imaged in Figure 3.1c shows a distinct peak near the source this implies that the process of upward continuation overestimates the analytic signal amplitude near the source. Hence the negative portions are formed when the upward continued analytic signal amplitude is subtracted from the base level analytic signal amplitude. The high frequency noise imaged is due to rounding errors in the computation at the station locations.

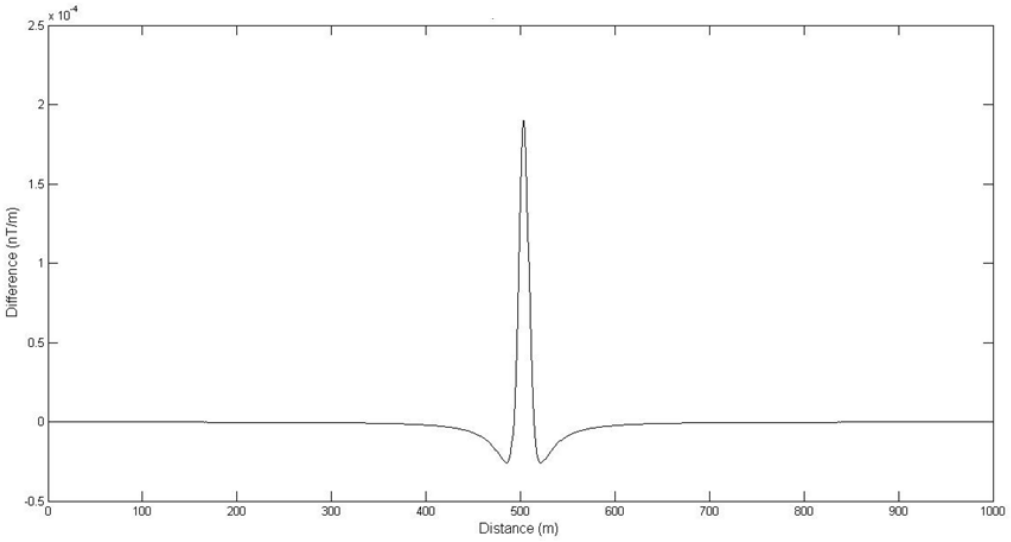


Figure 3.2 Difference between the analytic signal amplitude at the lower datum and at the higher datum. Note the negative values either side of the peak.

A comparison was then made between the results after applying the three methods for determining the vertical derivative of the analytical signal amplitude (Figure 3.3).

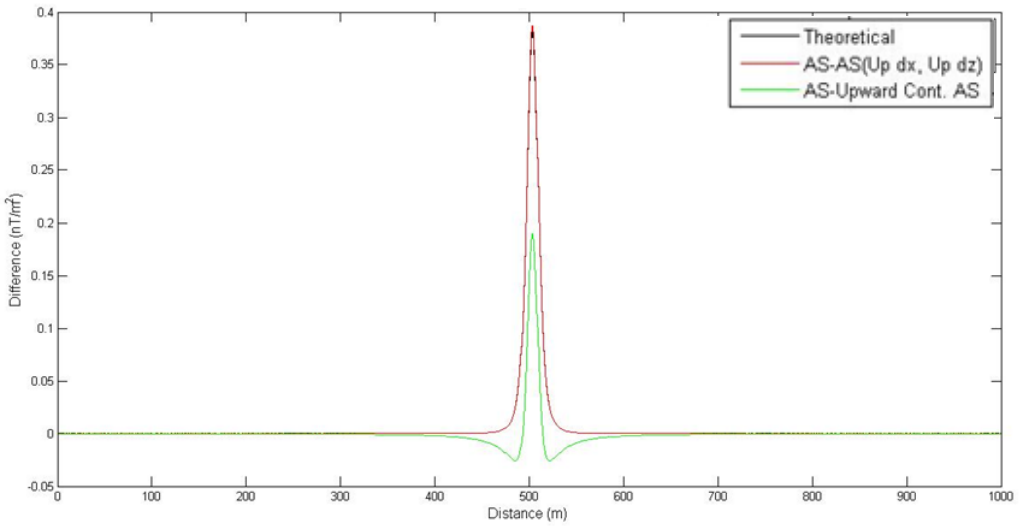


Figure 3.3 Vertical derivative of the analytic signal amplitude derived by upward continuing each component of the analytic signal amplitude compared to upward continuing the analytic signal amplitude. The results are compared to the analytic derivation (black line).

There was found to be good agreement between the results obtained by using the theoretical expression of the vertical derivative of the analytical signal (as used by Cooper, 2014) and upward continuing each component of the analytic signal with poor agreement between the theoretical and calculated values when calculating the vertical derivative of the analytic signal by upward continuing the analytic signal alone.

3.4 Calculation of the vertical derivative of the analytic signal amplitude applied to noisy data

Florio et al. (2006) suggest that the finite difference method should be employed when calculating the vertical derivative of the analytic signal amplitude since the finite difference method does not require the use of second order derivatives as found in the theoretical expression. Furthermore the description of the finite difference method involves upward continuing the analytic signal amplitude (Florio et al., 2006). Figure 3.4 shows the result of calculating the vertical derivative of the analytic signal amplitude over a dyke located at a depth of 10 m where the signal has been corrupted by 1% random Gaussian noise, via three different approaches.

Firstly, the theoretical expression for the vertical derivative of the analytic signal amplitude was calculated i.e. the third term in equation 3.13 (given in black on Figure 3.4). Secondly it was calculated by upward continuing each of the components of the analytic signal amplitude (dx, dz) before applying the finite difference method (given in red on Figure 3.4), finally by upward continuing the analytic signal amplitude and working out the finite difference (given in green on Figure 3.4). The results indicate that when the vertical derivative of the analytic signal amplitude is required to be calculated for noisy data the theoretical expression should be used. In instances where the finite difference method is to be employed then upward continuing each component of the analytic signal amplitude before recombining at the elevated datum should be done instead of upward continuing the analytic signal amplitude alone.

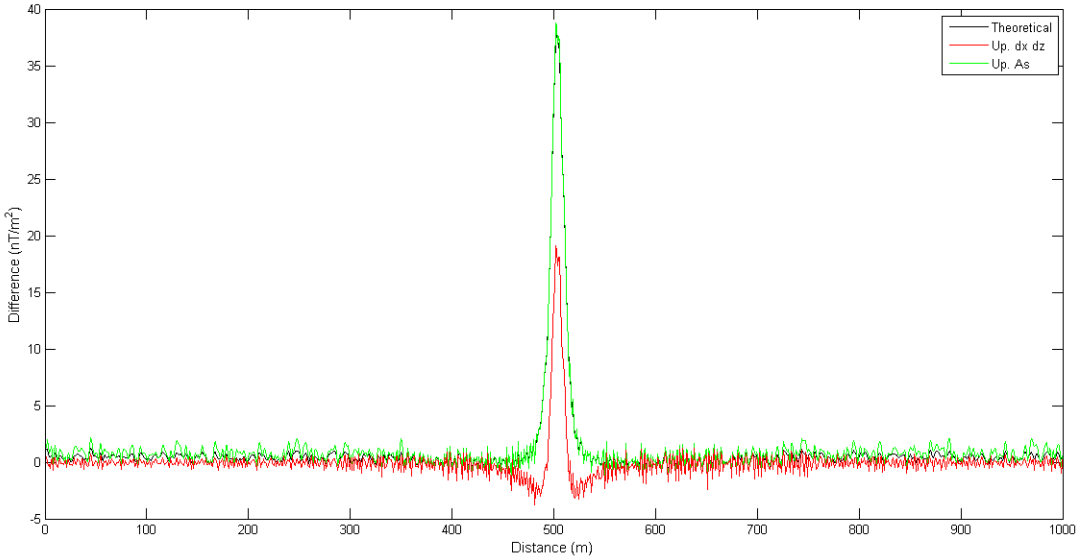


Figure 3.4 Calculation of the vertical derivative of the analytic signal amplitude over a thin dyke via three different methods. First via the theoretical expression for the derivative (given in black), secondly by upward continuing each of the components of the analytic signal amplitude (given in red), lastly by upward continuing the analytic signal amplitude (given in green) before applying the finite difference method.

3.5 Application of the analytic signal amplitude for depth/distance determination

The source-distance method proposed by Cooper (2014) was applied to theoretical profile data (Figure 3.5). The forward modelled body was step-like with a minimum depth of 25 m and a maximum depth of 75 m with each step having a width of 200 m and a susceptibility of 0.01. The flanks to each step dipped at an angle of 45°. The local magnetic inclination was set to -60° with a declination of 0°. The profile was orientated south-north. The resulting source-distance estimates were compared to solutions found by Euler deconvoulution (making use of a window length of 10 samples) and are much easier to identify since no cluster analysis needs to be done, since the method only requires that the local minima need to be identified. A structural index of 0 was used (appropriate for contacts). This model indicates that the method can be applied to non-RTP data as well as dipping bodies, and hence overcomes many of the limitations of the tilt-depth method. Furthermore since the presence of remnant magnetisation affects the measured signal in the same was as a change in dip the distance to source method proposed by Cooper (2014) can be used on remantly magnetised bodies. It should be noted however that the source-distance method only identifies the top corners of the body

and cannot determine the dip or susceptibility, hence a total replication of the measured field cannot be made from the source distance alone.

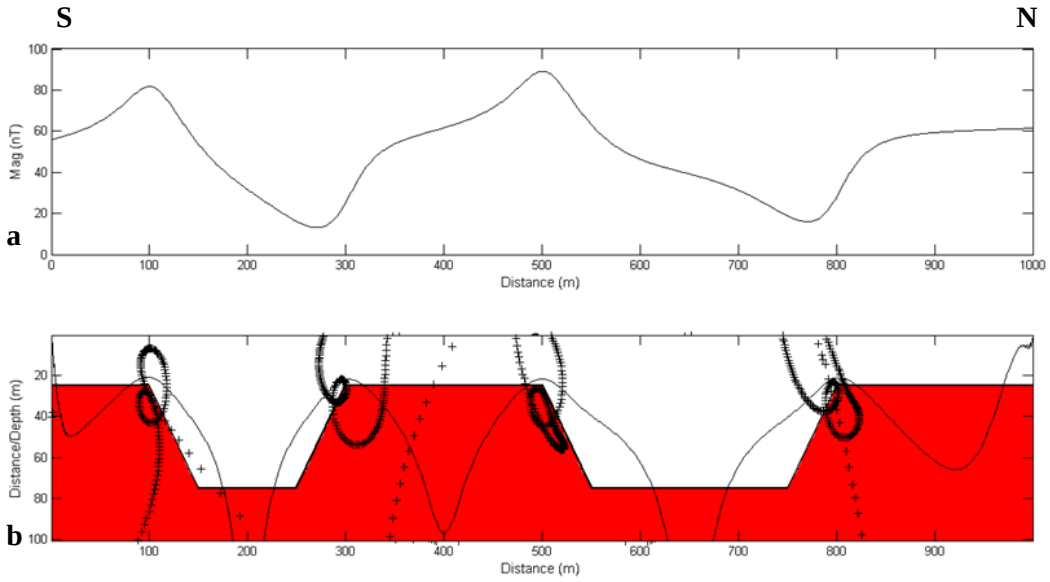


Figure 3.5 Application of the analytic signal amplitude depth determination method to profile data following Cooper (2014). a) Calculated magnetic field for model shown in red. b) Forward model (in red) and calculated distance/depth solutions. Cooper (2014) - solid lines, Euler solutions – crosses

The distance to source method proposed by Cooper (2014) was then applied to the magnetic field calculated over a magnetic prism located at a depth of 5 m with a magnetic inclination of -60° and declination of 30° (Figure 3.6a) using a structural index of 0. The prism was 100 m by 100 m with vertical sides.

The resultant distance to source method (Figure 3.6b) is equal to the true depth of the prism directly over the edges of the body. However, near the corners of the prism the depth is underestimated; this is due to the structural index used being too low. (The structural index should increase towards the corners of the body since a corner has a faster fall off rate than an edge). The correct shape of the source, reasonable depth estimation and ease of use, makes this method attractive.

The depth from known locations on the analytic signal method proposed by Ma and Du was applied to data calculated over a synthetic dyke located at a depth of 17 m midway along a 600 m long profile. This was the same model that Ma and Du (2012) discussed

(Figure 3.7). The calculated depth of the source and structural index after applying equations 3.8 and 3.9 respectively are given in Figure 3.8. The values were calculated by knowing the true horizontal location of the source. This together with the limitation that the method can only be used with profile data makes the applicability of the method limited.

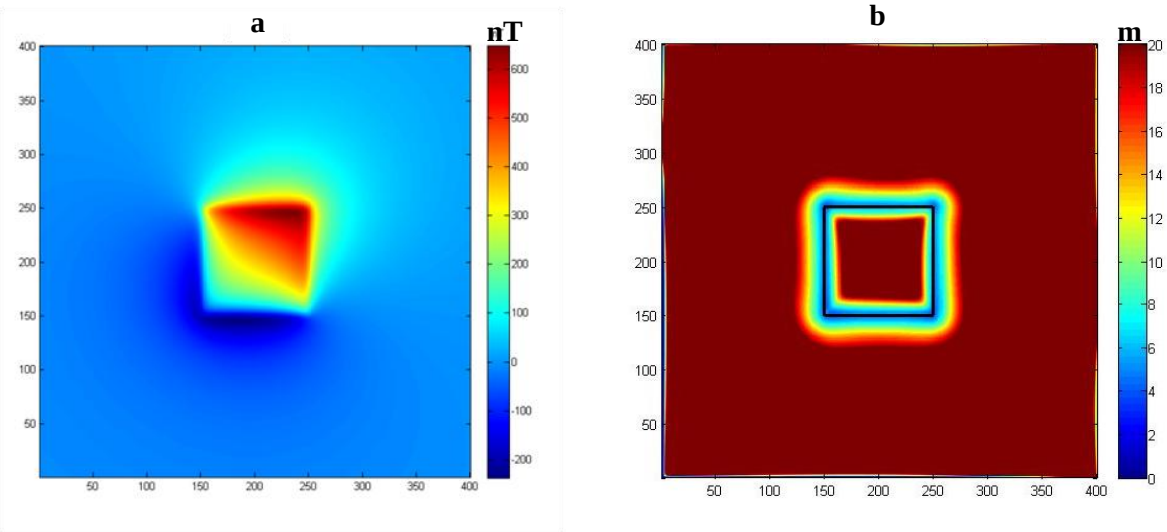


Figure 3.6 Application of the method proposed by Cooper (2014) to gridded data. a) Calculated magnetic field over a 100 m by 100 m magnetic prism with infinite depth extent at a depth of 5 m with a magnetic field inclination of -60° and a declination of 30°. b) Calculated distances to source, overlaid with magnetic prism boundary (black line).

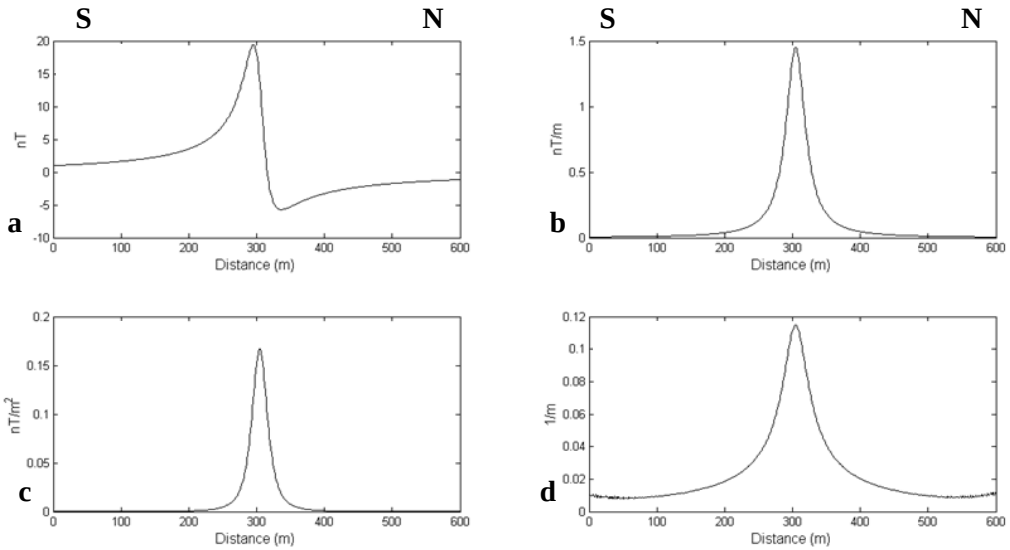


Figure 3.7 Application of the method proposed by Ma and Du (2012). a) Magnetic field over a vertical dyke located at (300 m, 17 m) with a magnetic field inclination of 60° and a declination of 0°. b) First order analytical signal amplitude. c) second order analytical signal amplitude. d) Ratio of the first and second order analytical signal amplitudes. (Adapted from Ma and Du (2012)).

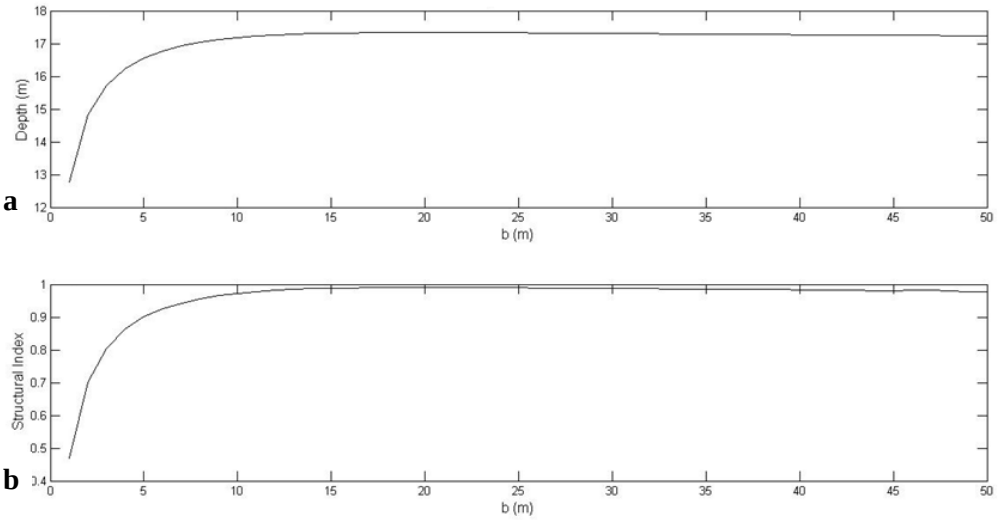


Figure 3.8 Resultant depth and structural index after the application of the method proposed by Ma and Du (2012) plotted against distance from the known horizontal position of the source. a) Estimated depth of the source (true depth 17 m). b) Estimated structural index of the source (true value 1).

3.6 Discussion on the Presented Analytic Signal Amplitude Depth Determination Methods

Taking the ratio of the first and second order analytic signal amplitudes, as is done in the source-distance method proposed by Cooper (2014), eliminates terms describing the strength of the inducing magnetic field and susceptibility of the body thus simplifying the inversion problem. Furthermore, making use of the analytic signal amplitude allows for the described methods to be applied to dipping and or remnant magnetised bodies unlike the Tilt-Depth method (Salem et al., 2007, Cooper, 2014) since the definition of the analytic signal amplitudes is devoid of such terms. Any inversion method that can be easily applied to not only profile data but also gridded data is immediately more attractive. Both the source-distance method and the depth from known points on the analytic signal method are based on making use of the analytic signal amplitude to invert for the position of the source are dependent on the structural index. If the structural index can be determined then the method described by Cooper (2014) can be adapted to accurately determine the distance to source from data containing multiple differently shaped bodies. For example is data were collected over both a dyke and a contact one would expect that the inverted distance to source estimates would be half or double the

true value for one of the bodies if a single structural index was assumed for the entire dataset. However if the structural index is know, then this can be corrected for by multiplying the distance to source estimates of that particular body by an appropriate amount. Compared to the inversion methods previously described, this adapted distance to source approach would be more readily applicable to most magnetic depth inversion problems. In comparison, the higher orders of differentiation required to calculate the second order analytic signal amplitude will always tend to lead to increased noise levels compared to the first order derivative based methods.

	Profile Data	**Grid Data**	**Known S.I.**	**Higher order derivatives**	**Further evaluation of results**
Distance to source method	**Yes**	**Yes**	**Yes**	**Yes**	**No – Local minima clearly visible and equivalent to depth of body**
Depth from known points	**Yes**	**No**	**No**	**No**	**Yes – To calculate depth and structural index the horizontal distance from the source needs to be known**

Table 3.1 Comparison between the distance to source method (Cooper, 2014) and the depth from known points method (Ma and Du, 2012).

Chapter 4: Estimating the Structural Index - Depth from Extreme Points

Proposed by Fedi (2007), Depth from Extreme Points (DEXP) is a semi-automatic interpretation method that can be applied to both magnetic and gravity data to solve for the depth, structural index and excess mass / dipole moment intensity of the source. The procedure entails upward continuing the data to construct a three dimensional data volume above the acquisition datum. At each upward continued height the calculated magnetic field values are scaled according to a defined scaling function which is dependent on the upward continuation height and the structural index of the source (Fedi, 2007). This scaling function is derived from assuming that the field falls off with distance to a certain power, hence taking the log of that fall-off results in a linear transform. The locations of local maxima within this constructed scaled volume are symmetrical about the x, y plane with the true location of the source in the subsurface (Figure 4.1). When the structural index is not known, multiple iterations of the procedure are applied under the assumption of different structural index values. For different input datasets the resultant location solutions will be similar under the correct assumed structural index but dissimilar under the incorrect choice.

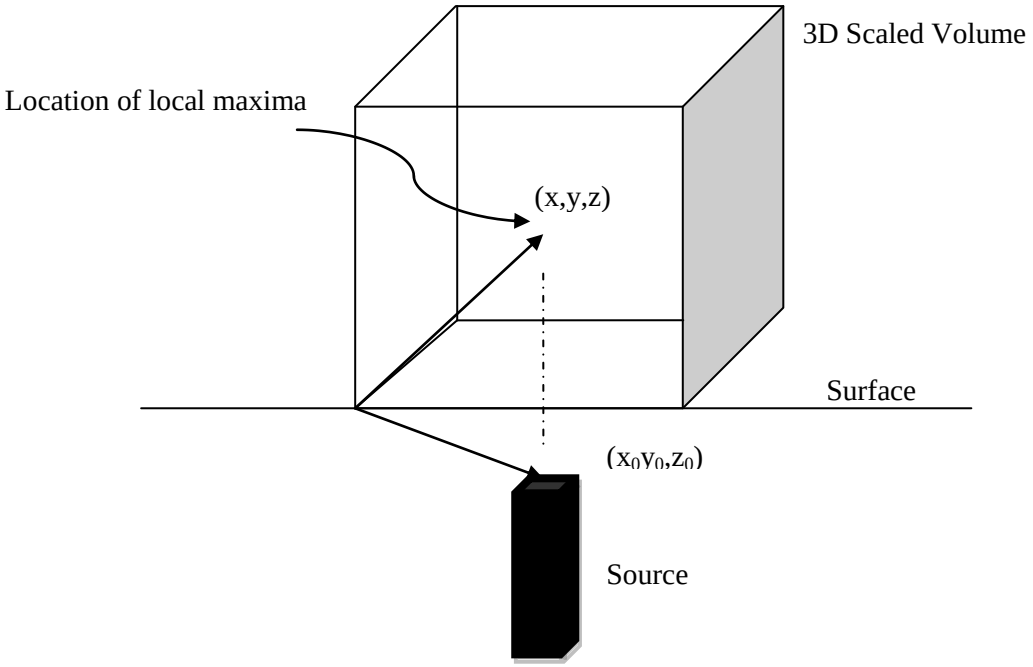


Figure 4.1 Simplified representation of the depth from extreme points method. The local maxima withn the 3D volume is located at (x,y,z) while the source (indicated in black) is located at (x_0,y_0,z_0). (x,y,z) and (x_0,y_0,z_0) are symmetric about the x-y plane as indicated by the dotted line.

4.1 Theoretical background of the DEXP method

A normalised magnetic field due to a point source observed from directly above ($x_0 = 0, y_0 = 0$) at a height of z has the form of:

$$f_1(z) = \frac{1}{(z - z_0)^2} \tag{4.1}$$

where f is the measured field, z and z_0 are the point of observation and the depth of the source respectively. Fedi (2007) defines the scaling function used to scale the volume above the body by:

$$\tau_1(z) = \frac{\partial\, log[f(z)]}{\partial\, log(z)} \tag{4.2}$$

For a source such as f_1 (equation 4.1), equation 4.2 simplifies to (Fedi, 2007):

$$\tau_1(z) = -\frac{2z}{z - z_0} \tag{4.3}$$

Hence directly above the source at an observation height equal to the depth to the source ($z = -z_0$) equation 4.3 reduces to:

$$\tau_1(z = -z_0) = \frac{\partial\, log[f_1(z)]}{\partial\, log(z)}\bigg|_{z=-z_0} = -1 \tag{4.4}$$

Differentiating equation 4.4 with respect to z and simplifying (Fedi, 2007) yields:

$$\frac{\partial log[f_1(z)]}{\partial z}\bigg|_{z=-z_0} = -\frac{\partial log(z)}{\partial z}\bigg|_{z=-z_0}$$

$$\frac{\partial\{log[f_1(z)] + log(z)\}}{\partial z}\bigg|_{z=-z_0} = 0 \tag{4.5}$$

Hence the function $log[f_1(z)] + log(z)$, for a fixed value of z_0 in f_1 will reach a maximum (have a zero gradient by the above equation) when $z = -z_0$. Plots of the function $log[f_1(z)] + log(z)$for three values of z_0 against upward continuation height z are presented in Figure 4.2. Each resultant curve reaches a maximum when $z = -z_0$.

It is shown by Fedi (2007) that the scaling function for different sources is given by:

$$W_n = z^{a_n} f_n \tag{4.6}$$

The scaling exponent a_n in equation 4.6 is similar to the conventional Euler based structural index since both quantities describe the fall-off rate of the field with distance from the source (Fedi, 2007). In fact the scaling exponent is half of the structural index value of the source (Fedi, 2007), with each order of differentiation of the input used increasing the scaling exponent used for a particular source by 1. I.e. if the vertical derivative of the field over a contact (structural index of 0) is to be scaled then the scaling exponent used should be 1 ($a_n = \frac{0}{2} + 1$).

The resultant scaled field volume constructed over the body to user defined height is then analysed for the location of local maxima and minima. Such points will be located at $x_0 = x, y_0 = y, -z_0 = z$, where$(x, y, z)$ (is the point of observation and $(x_0, y_{0,} z_0)$ is the location of the source, with both points being symmetrical about the x-y plane (Fedi, 2007).

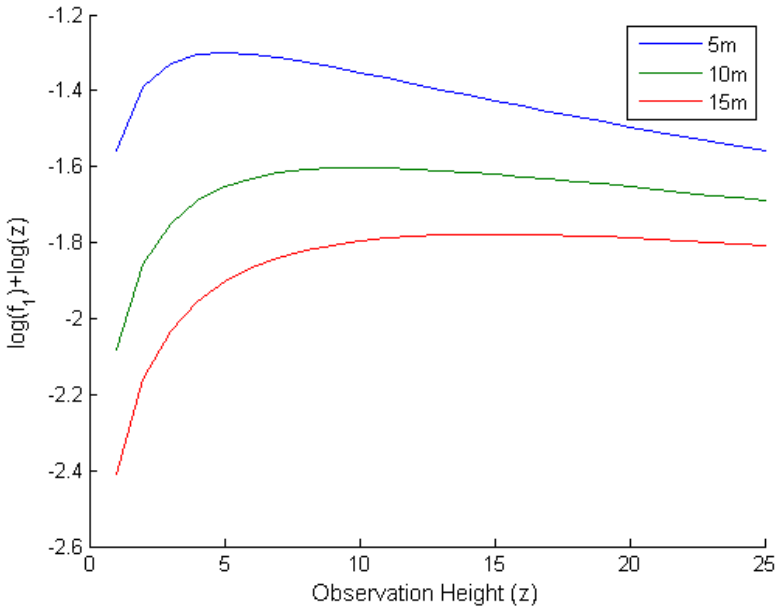


Figure 4.2 log(f_1)+log(z) as a function of observation height (z) for fixed values of z_0 (5m, 10m, 15 m) calculated directly over the source (x = x_0 , y = y_0). The function reaches a maximum value where z = -z_0. f_1 is calculated from equation 4.1

The correct choice of structural index for a particular source can be found by observing the location of the extreme points within the volume when the method is applied to the total field compared to when it is applied to the n^{th} vertical derivative of the field. Under the correct structural index choice, the location of the extreme points within the volume will not change for the two datasets (Fedi, 2007). However if the incorrect choice of structural index is made then the location of the extreme points will not coincide. In this way the structural index of the source can be determined.

4.2 Application of the DEXP method

4.2.1 Application of the DEXP method to profile data

The magnetic field over a thin vertical dyke located midway along a 1000 m long profile at a depth of 30 m with a local inducing magnetic field with an inclination of -90° and a declination of 0° was calculated. This field was then upward continued in 1 m intervals to a height of 50 m. The scaling function, equation 4.6, was then applied to each upward continued data subset. A scaling exponent of 0.5, appropriate for a dyke with structural index of 1 was used. The position of the local maxima within the resultant plane was then found to occur at x = 503 m z = 30 m, which is in good agreement with the true location of the source. The results are presented in Figure 4.3.

The same model was then calculated under non-RTP conditions, with a magnetic field inclination of -60° to assess how the method behaves with respect to non-RTP data. The first vertical derivative and the analytic signal amplitude of the data were then also used as input into the method together with the appropriate scaling function in an attempt to recover the correct structural index as proposed by Fedi (2007).

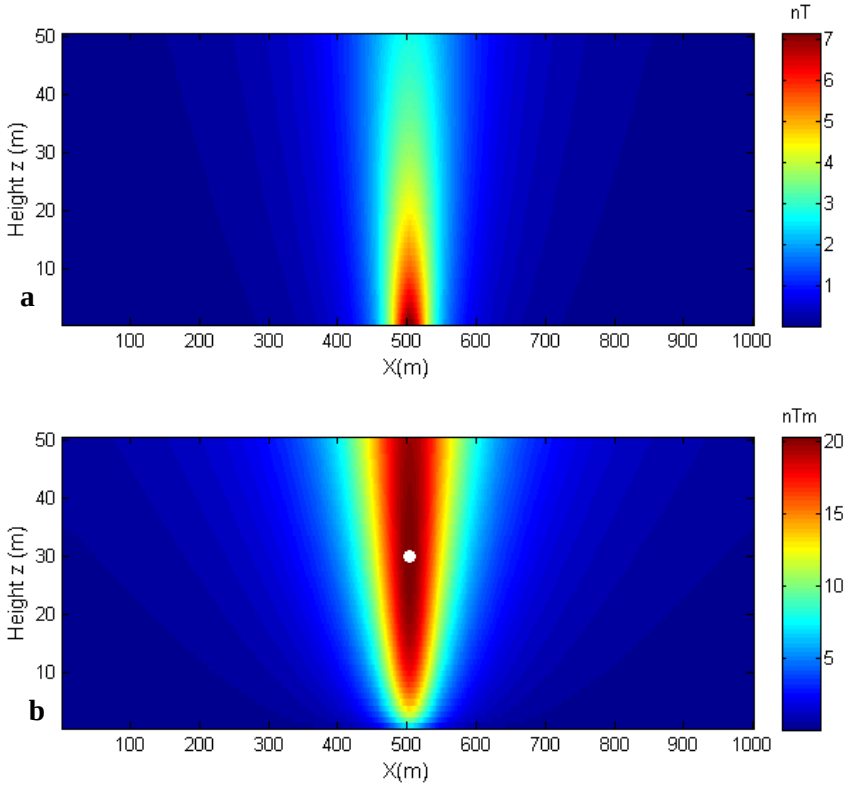


Figure 4.3 Application of the DEXP method over a dyke located at x_0 = 500 m z_0 = 30 m with a local field inclination of -90°. The top subplot shows the total magnetic field as a function of upward continuation height for the profile. The bottom function shows the scaled output after using a scaling exponent of 0.5 (appropriate for a dyke). The white dot indicates the position of the maximum of the scaled output and is located at (x = 503 m, z = 30 m).

The data was firstly assumed to be due to a N=1 source (a dyke, hence scaling exponents of 0.5, 1 and1 were used for input consistent with the total field, the vertical derivative and analytic signal amplitude respectively), secondly it was assumed to be due to a N=0 source (a contact, with scaling exponents of 0, 0.5, 0.5 for the three types of input). This resulted in six estimated locations of the source (Figure 4.4). The three solutions associated with a structural index of 1 show a closer grouping than the three solutions with an assumed structural index of 0. This shows how the method can be applied to estimate the structural index of the source in an iterative manner.

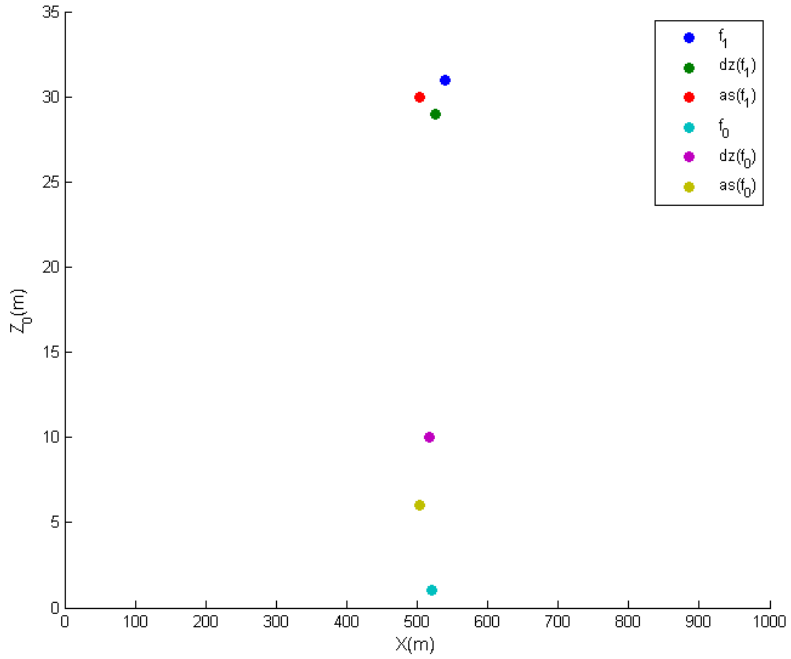


Figure 4.4 Application of the DEXP method to non-RTP data. Scatter points represent the position of the maximum in the scaled outpoint after applying the appropriate scaling exponent. As input the total field, the vertical derivative and the analytic signal amplitude were used. The structural index was first assumed to be equal to 1 and then equal to 0.The closest grouping (red green and blue dots) occurred when a structural index of 1 was assumed (appropriate for a dyke).

The slight amount of scatter within the tightest grouping of solutions is due to using non-RTP data with the analytic signal amplitude giving the best estimate of the true location of the source. Hence application of this method should be limited to RTP data or direct application to the analytic signal amplitude or n^{th} vertical derivatives of the field if the structural index is to be determined.

4.2.2 Application of the DEXP method to gridded data – Extended DEXP

The DEXP method was then expanded to accommodate gridded data. The procedure employed was to scale the upward continued first and second order vertical derivatives of the gridded data under the assumption of N = 0, 1 and 2 sources. The height at which the maximum occurred within the volume for each position on the grid was then found. Thereby six depth estimates for each position were recorded, two from each type of input (the first and second order derivatives) for each of the three assumed sources. The

absolute difference between the two depth estimates produced for each of the assumed sources is then calculated. This results in three absolute difference values for each x-y position on the gridded dataset. For each position on the grid the minimum difference value appropriate for that position is then used to assign a structural index of N= 0,1 or 2 to that position. The depth of that position is then given by the depth estimate previously calculated for that particular source (from the first vertical derivative depth estimate).

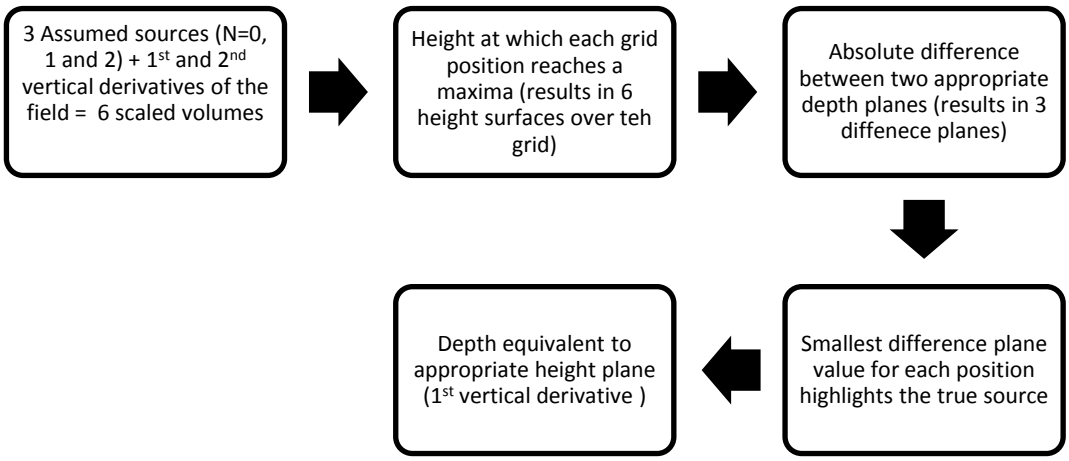


Figure 4.5 Summary of the workflow procedure implemented when applying the extended DEXP method to gridded data.

This adapted method was applied to three synthetic models over a magnetic contact, dyke and point source. The local magnetic field was set to -90° (pole reduced field). The contact was located at a depth of 10 m whilst the dyke and the point source were located at 20 m below the surface. The results of the adapted method are presented in Figure 4.6.

The structural index and the depth estimates calculated for the point source and the dyke correlate well with the expected values. For the contact, the structural index and the depth estimates vary more significantly near the true location of the contact, however directly over the source the structural index and depth estimates both approach their true values. Variation in the estimated structural index coincides with what would be expected from first principles. For example the variation of the estimated structural index over the point source falls off with distance from the source. The abrupt changes in the depth to the source are due to the change in the calculated structural index values.

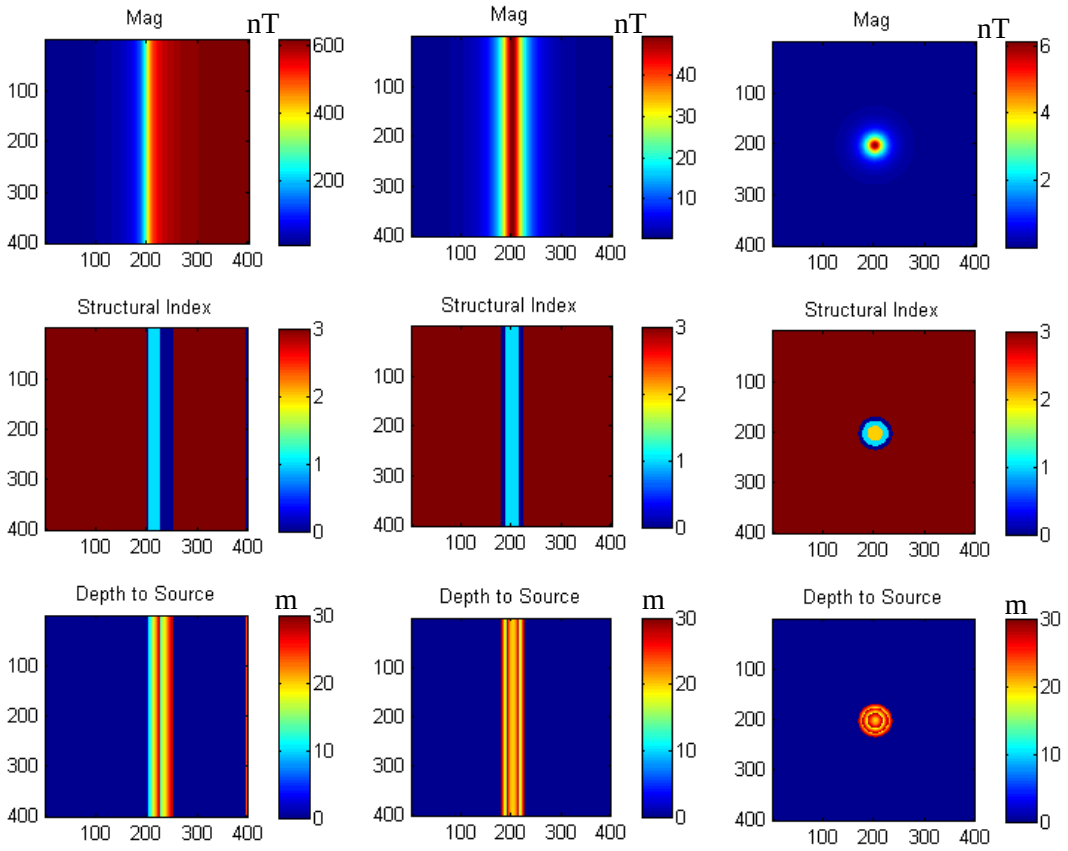


Figure 4.6 Application of the extended DEXP method to solve for the structural index and depth to source over three synthetic sources. Column 1: Magnetic field, structural index and depth to source calculated over a contact. Column 2: Equivalent values calculated over a dyke. Column 3: Equivalent values calculated over a point source. The contact was located at a depth of 10 m whilst the dyke and point source are located at a depth of 20 m. RTP-source was used.

As proven above the DEXP method can determine the depth and structural index of the source in a fully automated fashion. However, this requires multiple input datasets and multiple iterations of the scaling function. Moreover, the maximum imaged depth can only be as great as the maximum upward continuation height used to construct the data volume above the source. Finally the accuracy of the results depends on the upward continuation height interval. For example in the data volume were constructed at 10 m height intervals then the final depth solutions can only be reported to within 10 m. So whilst the method provides depth and structural index information, the amount of computation for accurate results over a large dataset is extensive.

Chapter 5: New Method: Multi-directional distance and structural index determination from analytic signal amplitude variation recorded at two different elevations

The use of upward continuation in any inversion method is attractive in that it inherently reduces noise levels as well as provides a second dataset on which analysis can be done. Any difference between this second dataset and the first can be attributed to a relative change in the depth of the source equal to the upward continuation distance used, which is always known.

Furthermore, solving for each of the three directional distances to source instead of the total distance to source is advantageous when applying techniques that make use of upward continuation since such techniques change the vertical distance to the source but leave the horizontal distances unchanged. The three positional elements can later be recombined to solve for the distance to the source since $\mathrm{R} = \sqrt{(\mathrm{x} - \mathrm{x}_0)^2 + (\mathrm{y} - \mathrm{y}_0)^2 + (\mathrm{z} - \mathrm{z}_0)^2}$. One such way of implementing such an approach is now described using the ratio of the appropriate directional derivative of the analytic signal to the total analytic signal. This method was developed by the author and termed multi-directional distance inversion which not only gives the multi-directional distances to the source but also the structural index of the source as will be shown. This is advantageous since the structural index can be used as input into Euler deconvolution and / or the source-distance method (Cooper, 2014).

5.1 Multi-Directional distance inversion - Theoretical background

Given the expression for the analytic signal amplitude As (Salem et al., 2004):

$$As = \frac{k}{((x - x_0)^2 + (z - z_0)^2)^{\frac{N+1}{2}}} \tag{5.1}$$

where k is a constant related to the magnetisation of the source, N is the structural index x and z are the horizontal and vertical positions of the source respectively and x_0 and z_0 locate the point of observation above the source. Dividing the vertical derivative of equation 5.1 by equation 5.1 gives (see appendix B):

$$\frac{\frac{\partial As}{\partial z}}{As} = -\frac{(z - z_0)(N + 1)}{(x - x_0)^2 + (z - z_0)^2} \tag{5.2}$$

Solving equation 5.2 for $(x-x_0)^2+(z-z_0)^2$ and substituting into the expression for the distance to source given by Cooper (2014) (Chapter 3, equation 3.10), yields:

$$\frac{(z-z_0)}{(N+1)} = -\frac{As\frac{\partial As}{\partial z}}{{As_2}^2} \tag{5.3}$$

Where As_2 is the second order analytic signal amplitude. Likewise, if a similar operation is applied to the horizontal distances instead of the vertical distance as in equation 5.3 the following will also hold:

$$\frac{(x-x_0)}{(N+1)} = -\frac{As\frac{\partial As}{\partial x}}{{As_2}^2} \tag{5.4}$$

$$\frac{(y-y_0)}{(N+1)} = -\frac{As\frac{\partial As}{\partial y}}{{As_2}^2} \tag{5.5}$$

z and N are then solved for by obtaining another dataset through upward continuation i.e:

$$\frac{(z-z_0)+dz}{(N+1)} = -\frac{As_{up}\frac{\partial As_{up}}{\partial z}}{{As_{2up}}^2} \tag{5.6}$$

and solving via substitution where dz is the upward continuation distance, As_{up}, As_{2up} and $\frac{\partial As_{up}}{\partial z}$ are the first and second order analytic signal amplitudes and the vertical derivative of the analytic signal at the higher elevation respectively.

The recombined expression for the distance to source (by combining equations 5.4, 5.5 and 5.6) is the same as that proposed by Cooper (2014)) (Chapter 3, equation 3.10), however through this method upward continuation can be used to obtain a second dataset to solve for the structural index (N), without making any assumptions about the nature of the source and or the location of the point of observation. Furthermore if the measured data are noisy then upward continuation can be applied prior to the application of the proposed method, with the upward continuation height being subtracted from the calculated vertical distance alone and not from the resultant distance to source, this leads to a better estimation of the true distance to the source.

5.2 Application of the multi-directional distance to source method

This approach was applied to theoretical data for both a vertical dyke and contact model located at a depth of 20 m with a magnetic field inclination of -90° and a declination of 0°, the results are shown in Figure 5.1. The structural index was determined by solving equations 5.3 and 5.6 simultaneously over an upward continuation height of 10 m. The structural index over both models was well estimated and hence could be used to rescale the distance to source (Cooper, 2014) to provide accurate estimates of the depth of each of the bodies.

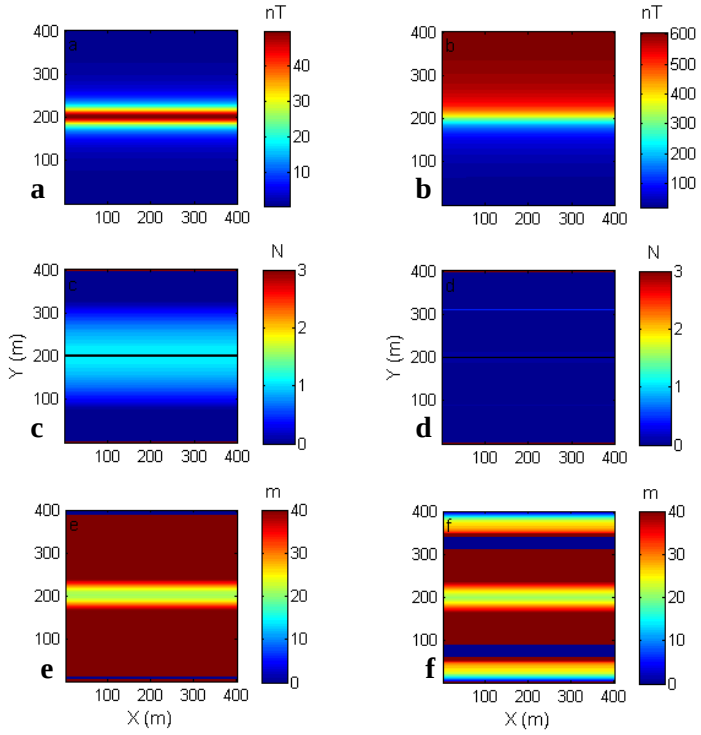


Figure 5.1 Multi-directional distance to source and structural index estimation over a thin (5 m) vertical dyke and contact located at a depth of 20 m. a, b) Calculated magnetic field over the dyke and contact. c, d) Estimated structural index values with the contour line of $R_h = 0$ overlaid. e, f) Rescaled distance to source estimations.

An advantage of adopting this method is that it can act as an edge detection operator since the null values of the horizontal distances (equations 5.4 and 5.5) by definition will define the body edges. To illustrate this the horizontal structural index dependent distance to source ($R_h = \sqrt{\left(\frac{(x-x_0)}{(N+1)}\right)^2 + \left(\frac{(y-y_0)}{(N+1)}\right)^2}$) was calculated and the contour of $R_h = 0$ was plotted on the estimated structural index values (Figures 5.1 c and d in black). The results clearly delineate the edges of the two models.

Since the total distance to source becomes greater as a function of horizontal distance to source multiplying the estimates by a small structural index (as was the case for the contact model) decreases this effect. Due to this Figure 5.1 f has noise on the edges of the image hence R_h should be calculated to identify true solutions.

The need to upward continue the data and the need to calculate R_h makes this new method more computationally extensive than source-distance method (Cooper, 2014). In contrast however, where the structural index is not known this method should be employed over the source-distance method since it does not require the structural index a-priori. Furthermore, this method can be employed as a stable edge-detection filter which is clearly advantageous in image processing or to identify zones that warrant further investigation.

Chapter 6: New Method: Structural index estimation from the analytic signal amplitude fall-off rate

In this method the variation in the analytic signal amplitude with distance to source is used to solve for the structural index. This approach is applicable to both profile and gridded data and is not constrained to being applied to certain source types or inducing field orientations. The variation in the analytic signal amplitude with distance is produced by the use of two datum elevations on which these values are calculated. The first datum elevation is the datum at which the data were acquired, while the second is constructed through the process of upward continuation. If the data are assumed to be noisy then the first elevation can itself be calculated above the measurement datum to reduce noise levels, with the second being constructed above that. The separation between the two elevations should be small enough as to not change the observed structural index for the source. For typical values a separation between 1 and 100 m should be sufficient.

The analytic signal amplitude and distance to source at the higher datum are calculated from the upward continued field instead of upward continuing the analytic signal to preserve data integrity (refer to section 3.2). It will be shown that this method does not rely on the correct choice of structural index (N) when calculating the distance to the source via the analytic signal amplitude method of Cooper (2014) so long as the same structural index is used at the two different elevations. The resultant structural index values are then used to define what is termed a rescaled distance to source after rescaling the distance to source by (*N+1*).

6.1 Analytical signal amplitude fall-off - Theoretical background

Given the expression for the analytic signal amplitude of Salem et al. (2004):

$$As = \frac{k}{((x-x_0)^2+(z-z_0)^2)^{\frac{N+1}{2}}} = \frac{k}{R^{N+1}} \tag{6.1}$$

where, k is a constant related to the magnetisation of the source and x and z are the horizontal and vertical positions of the source respectively. Hence if the analytic signal amplitude and the distance to source at two different elevations are known then solving equation 6.1 for k observed from the two different elevations:

$$AsR^{N+1} = As_{up}\,R_{up}{}^{N+1} \tag{6.2}$$

where As, R and As_{up}, R_{up} are the analytic signal amplitude and distance to source at the lower and higher elevations respectively. Taking the logarithm of equation 6.2 gives:

$$log(As) + log(R^{N+1}) = log(As_{up}) + log(R_{up}{}^{N+1}) \tag{6.3}$$

Simplifying equation 6.3 and solving for the structural index yields:

$$log(As) - log(As_{up}) = (N+1)(log(R_{up}) - log(R))$$

$$N = \frac{log\left(\frac{As}{As_{up}}\right)}{log\left(\frac{R_{up}}{R}\right)} - 1 \tag{6.4}$$

When the distance to source is calculated (Cooper, 2014) the structural index acts as a proportionality constant, hence taking the ratio of the two distance to source estimations, as in the denominator of equation 6.4, eliminates the dependence on the correct choice of computational structural index. I.e.:

$$\frac{R_{up}}{R} = \frac{\frac{(N+1)As_{up}}{As_{2up}}}{\frac{(N+1)As}{As_2}} = \frac{As_{up}\,As_2}{As_{2up}\,As}$$

where As_{up} and As_{2up} are the first and second order expressions for the analytic signal amplitude calculated on the higher datum.

6.2 Application of the analytic signal amplitude fall-off method

To test this method two theoretical contacts and their respective calculated magnetic responses were considered. The first contact was located at a depth of 20 m midway along a 1000 m north-south striking profile with the second contact located at a depth of 30 m. The local magnetic inclination was -60° whilst the declination was set to 0° for both models. The analytic signal and the distance to source, via the distance to source method (Chapter 3, equation 3.10) (Cooper, 2014) (with a structural index of 0) was calculated for both models, the results of which are shown in Figure 6.1. The distance to source for both the 20 m deep contact (Figure 6.1f) and for the 30 m deep contact (Figure 6.1c) were well estimated. The structural index was then determined using the analytic signal amplitude fall-off method (equation 6.4) with the result shown in Figure 6.1g. The

magnitude of the calculated structural index is close to the theoretical value for a contact (0) and varies slowly with horizontal positions away from the source, showing good stability. (The vertical lines to the right of the local minimum plot values that are outside of the window range).

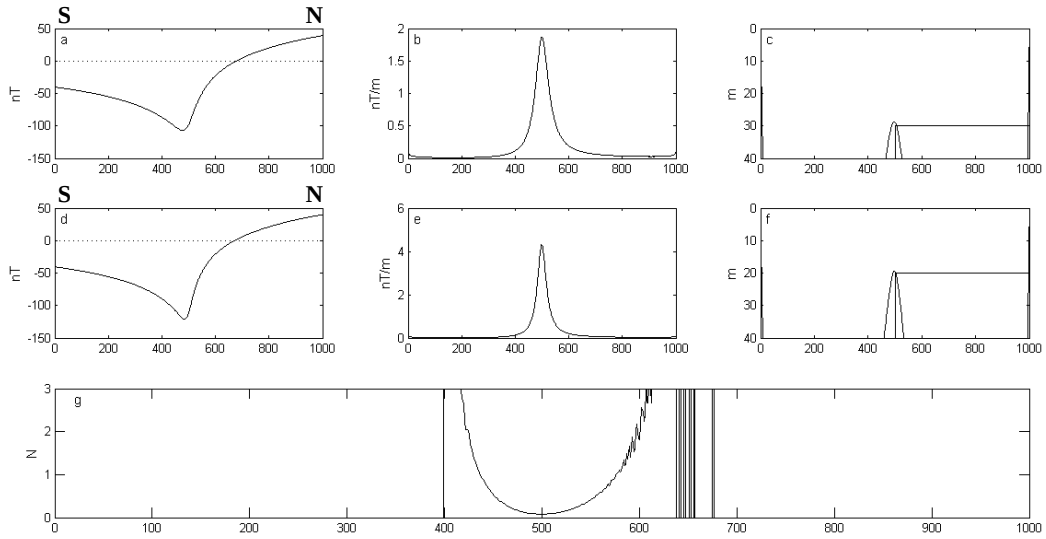


Figure 6.1 Conceptual application of the analytic signal fall-off rate method applied to contacts. a, b, c: The total magnetic field, the analytic signal amplitude and the distance to source of the contact located at a depth of 30 m respectively. d, e f: The total magnetic field, the analytic signal amplitude and the distance to source of the contact located at a depth of 20 m respectively. g Structural index estimation. The local magnetic field inclination was set at -60^0 and the declination was set to 0^0. For both distance to source estimates a structural index of 0 was used.

The two models were then adapted by replacing the contacts with thin vertical dykes, both located at the same depth. Again the analytic signal amplitude, distance to source and structural index were determined (Figure 6.2). Note that the calculated distance to source for both of the models is half of the true distance to source. This is due to using a structural index of 0 instead of a correct choice of 1 for a dyke. The distance to the source can however be corrected by making use of the estimated structural index to give a rescaled distance to source estimation.

The analytic signal fall-off method was then applied to the theoretical anomaly over both the previously modelled contact and the dyke located at a depth of 20 m calculated from the previous models, using an upward continuation height of 5 m to separate the two data elevations (5 m was chosen at random but it is recommended that un upward continuation height greater than the station spacing be used). The results are shown in Figure 6.3.

Whist there is somewhat of an increase in noise levels along the profile in its entirety (compared to Figures 6.1g and 6.2g); near the location of both sources the structural index is well estimated (there is a reduction in noise levels and the values are close to 1over the dyke) and is imaged by reduced noise levels and a near horizontal gradient.

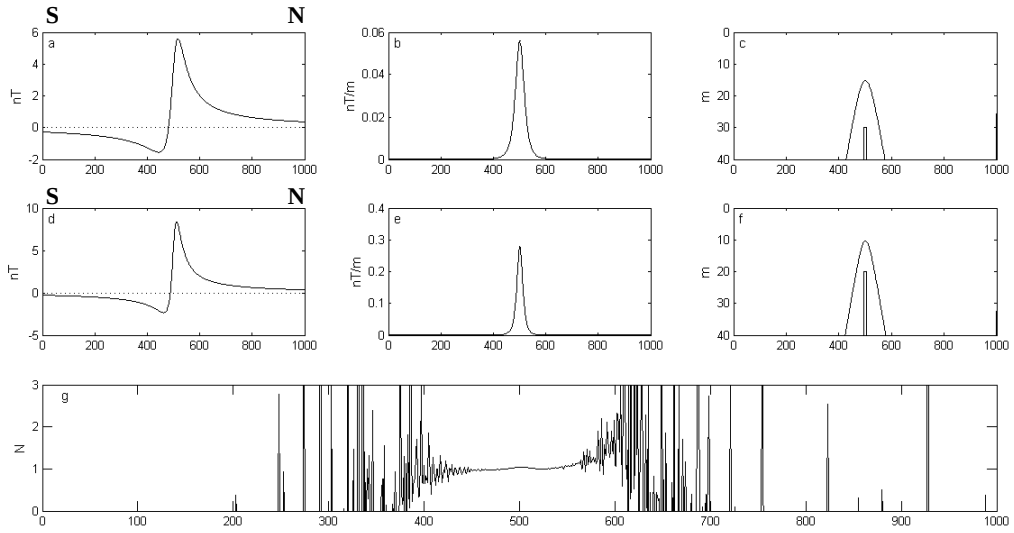


Figure 6.2 Conceptual application of the analytic signal fall-off rate method applied to two vertical (5 m thick) dykes. a, b, c: The total magnetic field, the analytic signal amplitude and the distance to source of the dyke located at a depth of 30 m respectively. d, e f: The total magnetic field, the analytic signal amplitude and the distance to source of the contact located at 20 m depth respectively. g Structural index estimation.

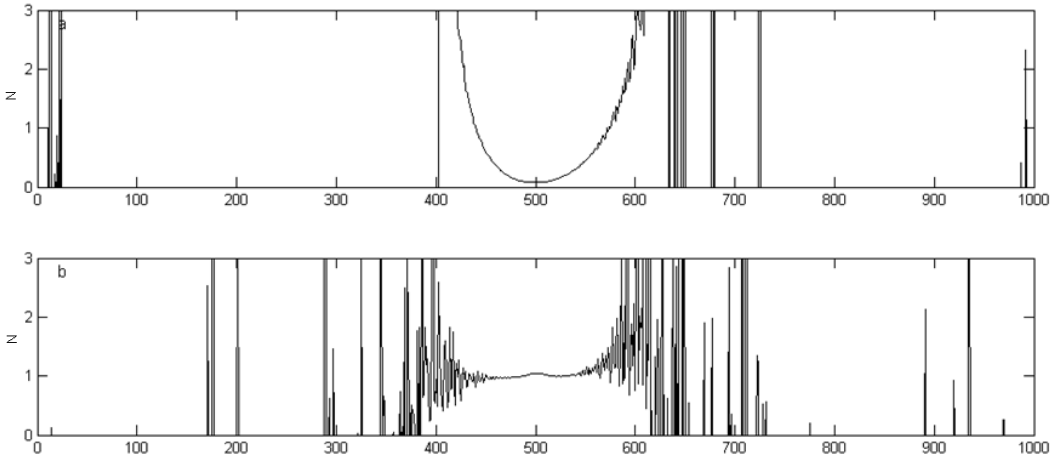


Figure 6.3 Estimation of the structural index over both a contact (a) and a dyke (b) located at a depth of 20 m by making use of the analytic signal fall-off method. An upward continuation height of 5 m was used between the two data elevations.

The gridded theoretical anomalies over a north-south striking vertical contact and dyke (width 5 m), both located at 20 m below the surface, were then calculated to assess the applicability of the method to gridded data. The local field inclination and declination were set to -70° and 0° respectively. Stable structural index estimations and accurate rescaled distance to source values (see Figure 6.4) were obtained, although there are edge effects in the structural index estimation for the contact model. An upward continuation height of 10 m was used between the two datum elevations. Applying this method to non-RTP data and obtaining expected results indicates that this approach can be used for bodies that possess remnant magnetisation or non-vertical dip, in line with the description by Cooper (2014) on the applicability of the distance to source method.

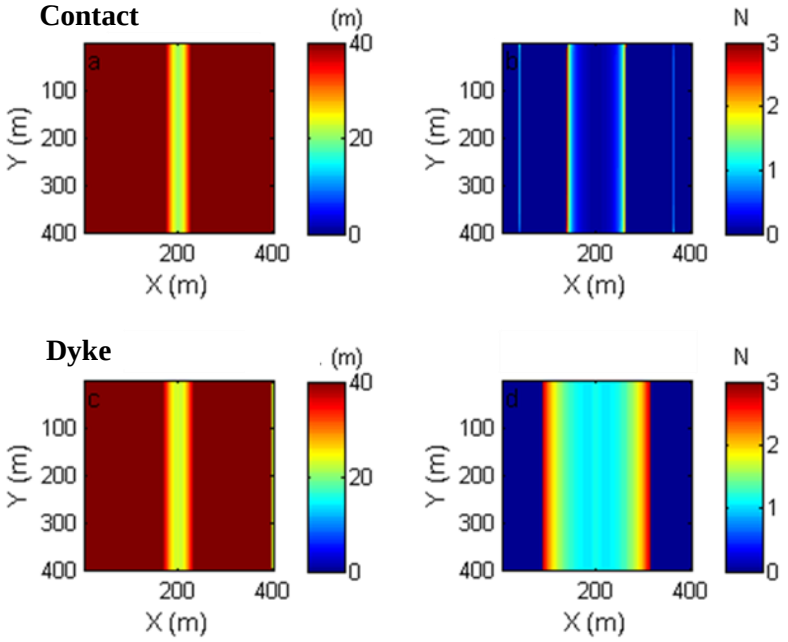


Figure 6.4 Rescaled distance to source and structural index estimation for gridded data over a contact and dyke. a) Rescaled distance to source over a contact located at 20 m below the surface. b) Estimated structural index over the contact (true N = 0). c) Corrected distance to source over a dyke located at a depth of 20 m. d) Estimated structural index over the dyke (true N=1). The local inclination was set to -70° with a declination of 0°.

6.3 The effect of interfering anomalies on the results

In the general case magnetic data contains contributions from multiple magnetic sources. Ideally these individual sources are separated by sufficient distance to be easily identified, but often sources are close together resulting in interference. The analytic signal fall-off

method was tested to assess how the interference between two different bodies affects the results.

A model of two vertical contacts was constructed by considered. The first was set at a depth of 25 m while the second was set at a depth of 40 m with a local magnetic field inclination of -80° and a declination of 0°. The two contacts were initially separated by a distance of 500 m (see Figure 6.5) the rescaled distance to source was then calculated and compared to the results obtained by applying the distance to source method (Cooper, 2014). Filtering of the distance solutions was done by rejecting those solutions associated with structural index values outside of the range of [0, 3]. Figure 6.5 shows that the calculated solutions correlate well to those calculated by the distance to source method (Cooper, 2014) for a separation distance of 500 m.

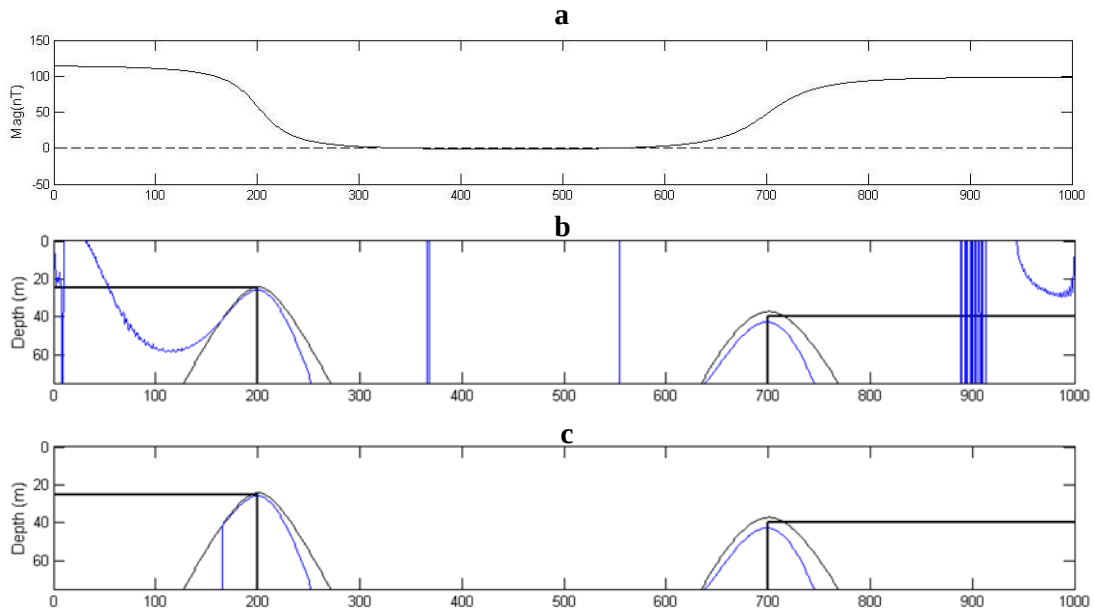


Figure 6.5 Rescaled distance to source estimations over two contacts separated by 500m. The local field inclination and declination were set to -80° and 0° respectively. a) Calculated magnetic field. b) The distance to source via the analytic signal amplitude based method (Cooper, 2014) is given in black for comparison. c) Filtering was based on rejecting distance to source solutions associated with calculated structural index values outside of the range of [0, 3]. The thick black line shows the outline of the two contacts.

The two contacts were then modelled with a separation of 100 m (Figure 6.6). The resultant rescaled depths are greater than the true depths of the contacts, however this difference is comparable to the underestimation in depth when the distance to source method (Cooper, 2014) is applied. Therefore the conclusion made is that the analytic signal amplitude fall-off method shows no degradation to the effect of interfering bodies compared to the conventional distance to source method.

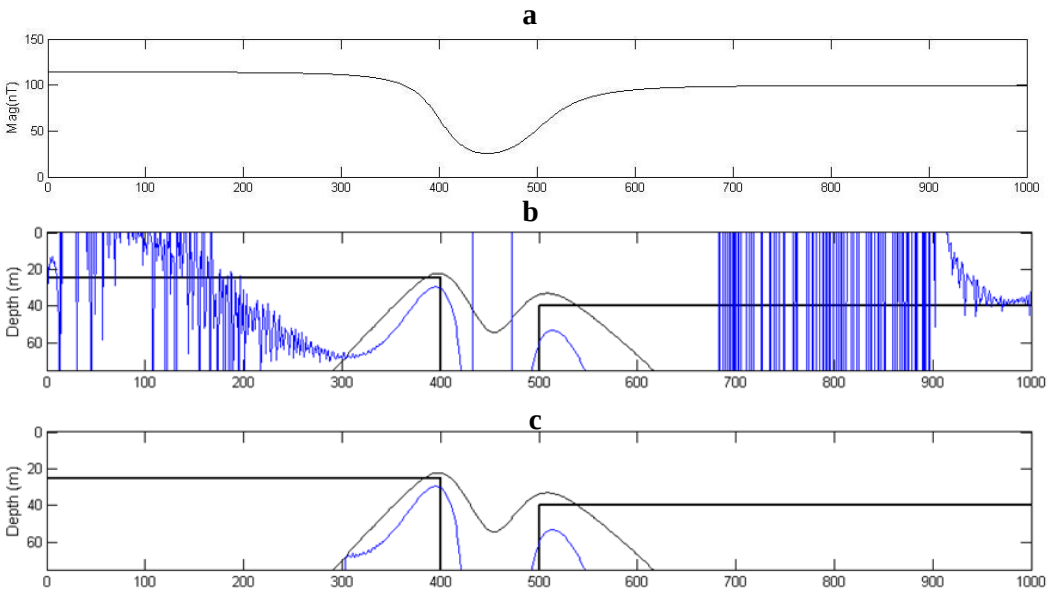


Figure 6.6 Rescaled distance to source estimations over two contacts separated by 100m. The local field inclination and declination were set to -80^0 and 0^0 respectively. a) Calculated magnetic field. b) Rescaled distance to source estimations, the distance to source via the analytic signal amplitude based method (Cooper, 2014) is given in black for reference. c) Filtered rescaled distance to source estimations.

6.4 The effect of noise in the signal on the results

Real world data are inherently corrupted with noise to a varying degree. The previous model of two vertical contacts separated by a distance of 500 m was again used however this time the data were corrupted with 0.1% random Gaussian noise.

The distance to source (Cooper, 2014) and filtered rescaled distance, based on acceptable structural index values (0 to 3), were compared to one another (Figure 6.7). While the distance to source solutions show clear maxima over the edges of the contacts the solutions are somewhat noisy. The filtered rescaled distance to source estimate is again noisy but has a distinct clustering around the edges of both contacts.

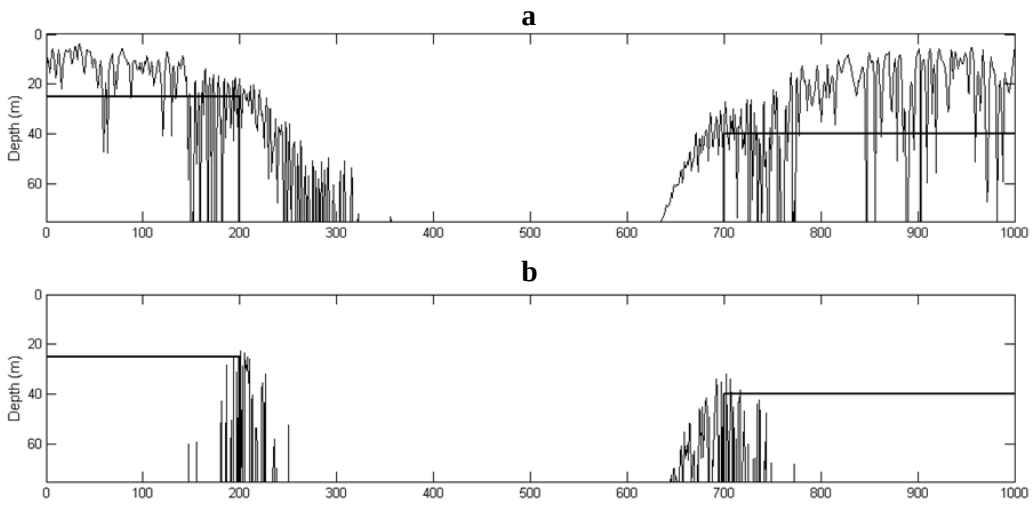


Figure 6.7 The effect of adding 0.1% random noise to the calculated two contact model previously discussed. The corrected distance to source (given in a) after applying the filtering (given in b) based on the structural index (valid solutions in the range 0 to 3) clearly shows two clusters roughly around the true location of the

6.5 Improved Euler solutions based on employing the estimated structural index

The commonly applied Euler deconvolution method requires the user to define the structural index prior to its application. Choosing the correct structural index to describe the source has been the greatest limitation to applying Euler deconvolution (Barbosa et al., 1999). The general approach is to analyse the data with a range of structural indices and then choose the structural index to represent the source based on the tightest clustering of solutions (Thompson, 1982, Reid et al., 1990).

Since the proposed method solves for the structural index of the source this output can be used in making use of Euler deconvolution (with each point along the profile having a calculated structural index) making it a fully automatic process. This concept was applied to theoretical data with different structural indices namely a dyke and a contact located along a profile. The dyke was located at a depth of 15 m whilst the contact was located at a depth of 30 m.

Figure 6.8 shows the results of this approach, the black crosses indicate the conventional Euler solutions with a structural index of 0 and the red crosses indicate the Euler solutions where the structural index has been calculated using the results in Figure 6.8b. For both datasets a window length of 12 samples was used.

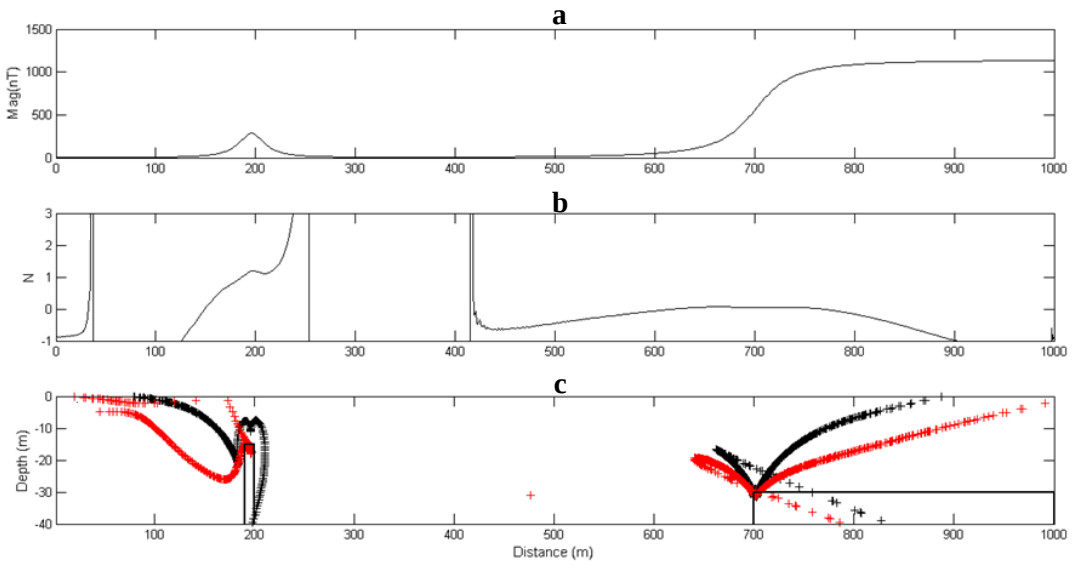


Figure 6.8 Euler deconvolution using calculated structural index values. a) the calculated magnetic field over a magnetic dyke located at a depth of 15 m and a contact located at a depth of 30 m with a local magnetic field inclination of -90°. b) Variation of the estimated structural index along the profile using Equation 4. c) Euler solutions using a window length of 12 samples, black crosses – convention Euler deconvoulution using a structural index of 0, red crosses - Euler solutions based on calculated structural indices for the profile (given in b). The black lines indicate the outlines of the bodies.

Conventional Euler deconvolution shows a tight clustering of solutions around the contact but a more disperse distribution around the dyke, as is expected given that a structural index of 0 was used. The Euler deconvolution solutions associated with defined structural index values based on the analytic signal fall-off method (red crosses) show a tight clustering around the true location of both the dyke and the contact.

The same approach was then applied to theoretical gridded data over the corner of an infinite prism located at a depth of 30 m with a local field inclination of -80° (Figure 6.9). The generated Euler solutions, after applying the method show a good clustering around the true location and depth of the source. Whilst this clustering is not as tight as those obtained using a structural index of 0, they are considerably closer than when a structural index of 1 is employed.

Structural index estimations that were less than 0 or greater than 3 were made transparent for display purposes but were still used in the calculation of Euler solutions to illustrate

the simple applicability of this method. Hence many of the solutions far from the true location of the prism could still be easily rejected based on filtering, by rejecting depth estimates associated with structural index values outside the expected range.

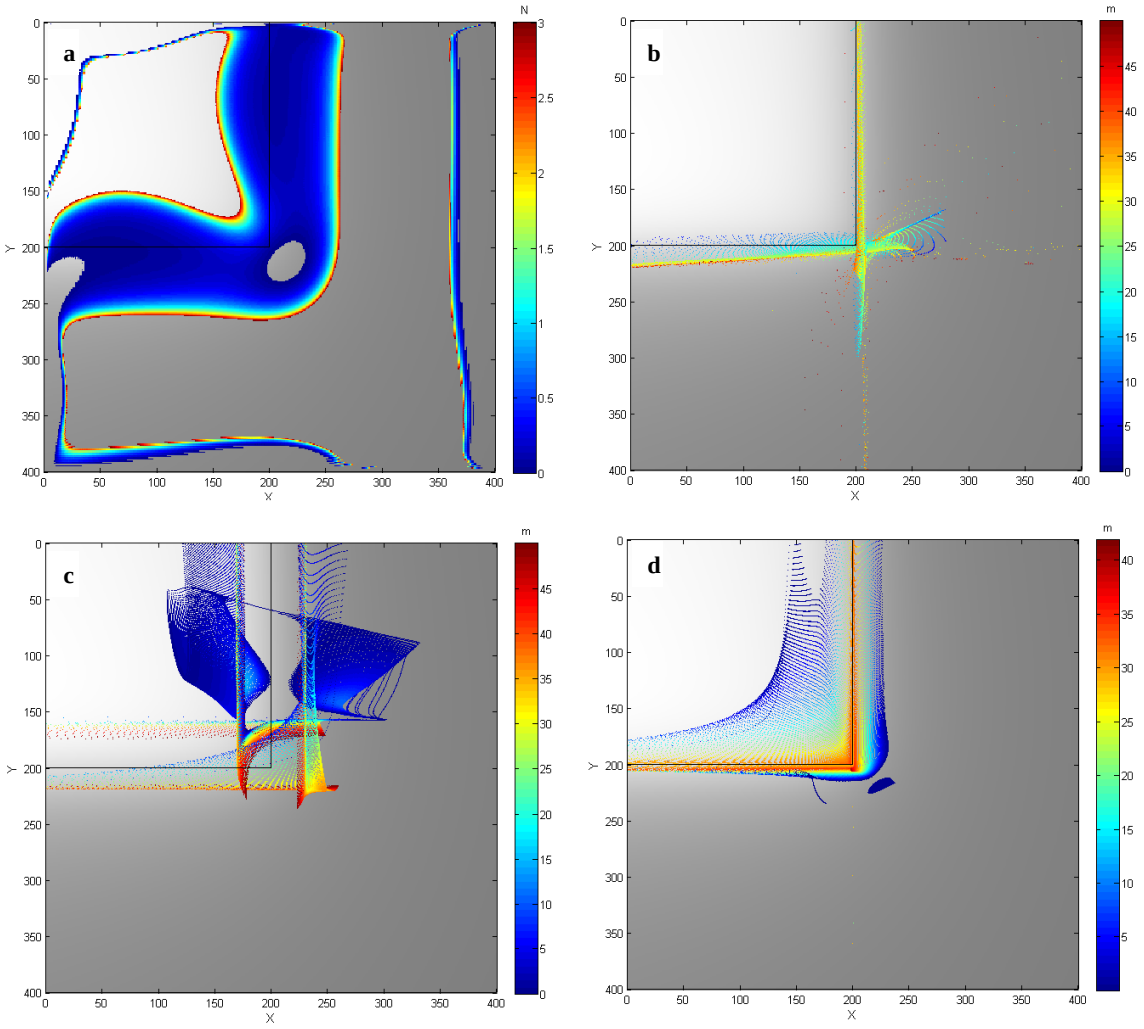


Figure 6.9 Semi-automatic and automatic Euler deconvolution applied to theoretical gridded data. a) Structural index estimation over the corner of an infinite prism located at a depth of 30 m with a field inclination of -80°. b) Automatic Euler solutions showing moderate to tight clustering around the edge of the prism. c) Euler solutions generated with an assumed structural index of 1. d) Euler solutions generated with an assumed structural index of 0. The outline of the body is given in black whilst magnetic field of the prism is shown in the background in gray.

Chapter 7 – Unconstrained depth and structural index inversion, using the variation in distance to source observed from two different elevations

7.1 Structural index independent depth determination

By observing potential field data from two different elevations separated by a distance equal to Δz, with the distance to source given by R, as observed from the lower elevation and R_{up}, as observed from the higher elevation, the following ratio can be formulated from first principles:

$$\frac{R}{R_{up}} = \frac{\sqrt{(x-x_0)^2 + (y-y_0)^2 + (z-z_0)^2}}{\sqrt{(x-x_0)^2 + (y-y_0)^2 + (z-z_0+\Delta z)^2}} \tag{7.1}$$

where x and z are the points of observation from the source and x_0 and z_0 locate the source. In practice the data need not be acquired at two different elevations since, through the process of upward continuation, the data acquired at one elevation above the source can be transformed into what would be observed at a higher elevation. Substituting the expression for the distance to source based on the first and second order analytic signal amplitudes (Cooper, 2014) into equation 7.1 and simplifying gives (Cooper and Whitehead, 2015):

$$\frac{R}{R_{up}} = \frac{\frac{(N+1)As}{As_2}}{\frac{(N+1)As_{up}}{As_{2up}}}$$

$$\frac{R}{R_{up}} = \frac{AsAs_{2up}}{As_2 As_{up}} \tag{7.2}$$

where As_{up} and As_{2up} are the first and second order expressions for the analytic signal amplitude calculated on the higher datum. For positions directly over the source (where $(x-x_0) = 0$) substituting equation 7.1 into equation 7.2 and simplifying gives:

$$\frac{(z-z_0)}{((z-z_0)+\Delta z)} = \left.\frac{AsAs_{2up}}{As_2 As_{up}}\right|_{(x-x_0)=0} \tag{7.3}$$

Solving equation 7.3 for the depth to source directly over the body yields:

$$(z - z_0)_{(x-x_0)=0} = \frac{\Delta z \left(\left. \frac{AsAs_{2up}}{As_2 As_{up}} \right|_{(x-x_0)=0} \right)}{\left(1 - \left. \frac{AsAs_{2up}}{As_2 As_{up}} \right|_{(x-x_0)=0} \right)} \tag{7.4}$$

Hence given data at two different elevations separated by a distance of Δz above a magnetic source the depth of the source can be calculated independently of the structural index by making use of equation 7.4. This method differs from that suggested in Chapter 6 in that the depth of the source is calculated independently of the structural index. Determining the structural index is only done to identify results located directly over the source (since for such positions it is assumed that N is between 0 and 3) and there is no rescaling of depth / distance solutions based on the calculated value of the structural index.

7.2 Unconstrained structural index determination

Since the structural index acts as a proportionality constant in the distance to source formulation (Cooper, 2014), dividing equation 7.4 by the conventional distance to source (assuming a structural index of 0) for positions directly over the source (Cooper and Whitehead, 2015) yeilds:

$$N_{x=0} = \frac{(z - z_0)_{(x-x_0)=0}}{R_{(N,\ (x-x_0))=0}} - 1 \tag{7.5}$$

where $R_{(N,\ x)=0}$ is the distance to source assuming a structural index of 0 and $z_{(x-x_0)=0}$ is calculated using equation 7.4. Cooper and Whitehead, (2015) show that calculating the structural index in this manner and rejecting solutions that exist outside the expected values acts as a good rejection filter of superfluous solutions if present away from the body.

7.3 Application of the distance to source variation method to theoretical data

The anomalous magnetic field over a thin vertical dyke located midway along a 1000 m north-south profile at a depth of 20 m was calculated (Figure 7.1a). The local inducing

magnetic field had an inclination of -60° and a declination of 0° with the dyke having a susceptibility of 0.01 (SI). The data were then upward continued by a height of 20 m and the distance to source was then calculated under the assumption of a $N = 0$ source. Equation 7.4 was then used to calculate the depth of the source, independently of the structural index. Figure 7.1b shows that multiple solutions were obtained at distances away from the true horizontal location of the dyke. The structural index was then estimated over the profile in its entirety by making use of equation 7.5 (Figure 7.1c). Since the structural index for magnetic sources are expected in the range [0, 3] depths at locations associated with structural index values outside that range were rejected. The filtered solutions are presented in Figure 7.1d.

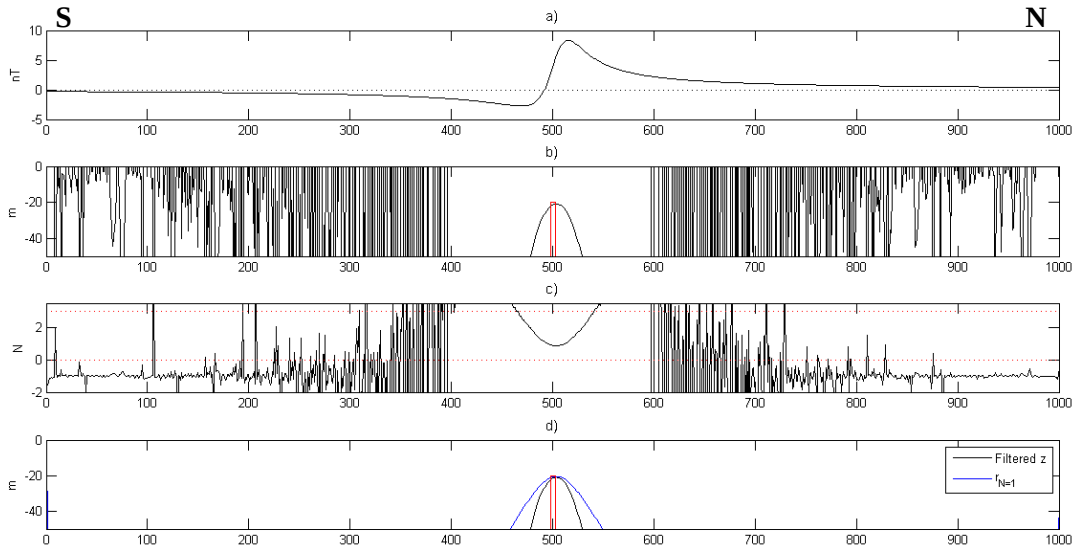


Figure 7.1 Application of the variation in distance to source method over a thin dyke located at a depth of 20 m. a) magnetic field with an inclination and declination of -60° and 0° respectively over the dyke. b) non-filtered depth of source. c) structural index variation with acceptable structural index values contained within the dotted lines. d) filtered depth solutions (filtering based an rejection of depth solutions associated with structural index values outside of the range of 0 to 3), shown in black, and distance to source (Copper, 2014), shown in blue (calculated with a structural index of 1).

7.4 The effect of noise on determining the depth to source

The previous vertical dyke model was then corrupted by 2% random Gaussian noise and the non-filtered depth results were compared to the distance to source obtained from

employing the method proposed by Cooper (2014) using the correct choice of structural index ($N = 1$). Both methods show comparable susceptibility to noise (Figure 7.2), with accurate distance and depth estimates observed directly over the body.

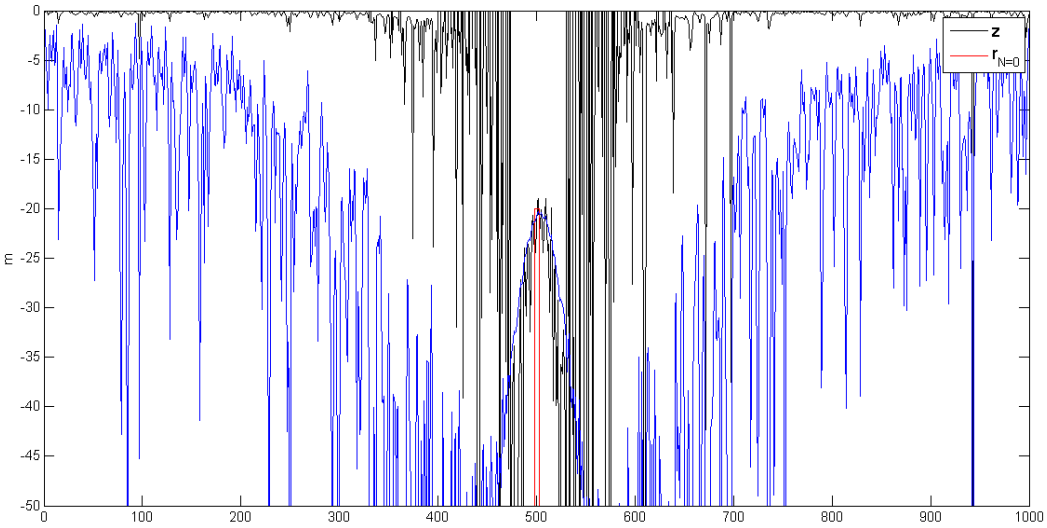


Figure 7.2 The effect of adding random 0.02% noise to the model previously discussed. The blue line indicates the distance to source estimate using the method proposed by Cooper (2014) with a structural index value of 1 (appropriate for a dyke). The black line indicates the unconstrained unfiltered depth solutions obtained by making use of equation 7.4.

This therefore indicated that the method has a similar susceptibility to noise compared to the source-distance method (Cooper, 2014). However, this method has the advantage that there is no need to specify structural index values and also provides a means to filter the data through the rejection of depth solutions associated with structural index values outside of the range of 0 to 3.

Chapter 8: Application to Total Magnetic Intensity Data Collected Over the Kuruman Military Area, Northern Cape South Africa (Description of the Geology and Available Geophysical Datasets)

8.1 Regional geology of the Kuruman Military Area – The Transvaal Supergroup

Located in the Northern Cape of South Africa, the Kuruman Military area comprises of rocks from the Transvaal Supergroup, overlain by later Quaternary sand cover (Erikson et al., 2006, Astrup et al., 1998, SACS 1980). The Transvaal Supergroup is subdivided into two distinct regions representing two similar paleo-depositional settings (Figure 8.1). To the east, deposition occurred into what is now known as the Transvaal basin with the equivalent basin to the west being termed the Griqualand Basin (Erikson et al., 2006, SACS, 1980). Division of the Transvaal Supergroup into these two sub-basins occurred along the north south trending Lobatse arch that propagated southwards from the southern border of Botswana (Carincross et al., 1997), exposing the underlying basement and subdividing the Transvaal Supergroup (Figure 8.1). The base of the Transvaal Supergroup is represented by a thin unit of quartzite referred to as the Vryberg formation in the west and as the Black Reef formation in the east. This in turn is overlain by a thick sequence of carbonates and ironstones known as the Chaap Group in the western Griqualand Basin and the Chuniespoort Group where it occurs in the eastern Transvaal basin (Caringcross et al., 1997, Erikson et al., 2006). Following the deposition of the Ghaap Group, deposition of both the Griquatown group, consisting of the Asbestos Hills, Koegas and Gamagara formations occurred (SACS, 1980). The final unit to have been deposited consists largely of quartzite and shale with minor dolomite and iron formations, in the west (the Grigualand Basin) this final unit is termed the Postmasburg Group (formerly known as the Cox Group (SACS, 1980)) whilst in the east (the Transvaal basin) it is termed the Pretoria Group (Erikson et al., 2006). The western Posmasburg Group is of significant economic importance since it hosts the Kalahari Manganese deposits (Astrup et al., 1998).

Deposition of the Transvaal units began at 2600 Ma and concluded by ~2200 Ma (Caringcross et al., 1997). The later deposition of the red beds of the overlying Olifantshoek Group in the Griqualand west region occurred at ~1800 Ma over a regional unconformity. This presence of this unconformity was key in the supergene enrichment process that upgraded the manganese and iron deposits to ore grades in the Posmasburg group (Caringcross et al., 1997, Astrup et al., 1998). In the east the 2100 Ma Rooiberg

Felsite and Dulstroom Lavas concluded deposition of the Transvaal supergroup (Caringcross et al., 1997).

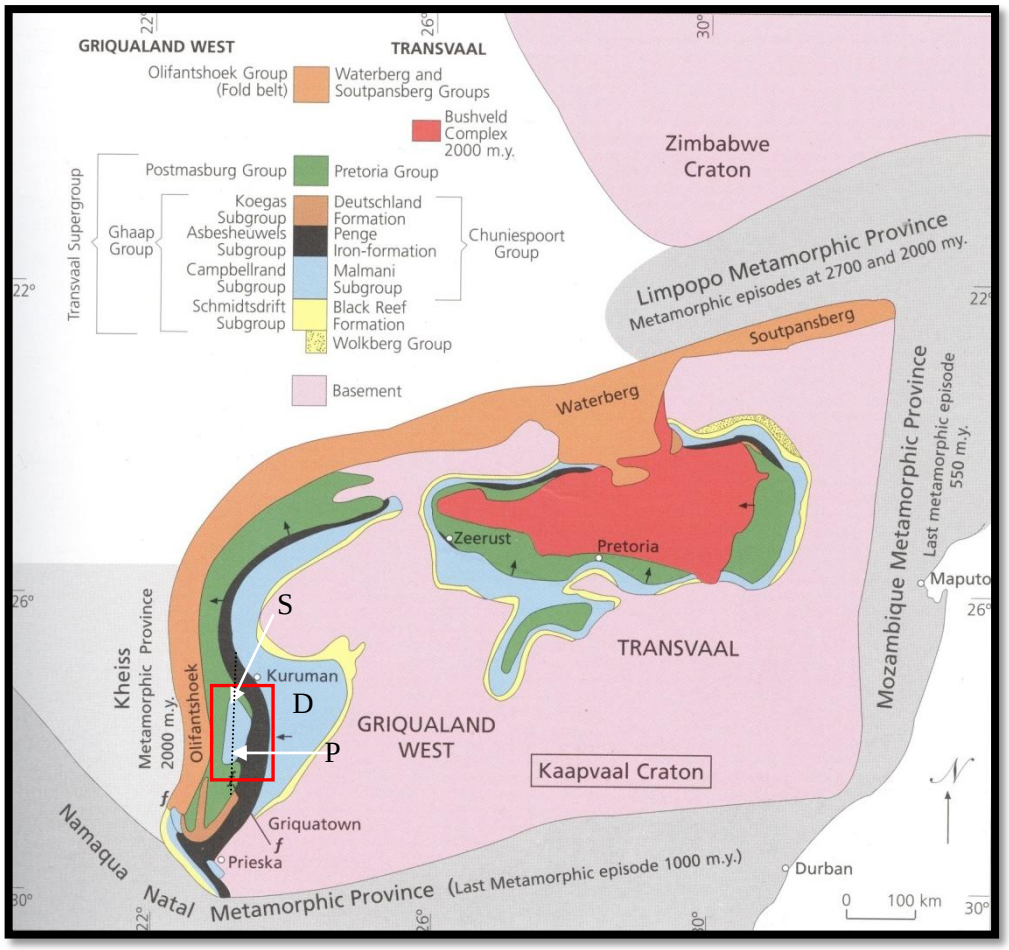


Figure 8.1 Simplified geology of the Transvaal Supergroup. Deposition of the Transvaal group occurred in the Transvaal basin to the east, whilst in the west it occurred in the Griqualand basin, division into the two basins occurred along the north south trending Lobatse arch. The boundary of the Kuruman Military Area is given in red (Cairncross et al. 1997). S, D, P show the locations of Sishen, Dimoten syncline and Postmasburg respectively while the dotted line indicates the Maremane dome axis.

The Kuruman Military Area rocks were gently folded the strata into a sequence of syn-forms and anti-forms prior to the deposition of the Olifantshoek Group. The Kalahari Manganese field was preserved along the Dimoten syncline whilst the manganese and iron ore deposits between Sishen and Postmasburg to the East were preserved along the Maremane dome axis (Caringcross et al., 1997, SACS, 1980).

8.1.1 Nature of ore occurrence

The economic deposits of the Kuruman Military area occur in two regions, namely the Eastern and Western Postmasburg Belts. The eastern belt is located on the ridge of the Maremane dome whilst the western belt is located at the base of the Gamagara ridge off the western margin of the Maremane dome (Carincross et al., 1997) (Figure 8.2).

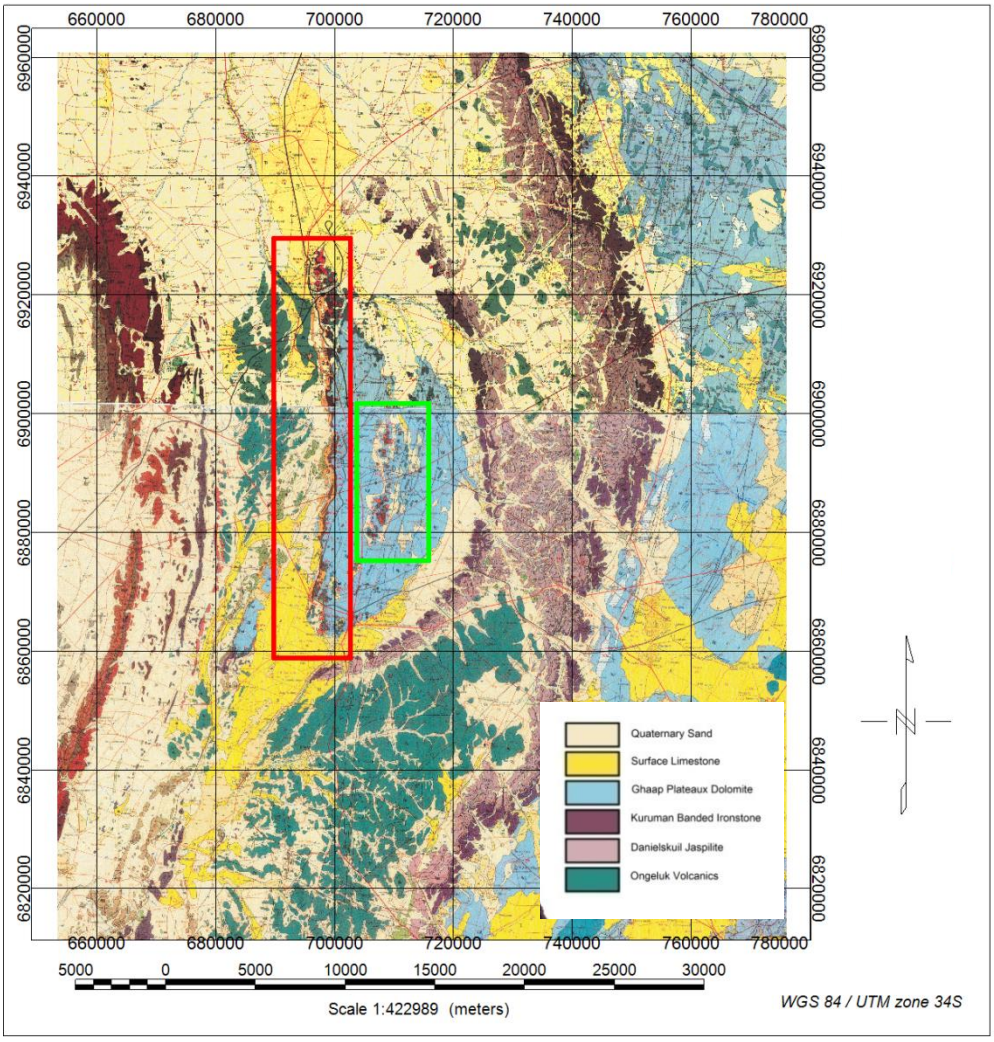


Figure 8.2 Geological map of the region indicating the extent of the western (red block) and eastern (green block) manganese belts. Geological map obtained from the Council of Geosciences, South Africa, (2014).

8.2 Geophysical datasets pertaining to the Kuruman Military Area

8.2.1 Magnetic Data Collection Parameters

Total magnetic field strength was recorded on an airborne platform through the using a Geometrics G8223A Caesium Vapour magnetometer over the Kuruman Military Area as part of a ground water investigation project conducted by Golder Associates Pty (Ltd). The region was subdivided into two survey blocks (Figure 8.3).

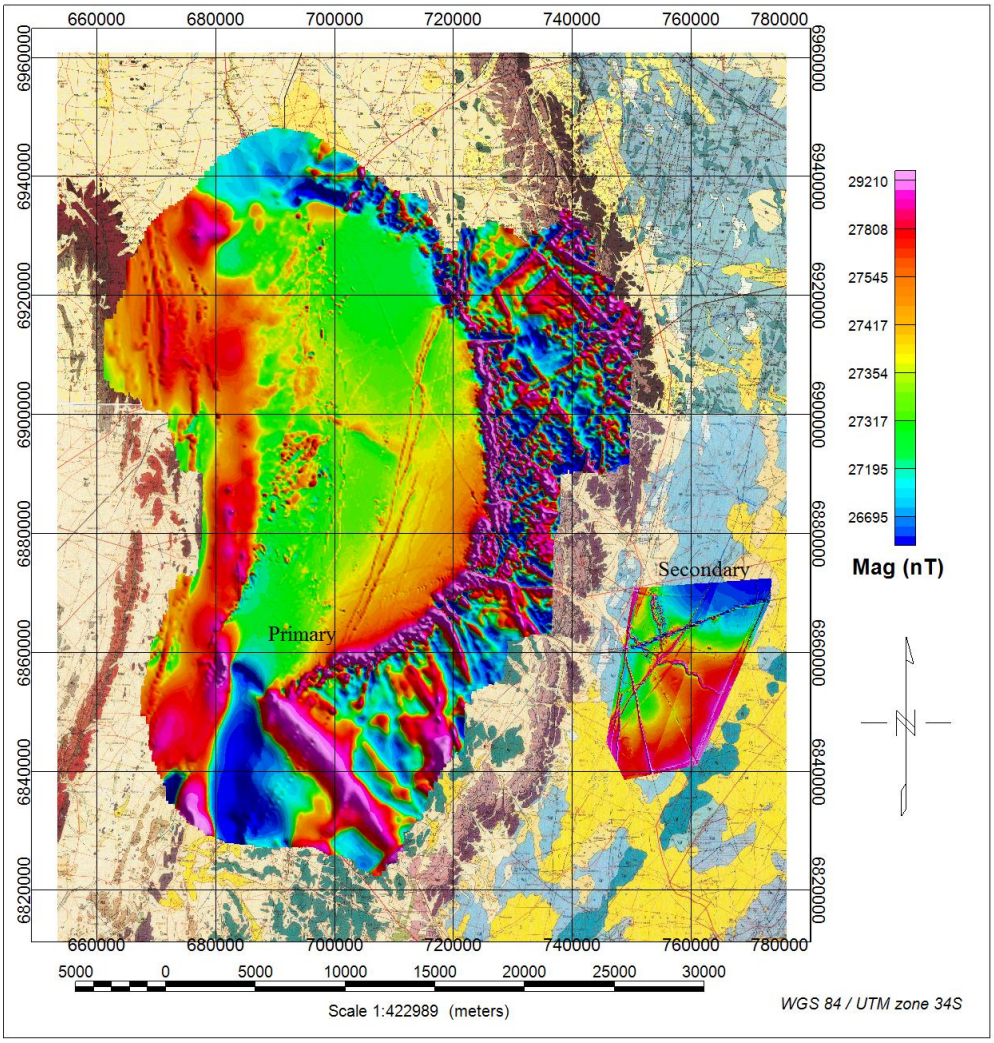


Figure 8.3 Total magnetic intensity map of the Kuruman Military Area, overlain on the geological map of the region, showing the location of the two survey blocks, namely the primary and secondary blocks.

The larger block is referred to as the primary region whilst the smaller block to the east is referred to as the secondary region. Flight lines for both the primary and secondary regions were orientated east-west (perpendicular to the strike of the mapped geology) and flown on a draped flight profile with an average of 50 m ground clearance. Time domain electromagnetic measurements were being conducted at the same time as the magnetic recordings hence the data is somewhat noisy.

The raw data for the primary block were not available however, the processed data were available on a grid interval of 125 m. The processed data for the secondary block was available and gridded on a tighter 20 m grid spacing. The grid spacing for the primary block and secondary block varied due to the flight line spacing used during the survey namely 250 m for the former and 50 m for the latter. The secondary block was flown to detect a thin paleo-channel and so was flown at much tighter line spacing than the primary block, which was aimed at giving a broader regional understanding of the area.

8.2.2 Interpretation of the TMI data over the primary and secondary blocks

The total magnetic intensity map of the primary region (Figure 8.3) has a distinctive arc shaped high anomalous feature extending from beneath the quaternary sand cover in the south through the town of Doornfontein in the east until it is again buried by quaternary sand cover in the north (north of Sishen). This feature correlates to the outcropping of the Kuruman banded ironstone member of the Asbesberge formation and has an absolute magnetic field strength in excess of 30000 nT. The Kuruman banded ironstone member varies in thickness between 180 m to 240 m and consists of interbedded chert, jasper and dark jasperlite. The jasperlite consists mainly of hematite, and limonite however it also contains magnetite, giving the high magnetic anomaly. The deep magnetic lows interspaced by the magnetic high ridges to the east of the map indicate faulting (Prof Stetller, Pers. Coms).

In the south of the primary region, the TMI map shows a distinct long wavelength anomaly striking roughly northwest. This feature has a magnetic strength value in the range of 28 000 to 29 000 nT. Its longer wavelength suggests that the source is located at a significant depth below the surface. Extension of this feature past the boundaries of the area of interest is not evident on the South African regional magnetic coverage map.

Contained within the concave arc, of the outcropping Kuruman formation, several north east striking linear cross cutting features can be identified. Whilst there is no distinct lithological change in association with these features, on the geological map they have been identified as possible dolerite dykes. A second set of north west striking dykes is also imaged, these are most evident in the secondary region but show only limited presence in the primary area. Along the central portion of the Maremane dome (near the centre of the TMI image), small circular to semi-circular scattered magnetic highs can be found. When the magnetic TMI map is compared to the geological map of the region these small semi-circular features correlate well to the occurrence of the Blinkklip and Wolhaarkop breccias. These breccias were deposited as the first sequence of rocks onto the ancient slump structures and form the lower part of the Manganore deposits that are currently being exploited along the Eastern Belt of the Posmasburg Manganese deposit (Geological map obtained from the Council of Geosciences, South Africa).

Figure 8.4 illustrates how these semi circular to circular magnetic anomalies can be correlated to the mapped geology as well as the surface topography. Similar features can be found to the north near Sishen.

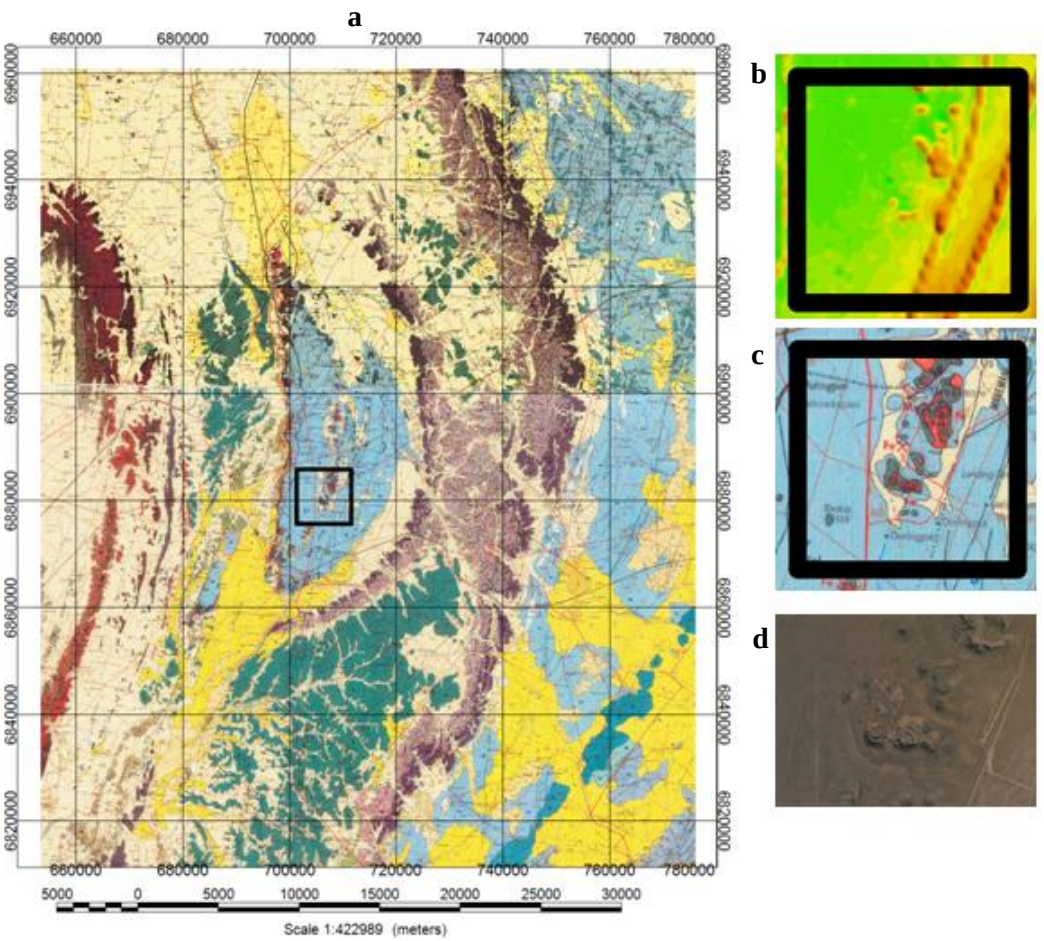


Figure 8.4 a) Occurrence of slump structures that host the economic Blinkklip and Wolhaarkop breccias that form part of the Manganore deposits (given in red on the geology map). b) Total magnetic intensity map of area indicated by the black rectangle, showing two north east trending dykes as well as scattered circular to semicircular features associated with the Manganore deposits. c) Geological map of the region under discussion, with the Manganore deposits given in red. d) satellite image of the region, showing circular topographic highs in association with the mapped geology (Google Earth, 2014).

8.2.3 Identification of cultural noise in the TMI data

The electric railway line that connects Sishen to Saldanha runs in a westerly direction from Blinklip in the east to Postmasburg. Upon reaching Postmasburg the railway line turns north and heads toward Sishen. This anomaly has a characteristic high frequency alternating high and low magnetic signature and thus can easily be identified. The railway line crosscuts both the primary and secondary regions of the Kuruman Military Area.

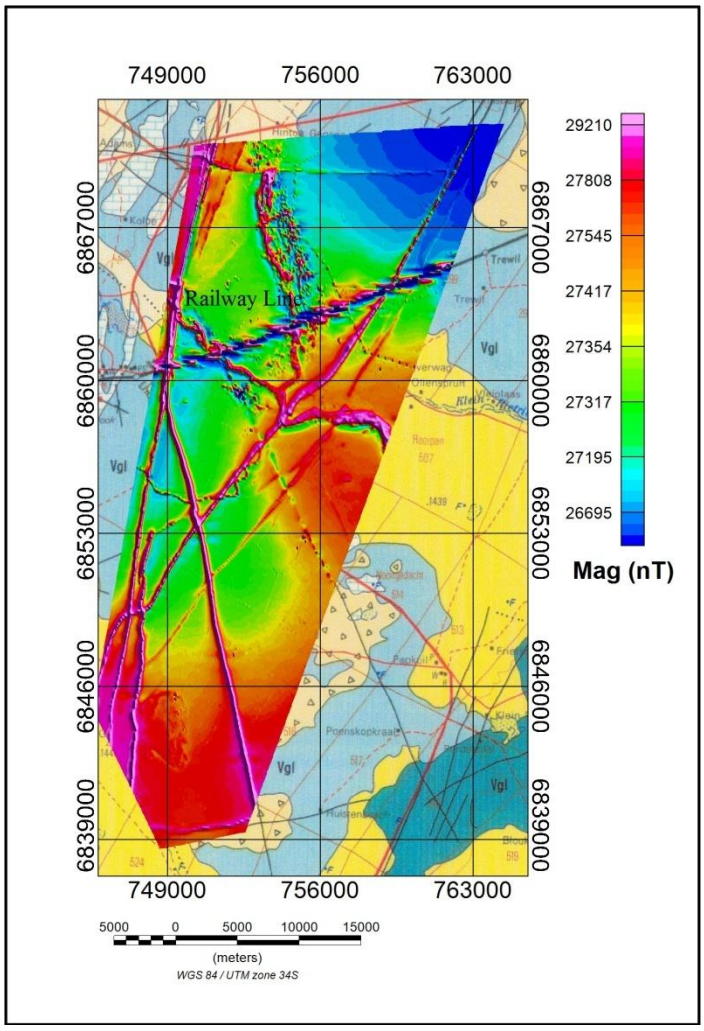


Figure 8.5 The electric railway line connecting Sishen to Saldahna causes considerable localised noise. In the secondary region this is clearly seen by the high frequency noise in the TMI data directly along the path of the railway line.

8.2.4 Topography of the Kuruman Military Area correlated to the mapped geology

Elevation data for the primary region were obtained from the freely available SRTM database. Figure 8.6, shows the regional elevation contained within 27°S, 22°E and 29°S,24°E at 90 m horizontal resolution. The outline of the primary region is given in black.

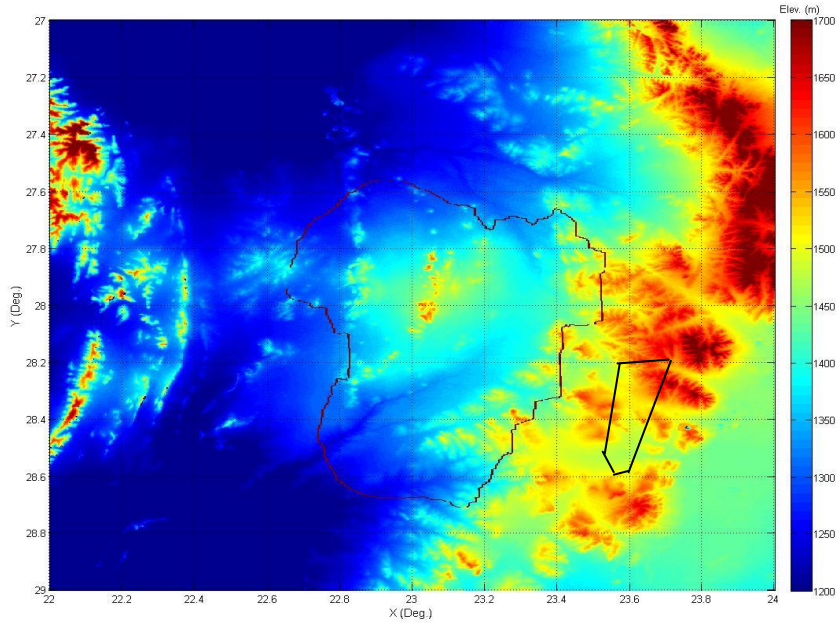


Figure 8.6 Shuttle Radar Topography Mission (SRTM) data of the region. The primary region of the Kuruman Military Area is outlined in black.

The Maremane Dome is located in the centre of the Figure with the majority of the dome being between 1400 and 1475 m above sea level (turquoise to pale green in colour). There are two distinct dendritic drainage patterns to both the north and the south of the dome, resulting in the lowest mapped elevations. To the east the outcropping of the Ghaap Plateau dolomites results in increased elevations, however this area is out of the bounds of the region of interest (the boundary of which is shown in black). The north-south striking Gamagara hills are contained just within the western margin of the area of interest. The Gamagarra hills extend beyond the northern boundary of the region of interest however are rapidly terminated by the drainage system located to the south.

Along the western margin of the area of interest the outcropping of the Kuruman and Danielskuil formations of the Asbesberge group cause the first increase in elevation off the western margin of the Maramane Dome trending in a concave arc fashion (refer to Figure 8.7).

In the central portion of the Maramane Dome isolated areas with higher elevations can be seen. These small areas occur as circular to sub-circular features and correlate well to the location of the western belt of the Posmasburg manganese field where deposits of both manganese and iron are found in elevated paleo-karst like structures that have resisted erosion.

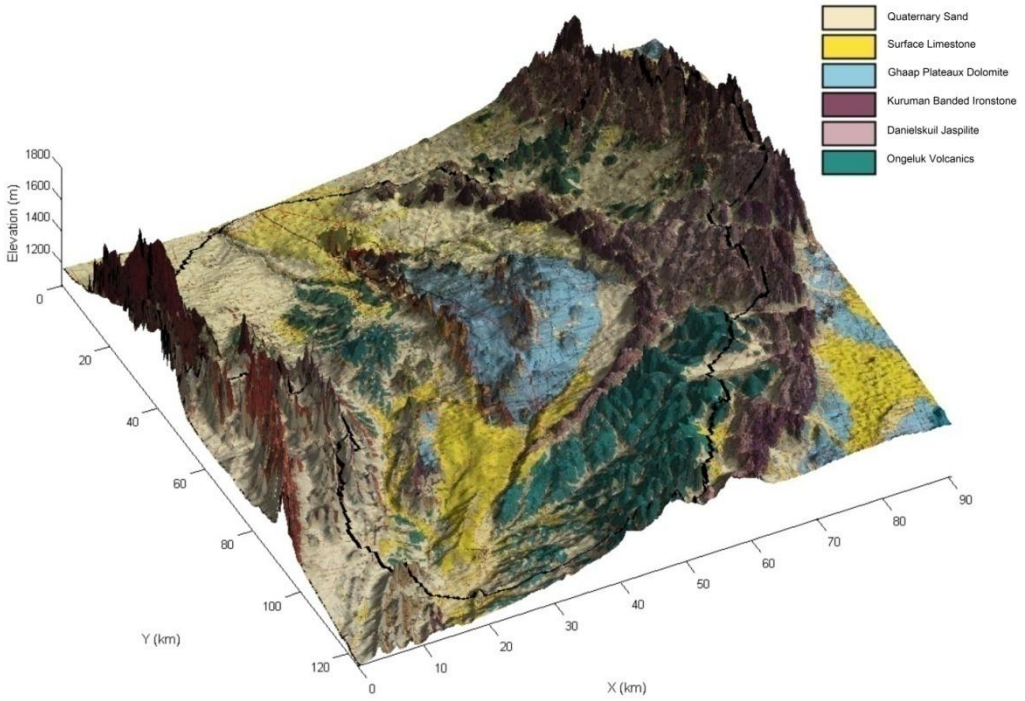


Figure 8.7 Surface elevation with the geology overlaid for the primary region. The outline of the primary region is given in black. Geological map obtained from the Council of Geosciences, South Africa (2014).

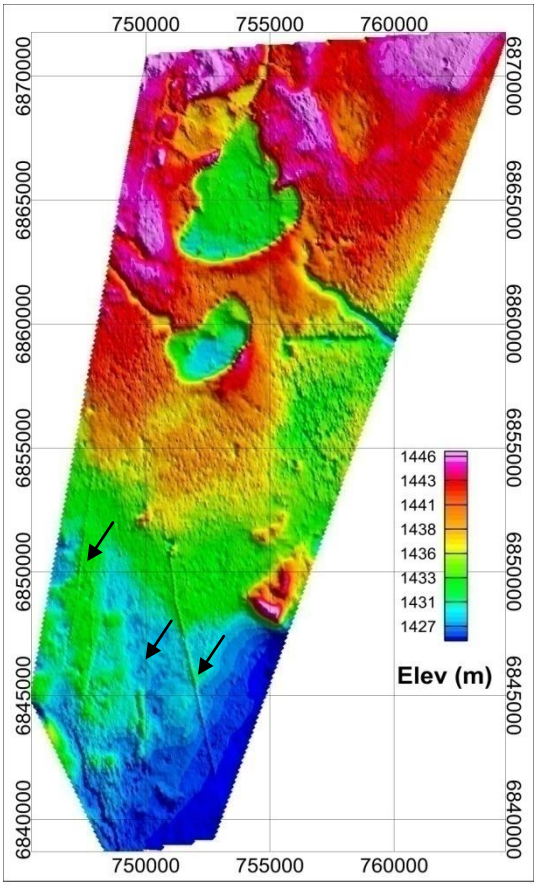


Figure 8.8 Elevation of the secondary region, data was collected in-flight through the use of a Optech/King laser altimeter. Several liner features can be identified that correlate to features on the TMI image of the region (Identified with black arrows).

The ground topography of the secondary region was obtained directly from the flight data through the use of an Optech/King laser altimeter. The mapped topography of the region is given in Figure 8.8. The region gradually slopes from the north west to the south east with an overall elevation change of around 30 m. In the south, extending from Y = 6840000 m to Y = 6845000 m (UTM zone 34S) there is a linear north south trending feature. This feature correlates well to a magnetic anomaly shown on the TMI map of the region, several other similar linear features can also be identified to the west of this.

The most notable features on the DTM of the secondary area are the two circular basins occurring to the north of the region. On the geology map of the region the northern basin is referred to as the Great Pan whilst the southern one is referred to as Rootpan.

Chapter 9: Application of the distance/ depth and structural index determination methods to the TMI data of the Kuruman Military Area, Northern Cape, South Africa

9.1 Application of the discussed methods to the Primary Area

9.1.1 Distance to source after Cooper (2014)

The total magnetic intensity (TMI) dataset of the primary region was used as input into the distance to source procedure described by Cooper (2014). The data were first upward continued to a height of 60 m above the flight level to reduce the effect of high frequency noise. The calculated distance to source was later reduced by 60 m after calculation to for this addition above the flight height. A structural index of 1 was used, hence the dykes present in the region would be imaged at the correct depth of occurrence. The calculated distance to source image is presented in Figure 9.1. Note, distance to source estimates in excess of 700 m were considered to represent locations sufficiently far from the true source as to be rejected (shaded in grey on the distance image).

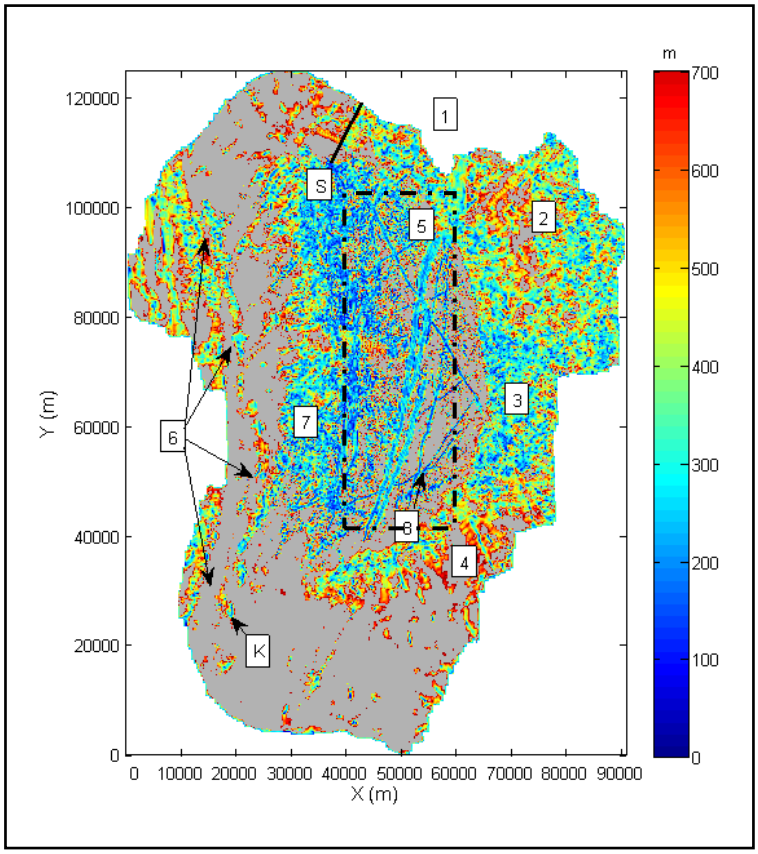


Figure 9.1 Distance to source estimation calculated via the method proposed by Cooper (2014) assuming all sources have a structural index of 1. The data was upward continued by 60 m prior to the calculation to reduce the effect of high frequency noise which was later subtracted from the output.

The distance to source solutions were then compared to the mapped geology of the region (Figures 8.4 and 8.7) to ascertain how the buried anomalies could be linked to the mapped geology. The following was determined to be notable, refer to Figure 9.1 for location of occurrence and note all distances / depths are relative to the sensor height on the platform (50 m):

1) The extension of the Maramane Dome north of Sishen beneath the later quaternary sand cover is evident. The northernmost and southernmost extensions of the Dome lie roughly north south with respect to one another. Where the magnetic Kuruman Banded Ironstone (purple on the geology map (Figure 8.7)) becomes covered by the quaternary sand (yellow on the geology map) there is an abrupt increase in the distance to source. This region may be affected by a fault (the strike of which is indicated on Figure 9.1 by a black line) along this contact down throwing the banded ironstone and allowing for the deposition of the sand cover above.
2) The Dimoten syncline with a mapped strike of NNW-SSE results in an increase in distance to source estimations as it depresses the magnetic Blinklip breccias and Kuruman Ironstones (shaded in dark and light purple on the geology map (Figure 8.7))) to greater depths below the surface under the non magnetic sand cover. Distances around 450 to 500 m were estimated.
3) At the fold axis of the Dimoten syncline, the Blinklip breccias, and Kuruman ironstones crop out hence distance to source estimates in the region are lower than to the north (~150 m deep as compared to 450 to 500 m).
4) To the south of the Dimoten fold axis the distance to source estimates increase to ~400 m. The syncline in this region is identified by the drendritic drainage pattern evident on both the geology map and elevation map (Figure 8.6) as erosion of the overlying Ongeluk andesitic lavas.
5) There is no evidence of the multiple imaged dykes on the geology map since they can now be estimated to occur at depth of ~200 m.
6) The mapped geology in this area contains sedimentary rocks (quartz and conglomerates with minor shales) and hence should not provide any magnetic signal. In the south there is a minor outcrop of the Kuruman banded ironstone (marked “K”). From this point north there is a clear lineament that maintains a constant depth (250 m) to the north until it is covered by sand. It is therefore

proposed that this lineament represents the western occurrence of the Kuruman Ironstone and Blinklip Breccias.

7) As expected distance to source estimations over the Maramane Dome are close to the flight height of 50 m.
8) The electric railway line presented previously as cultural noise is imaged as a shallow (< 60 m) feature on the distance to source map.

The two most prominent north south striking dykes in the region were then imaged to asses at what depth they occur (Figure 9.2, the location of the image with respect to the complete survey block is given in Figure 9.1 by the dashed block). The depth of the dykes was estimated between 70 and 110 m. If a flight height of 50 m is then corrected for the dykes occur at a depth between 20 and 60 m below the surface.

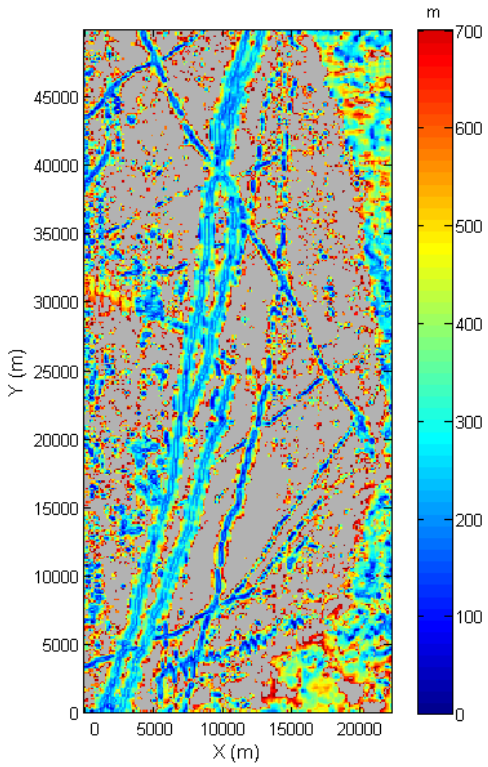


Figure 9.2 Distance to Source estimations over the two most prominent north south striking dykes in the primary region. The location of this figure with respect to the survey block is indicated in Figure 9.1 by the dashed box.

9.1.2 Structural index estimation over the primary region

Both the extended DEXP and the analytic signal fall-off methods were used to estimate the structural index variation over the primary area (Figures 9.3 and 9.4). Both structural index estimation methods failed to estimate the expected structural index values over the known geology, for example values close to 1 over the dykes, and hence were not used to calculate rescaled distance to source estimations. The reasons for this failure are likely due to inherently noisy data and possible aliasing since a gridding interval of 125 m was used.

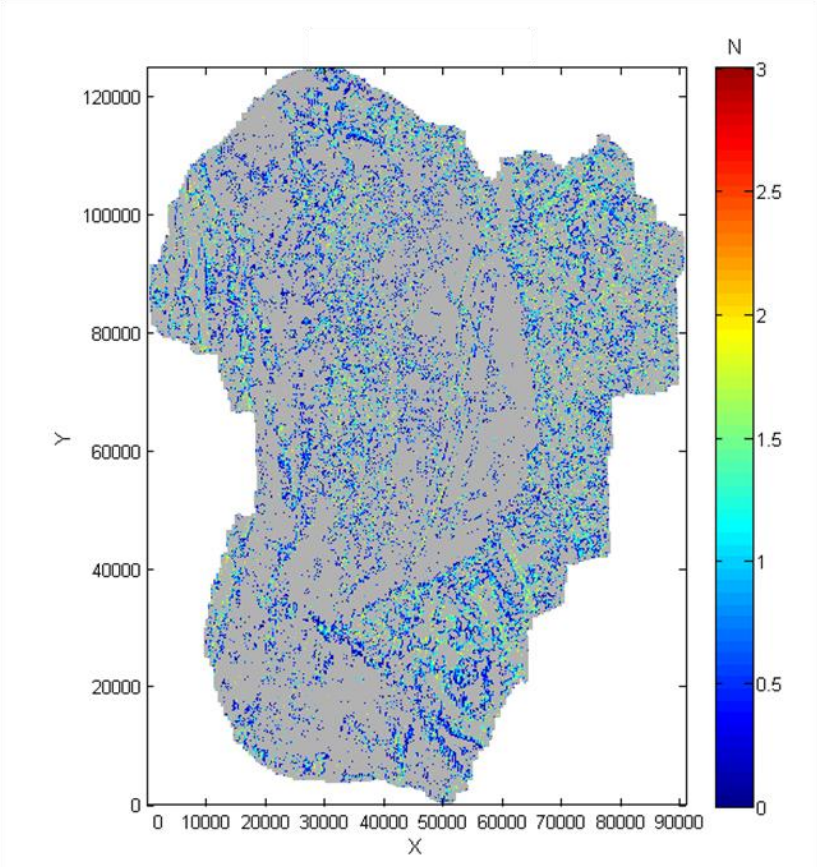


Figure 9.3 Structural index values estimated by making use of the analytic signal fall-off method over the primary region of the Kuruman Military Area, South Africa.

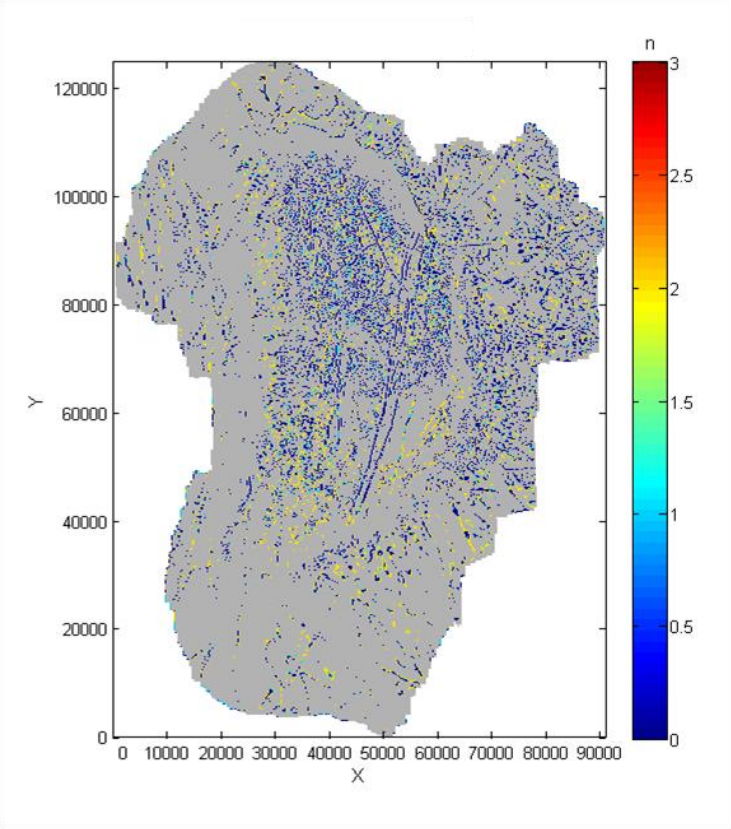


Figure 9.4 Structural index values estimated by making use of the extended DEXP method over the primary region of the Kuruman Military Area, South Africa.

The depth map shown in Figure 9.5 was produced through the use of the non-constrained depth inversion method presented in Chapter 7. Filtering of the calculated depth solutions was accomplished by rejecting depth solutions associated with estimated structural index values outside of what would be expected for magnetic data (i.e. outside of the range of [0, 3]). The rejected solutions are shaded in grey on the image. While the filtering has rejected many of the depth solutions, Figure 9.5 replicates the main trends imaged by assuming a structural index of 1 (Figure 9.1). For example the increase in depth either side of the Dimoten syncline fold hinge (indicated by "D" on Figure 9.5), the multiple dykes in the region as well as the overall shallower depths over the Maramane dome. It should also be noted that not only are these trends preserved but the depths at which the units occur, as shown on Figures 9.1 and 9.5, are also similar.

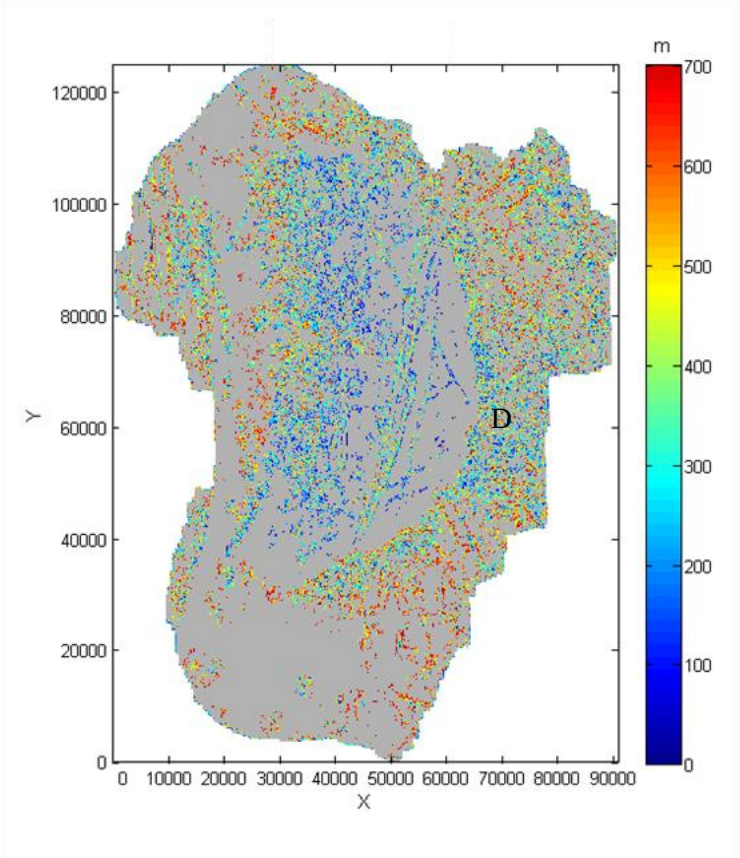


Figure 9.5 Depth image over the primary region using the non-constrained inversion method (presented in Chapter 7).

In the presentation of the multi-directional distance to source method (Chapter 5) the following two expressions for the horizontal location of the source were presented:

$$\frac{(x - x_0)}{(N+1)} = -\frac{As\frac{\partial As}{\partial x}}{{As_2}^2} \tag{9.1}$$

$$\frac{(y - y_0)}{(N+1)} = -\frac{As\frac{\partial As}{\partial y}}{{As_2}^2} \tag{9.2}$$

where x, y and N are the horizontal locations and structural index of the source respectively. Equations 9.1 and 9.2 can be combined to give a pseudo horizontal distance to source R_h, be it still dependant on the structural index, namely:

$$R_h = \sqrt{\left(\frac{(x - x_0)}{N + 1}\right)^2 + \left(\frac{(y - y_0)}{N + 1}\right)^2} \qquad (9.3)$$

For positions directly over the source, R_h tends to 0 irrespective of the value of N, therefore calculating the pseudo horizontal distance to source via Equation 9.3 results in a stable edge detection filter. R_h was calculated for the primary region (Figure 9.6) with solutions in excess of 30 m being rejected (i.e. sufficiently far from the source). The filter clearly delineates the complex nature of the dyke swarms over the Maramane dome.

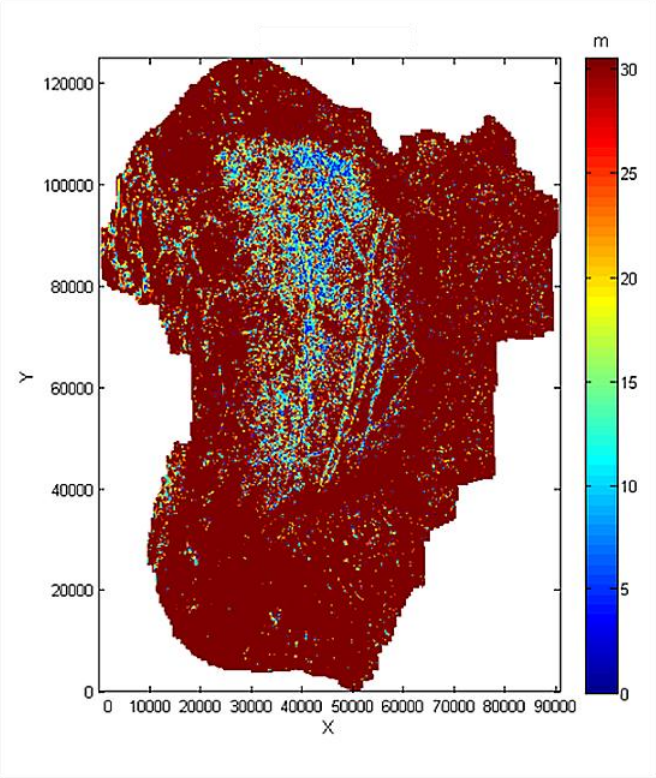


Figure 9.6 R_h calculated over the primary region delineating the complex nature of the dyke swarms over the Maramane dome. Solutions in excess of 30 m were rejected.

9.2 Application of the discussed methods to the Secondary Area

9.2.1 Initial interpretation of the TMI dataset

The most notable feature on the secondary area TMI image are the N-S, NW-SE and NE-SW striking dyke swarm. The dykes have been mapped on the surface geological map (Figure 9.8, black lines) but the extension of these dykes under the later Quatanary sand cover can now be confirmed.

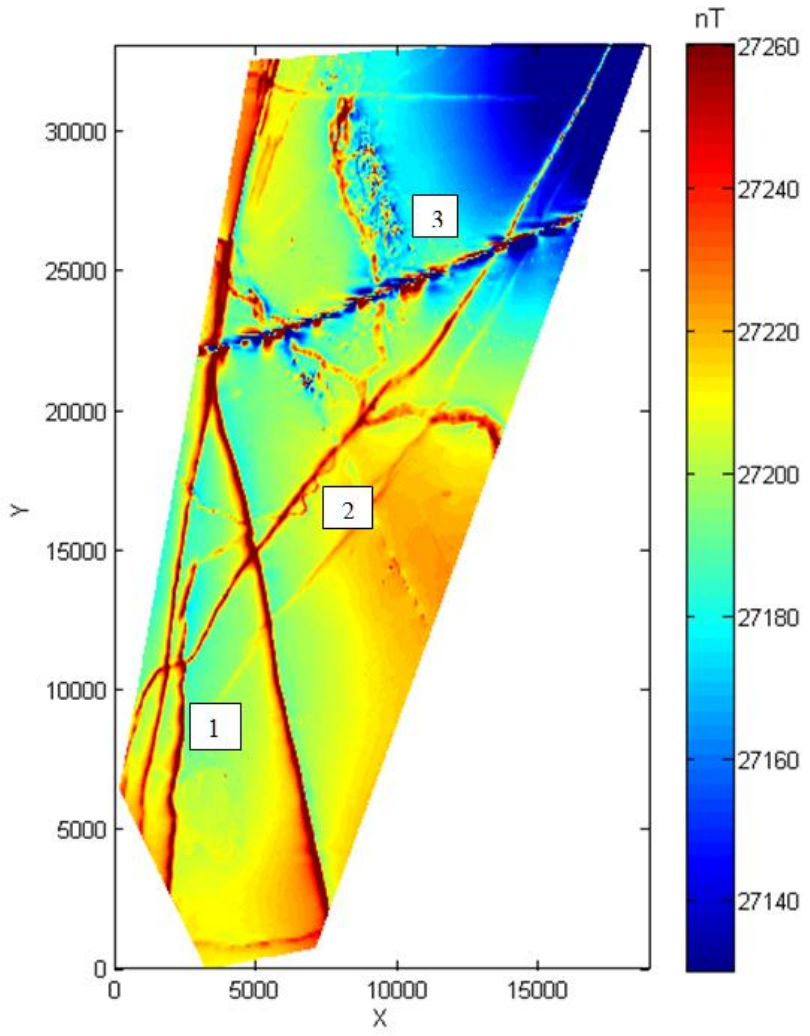


Figure 9.7 Total magnetic intensity (TMI) recorded over the secondary area, showing N-S, NW-SE and NE-SW propagating dyke swarms (1), paleo-river channel (2) and cultural noise due to an electric railway line (3).

Evidence of the outcropping of the dykes is also seen in the elevation image of the area (Figure 8.8). Two paleo-river channel systems are also imaged as short (~50 m) wavelength positive meandering magnetic features. The first of these channel systems propagates from the southwest to the northeast with the second from the northwest to the southeast.

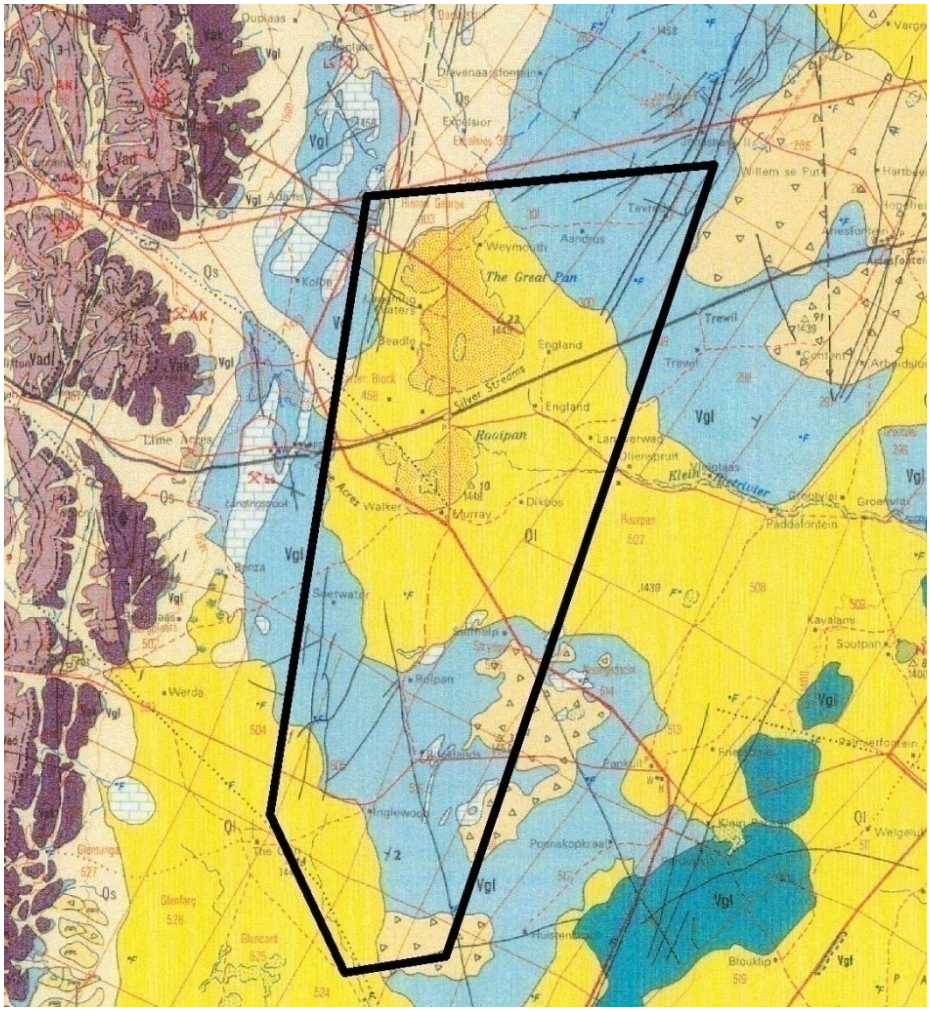


Figure 9.8 Geology map of the secondary region showing the mapped lithology and occurrence of dolerite dykes, drainage systems and cultural features. The outline of the secondary area given in black (map obtained from the Council of Geosciences).

The two river channels intersect around X=10000 m, Y=20000 m on Figure 9.7 (number 2). Whilst a paleo-river channel cannot in itself be magnetic the rocks deposited along the channel bottom may be, thus delineating the flow path of the channel. This is most likely the case since the rocks near the source of both river systems (the Kurman ironstones, indicated in purple on the geology map, Figure 9.8) are magnetic, and would be found in the river system as a product of erosion. These river systems show no correlation to the mapped surface drainage pattern and in fact occur under the Great Pan to the north and Rooipan to the south. This indicates that the paleo-river channels are older than the

drainage pans and may indicate that the area has undergone subsidence. The final magnetic feature of interest has a comparatively subtle expression on the TMI image and is located at X=4000 m, Y=5000 m (Figure 9.7 (number 1)). This feature is semi-circular to rectangular in shape and could be due to a buried sill located in the underlying dolomites (Stetller, Pers Coms).

9.2.2 Secondary Area - Calculation of distance to source and rescaled distance to source on profile data

Two east west trending profiles were extracted from the TMI image, the locations of which are shown in Figure 9.9. The distance to source (Cooper, 2014) and the rescaled distance to source were then calculated, by making use of a structural index of 1 in the former method and a structural index calculated by making use of the analytic signal fall-off method in the latter.

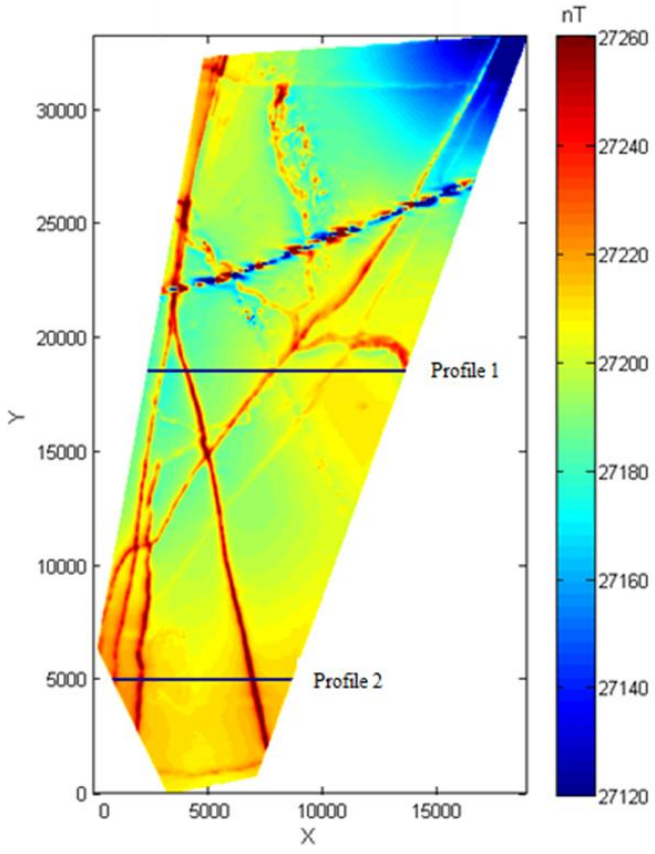


Figure 9.9 Location of the extracted profiles used for calculating the distance to source and the rescaled distance to source. A structural index of 1 was assumed for the distance to source method while the structural index was calculated by making use of the analytic signal fall-off method to rescale the distance to source.

The data were upward continued by 30 m prior to applying the two methods to suppress high frequency noise, this was then subtracted from the final distance to source estimates. A further 50 m of upward continuation was used to calculate the analytic signal amplitude and the distance to source at the higher datum needed to calculate fall-off of the structural index. The results are shown in Figures 9.10 and 9.11 for the two profiles.

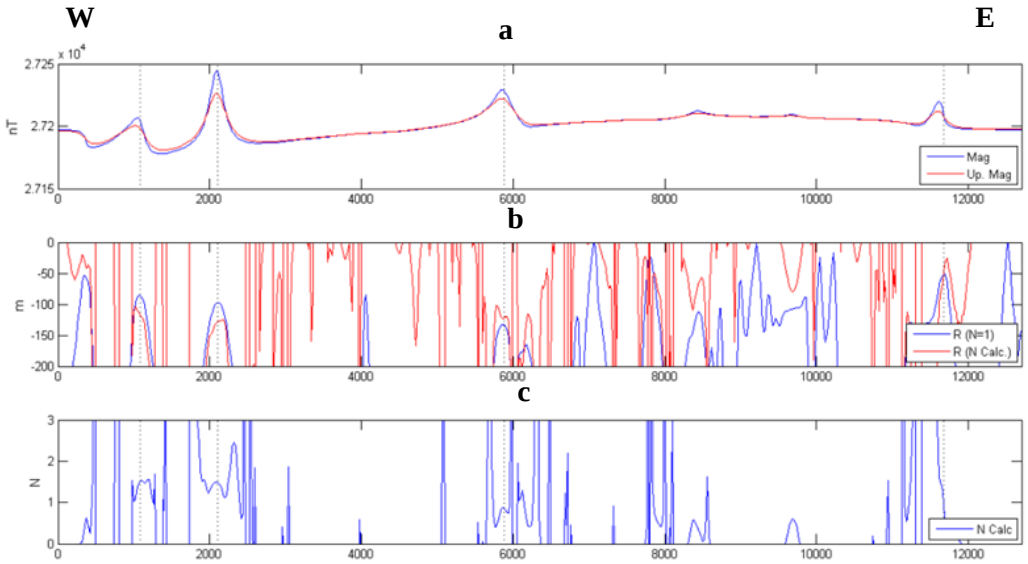


Figure 9.10 Profile 1 extracted from the secondary area. a) TMI (blue) and upward continued TMI (red). b) Distance to source using a structural index of 1 (blue) and the distance to source using the calculated structural index (red). c) calculated structural index.

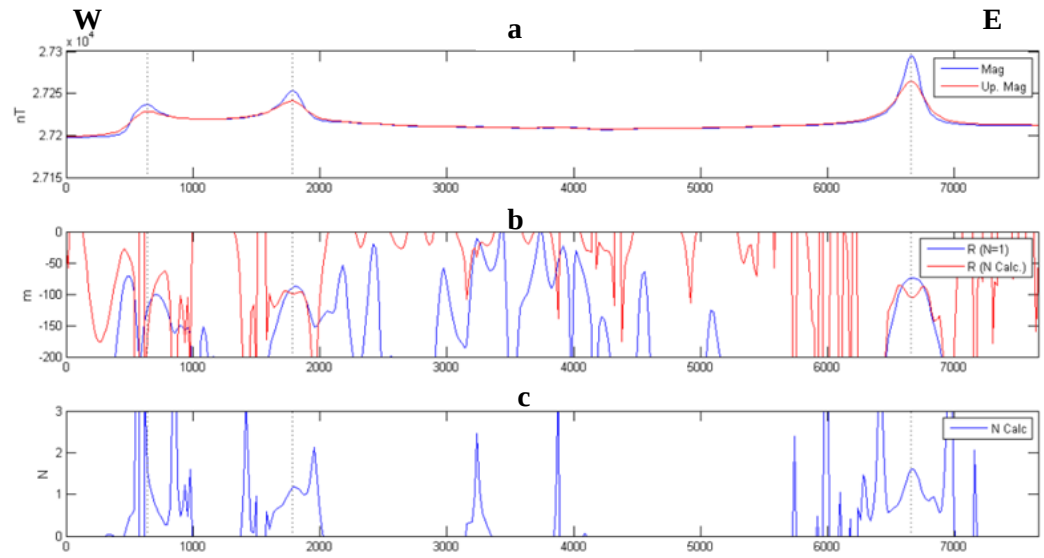


Figure 9.11 Profile 2 over the secondary area. a) TMI (blue), and upward continued TMI (red). b) Distance to source using a structural index of 1 (blue) and the distance to source using the calculated structural index (red). c) Calculated structural index

	N = 1	N = Calc.	% Error
Profile 1	85	116	36%
	98	129	31%
	133	122	8%
	51	47	8%
Profile 2	N/A	N/A	N/A
	88	98	11%
	74	106	43%

Table 9.1 Summary of depth to dykes determined by the distance to source method and the analytic signal fall-off method

Table 9.1 shows the depth to the dykes over the two profiles. Note neither method, when applied to the, second profile produced depth estimates for the first dyke i.e. there was no local minima over the location of the dyke. The third dyke along profile 1 outcrops (as can be seen in the elevation data) and has an apparent depth equal to the flight height. Assuming the depths for the constrained inversion (N=1) are correct the percentage error in the non-constrained inversion (structural index calculated by the analytic signal fall-off method) was calculated. If the incorrect structural index was used when calculating the distance to source (Cooper, 2014) then the percentage difference would be 50% hence with a maximum difference of 43% observed over the set of dykes the rescaled distance to source shows errors that are acceptable. Furthermore if the method is used to simply distinguish between contacts and dykes then further improvement of results will be observed.

The two profiles were then inverse modelled, with the depth of the dykes constrained by the distance to source method (Cooper, 2014). For both profiles (Figures 9.12 and 9.13) the measured TMI and modelled TMI were well matched assuming the dykes had a vertical dip and were all 2 m thick. Changing the thickness increases the wavelength of the dyke and so does not allow for the slopes of the signals to be mached. Referring to Figure 9.9 it is clear that the second dyke modelled on the first profile and the third dyke on the second profile are in reality the same dyke. Since the magnetic susceptibility of the aforementioned dyke is approximately equivalent and there is minimal misfit observed on both the profiles, confidence can be placed in the model i.e. the depth estimates.

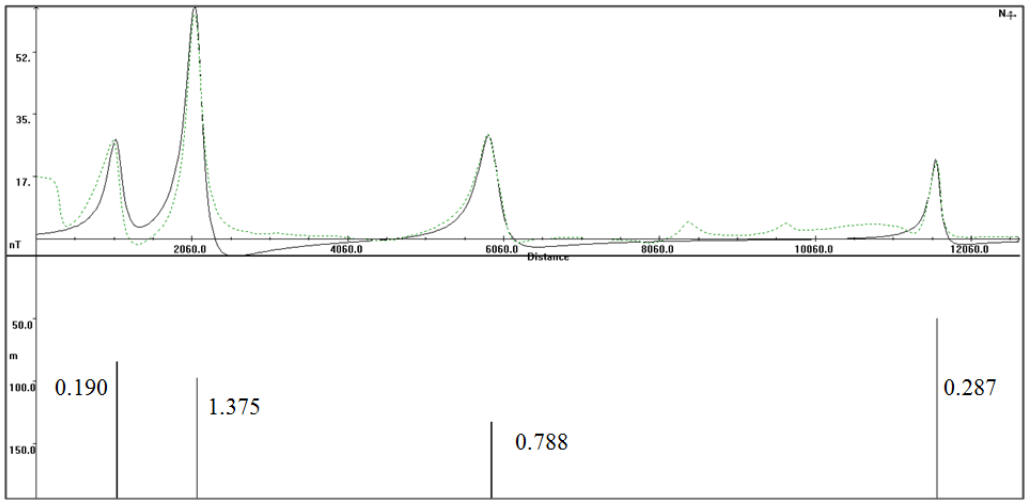


Figure 9.12 Inverse modelling of profile 1. The observed magnetic field is given by the dashed green line, while the modelled response is given in black. The depth of the dykes was set to the calculated values given by the distance to source method (Cooper, 2014) with a structural index of 1. The dykes all had a thickness of 2 m, with the susceptibility (S.I) of each of the dykes given alongside the appropriate dyke.

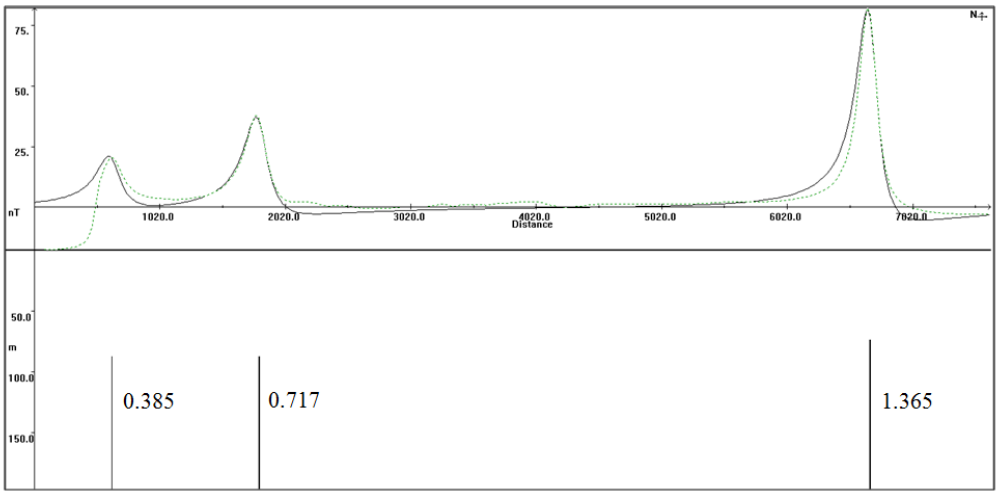


Figure 9.13 Inverse modelling of profile 2. The observed magnetic field is given by the dashed green line, while the modelled response is given in black. The depth of the dykes was set to the calculated values given by the distance to source method (Cooper, 2014) with a structural index of 1. The dykes all had a thickness of 2 m, with the susceptibility (S.I) of each of the dykes given alongside the appropriate dyke.

9.2.3 Secondary Area - Calculation of distance to source and rescaled distance to source on gridded data

As for the primary area, the distance to source method, as described by Cooper (2014) was applied to the data under the assumption of an *N*=1 source (Figure 9.14). The resultant distance image clearly illustrates the dykes mapped to the south of the sand cover (coloured in yellow on Figure 9.7) are connected to the dykes mapped in the north. Local minima over the dykes indicate their occurrence at a depth of around 80 m in the south becoming ≈110 m where present under recent sand cover while returning to depths around 70 m to the north. While the southern portion of the dyke swarm clearly outcrops, as testified to by the surface elevation image of the region (Figure 8.8) surface weathering may reduce the magnetic response of the dykes in the upper portions. I.e. the dykes are only truly magnetic bellow a depth of 30 m (80 m minus the flight height of 50 m). Furthermore if the top of the dykes are approximately level and the weathering profile, if present, is consistent then the sand cover can be assumed to be between 30 m and 40 m thick.

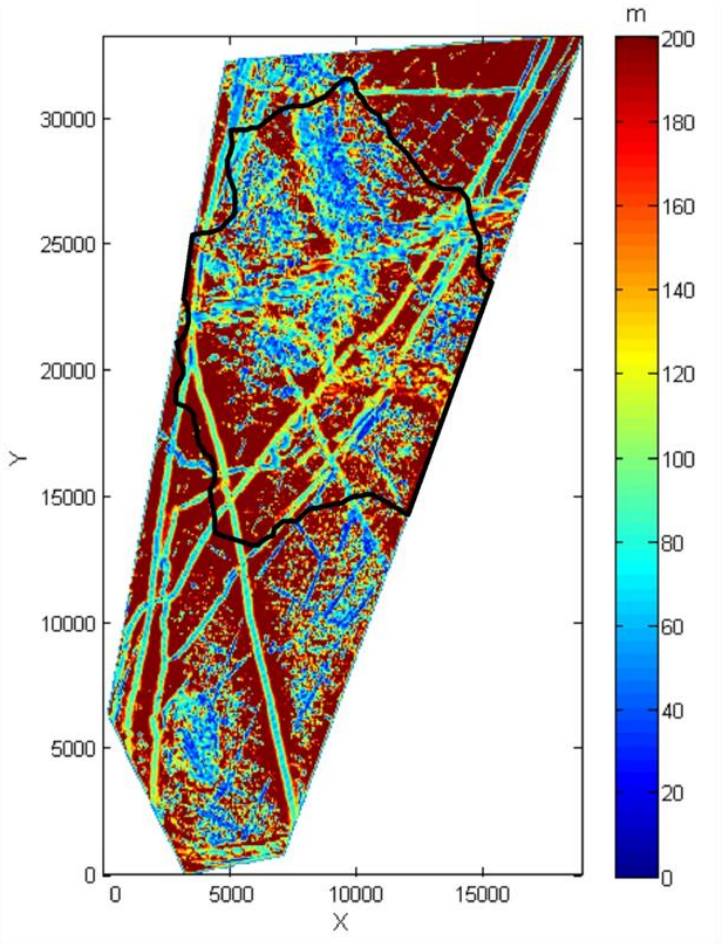


Figure 9.14 Distance to source over the secondary area calculated using a structural index of 1. The black outline indicates the boundary of the recent sand cover, estimated depths are deeper in this area.

The structural index over the secondary area was then calculated by making use of the analytic signal fall-off method (Chapter 6) (Figure 9.15). The data were upward continued by a height of 20 m prior to the application of the method to suppress high frequency noise content. A separation of 20 m was used between elevations. Structural index values greater than 3 or less than 0 were defined as invalid solutions and are shaded in grey (Figure 9.15). Structural index values close to 1 are calculated over the mapped dykes, as expected.

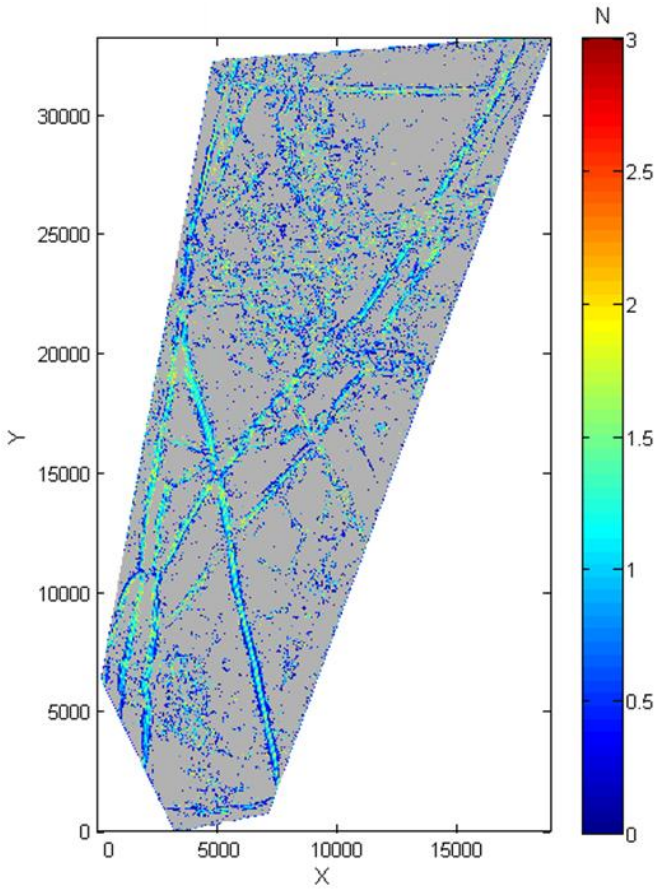


Figure 9.15 Estimated structural index values over the secondary area. Values calculated by making use of the analytic signal fall-off method. Calculated structural index values outside of the range of 0 to 3 were rejected and shaded in grey.

Figure 9.16 shows the results of the rescaled distance to source method, i.e. the non-constrained distance inversion (Chapter 6). Whilst there is an increase in noise levels compared to the distance to source image based on assuming N= 1 (Figure 9.14) the overall depth trends are preserved. For example the apparent depth of the dykes under the

sand cover increases in a similar fashion to what was observed in the constrained inversion.

To evaluate the variation on depth estimates between the non-constrained and constrained inversion techniques the absolute difference between the two images was calculated (Figure 9.17). The results indicate that the depth of the dykes varies on average by less than 10 to 15 m between the two methods.

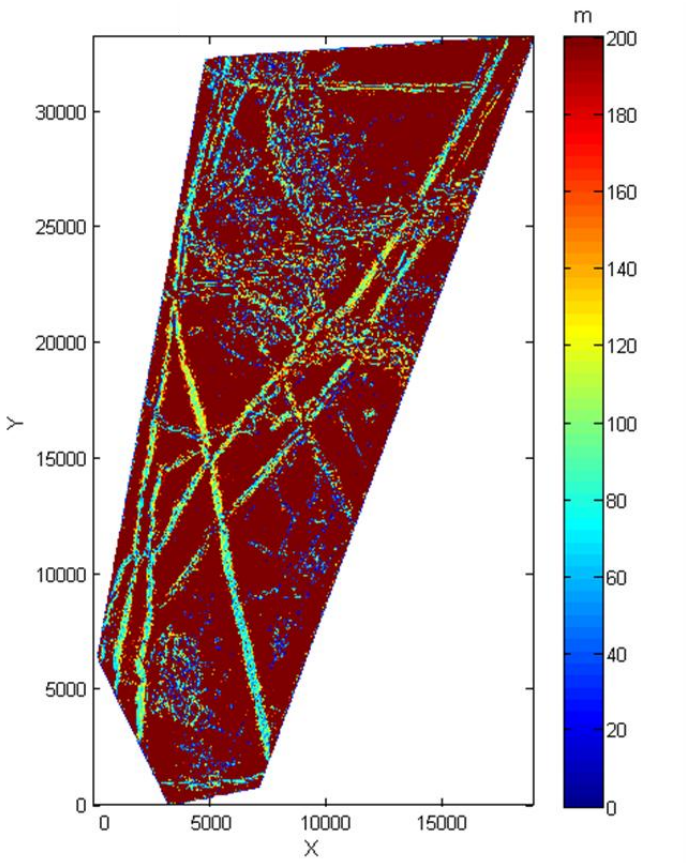


Figure 9.16 Rescaled distance to source over the secondary area. Although there is an increase in noise levels the overall distance to source trends are preserved.

The unconstrained method for determining the depth of magnetic sources (presented in Chapter 7) was aplied to the secondary region. The data were upward continued by a height of 60 m prior to the application of the method to suppress high frequancy noise content. A further 20 m of upward continuation was applied to the data to allow for the construction of the elevated second dataset, required for the method.

The depth solutions were then calculated and used to determine the structural index. Structural index values outside of the range of [0,3] (appropriate for magnetic data for contacts dykes and point sources) were assumed to represent locations far from magnetic bodies as thus the associated depth solutions were rejected. The filtered depth image is presented in Figure 9.18. The filtered depth solutions show not only simmilar depth trends to the distance to source using a fixed structural index value (Figure 9.14) but are significantly less noisy than the rescaled distance to source solutions (Figure 9.16) due to this filtering based on the structural index.

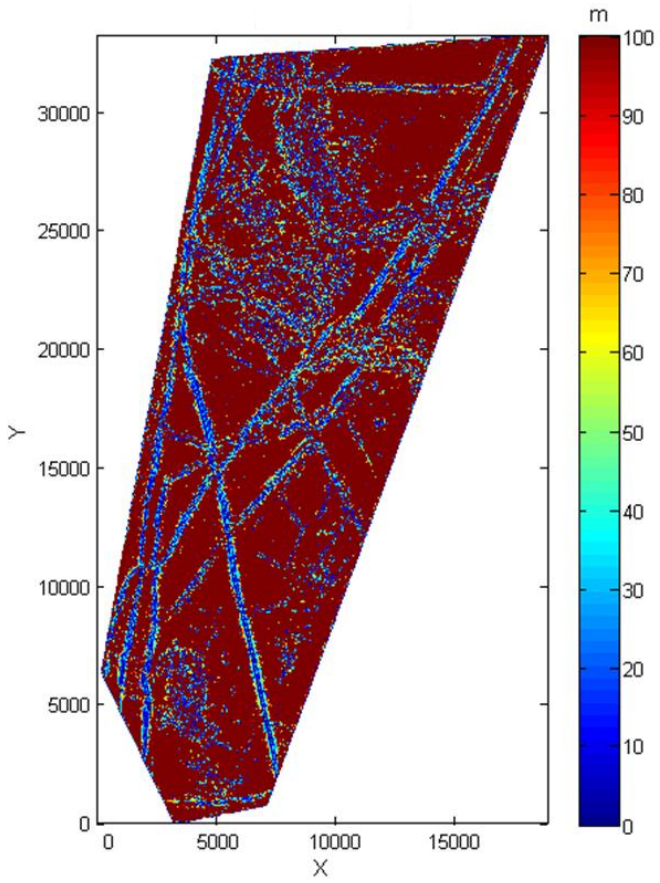


Figure 9.17 The absolute difference between the distance to source with a structural index of 1 and the rescaled distance to source (with the structural index calculated by the analytic signal fall-off method) over the secondary area. On average the absolute difference is less than 30 m between the two methods over the dykes.

For comparison, the structural index of the secondary area was also calculated by making use of the extended DEXP method. The data were upward continued to a height of 100 m in 1m intervals to construct the necessary data volume used for the structural index

estimate. The first and second order vertical derivatives of the field were used, under three assumed structural index values (namely 0, 1, 2) as previously presented. The results are presented in Figure 9.19. The structural index over the southern part of the dykes results in structural index estimations of 1. However under the sand cover the structural index values for the dykes were estimated to be equal to 0. This resulted in a rescaled distance to source image (Figure 9.20) that did not preserve the overall distance to source trends present in the constrained inversion (Figure 9.14).

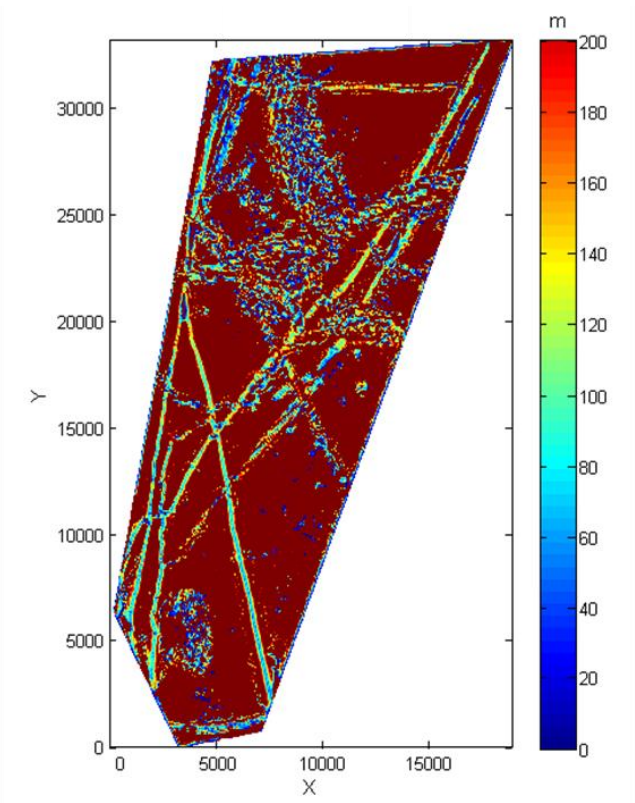


Figure 9.18 Filtered depth of magnetic sources contained within the secondary region. Filtering was based on rejecting depth solutions associated with structural index values outside of the range of [0, 3].

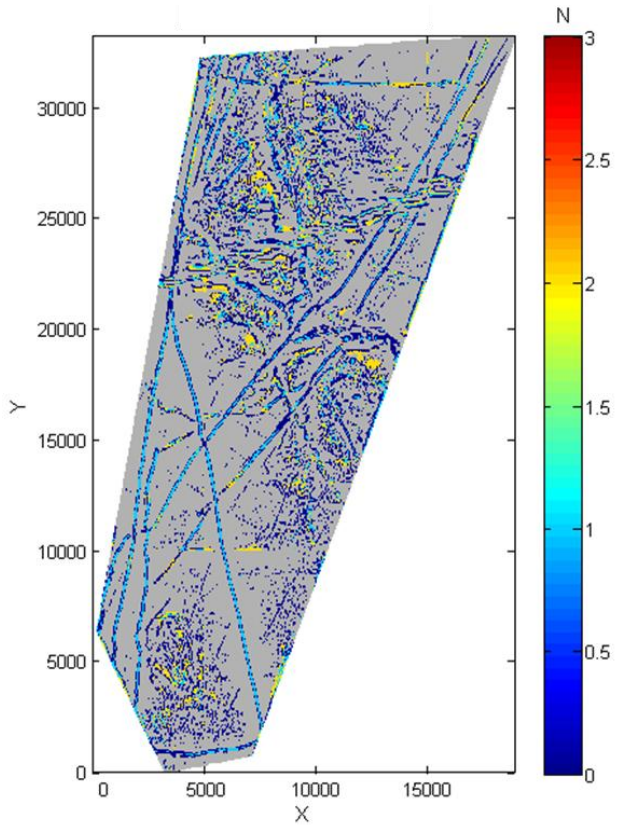


Figure 9.19 Structural index estimation over the secondary area after the application of the extended DEXP method. Values less than 0 or greater than 3 were rejected and shaded in grey.

The absolute difference, between the rescaled distance to source (calculated by making use of the structural index values given by the extended DEXP method) and the original image was calculated (Figure 9.21). While for the exposed portions of the dyke swarm, where an estimated structural index of 1 was calculated the distance to source estimations were naturally equal, variations between 60 to 80 m were however observed between the two images beneath the sand cover where the structural index had been poorly determined.

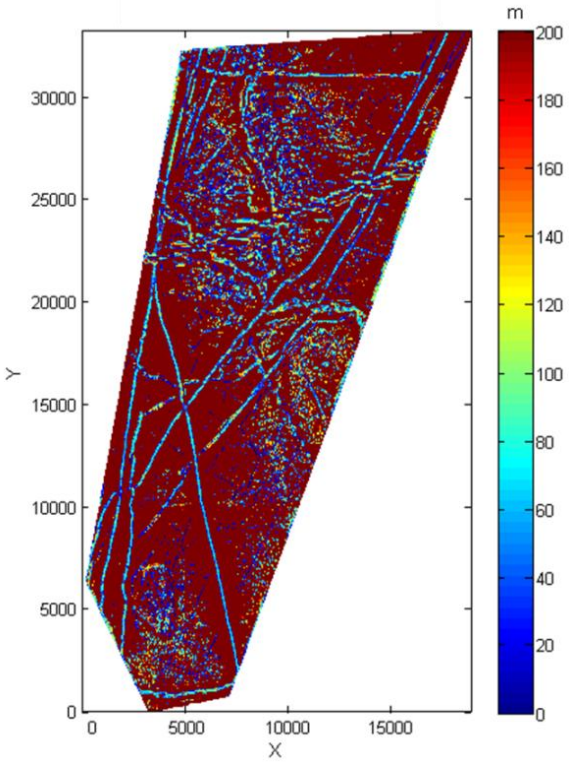


Figure 9.20 Rescaled distance to source over the secondary area using structural index values calculated by making use of the extended DEXP method.

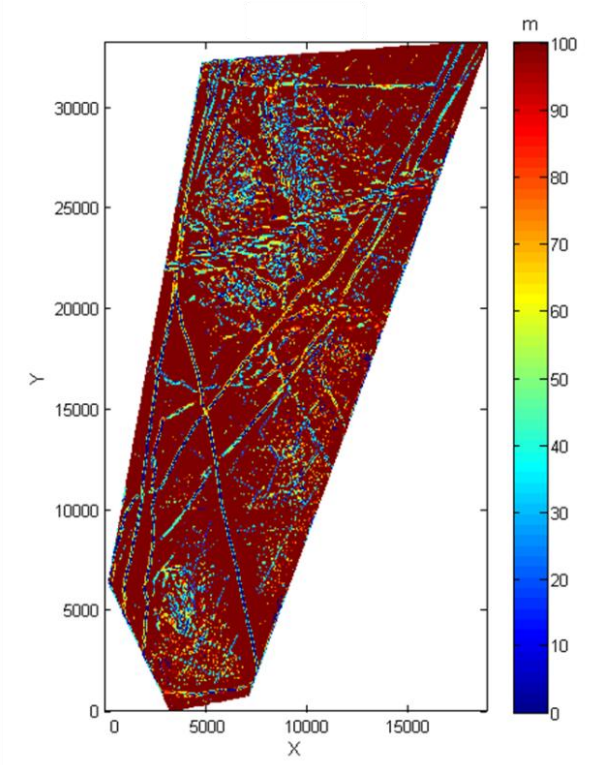


Figure 9.21 The absolute difference between the distance to source assuming a structural index of 1 and the rescaled distance to source (with the structural index calculated by the extended DEXP method) over the secondary area. Significant variation in the depth of the dykes is observed under the sand cover where the structural index is poorly estimated due to increased noise.

R_h (equation 9.3) was calculated over the secondary area with distances in excess of 30 m assumed to be sufficiently far from any source to represent the location of a magnetic body. The results presented in Figure 9.22 show values approaching 0 directly over the multiple dykes in the region. Furthermore, the presence of other coherent magnetic units that were not previously imaged on the TMI map of the region, due to saturation of the image, can now be observed (most notably around X=4 500 m, Y=5 000 m). Finally this filter could be used with any of the distance/ depth to source methods previously described to filter the generated solutions to obtain depths directly over the true location of the magnetic bodies present.

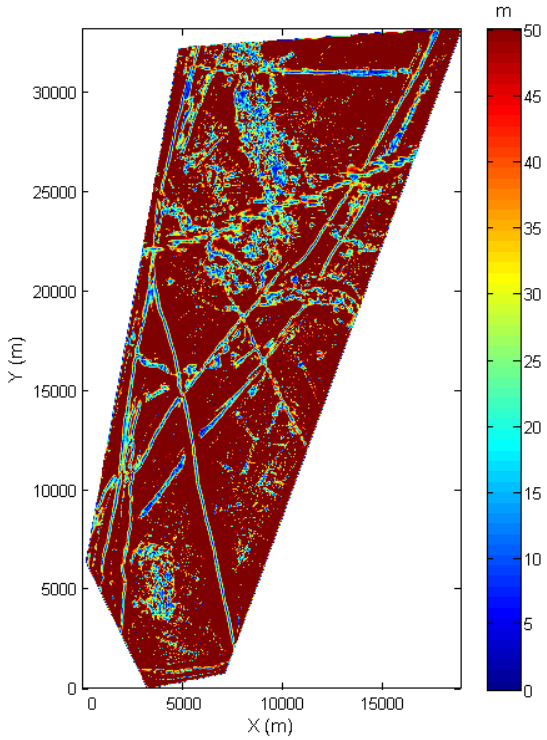


Figure 9.22 R_h calculated over the secondary region. R_h tends to 0 directly over the multiple dykes present in the region.

9.3 Three dimensional imaging of the magnetic subsurface under the secondary region

For illustration purposes the various results obtained from the depth inversion techniques were plotted on a three dimensional surface. To enhance the image a subset of the secondary region (Figure 9.23) was used, namely where the concentration of magnetic dykes was the highest. The three dimensional plots illustrate how the depth of the dykes varies along their strike furthermore it shows how the dykes intersect one another (e.g.

with level tops or not). All three methods used (Figure 9.24) highlight the presence of the sill located in the southernmost corner of the region which is not clearly imaged on the TMI map. The distance to source image (Figure 9.24a) produced assuming a structural index of 1 shows the sill as a single unit whilst both the rescaled distance to source and non-constrained depth inversion images (Figure 9.4b and c) show the sill as two distinct bodies both semi-circular in shape. Furthermore, there is an increase in noise levels between using the non-constrained depth inversion method as compared to the conventional distance to source (with N=1) there is also an increase in resolution, thereby clearly highlighting more of the subtle features associated with the dykes. Finally all depth solutions over the dykes appear to be consistent between methods.

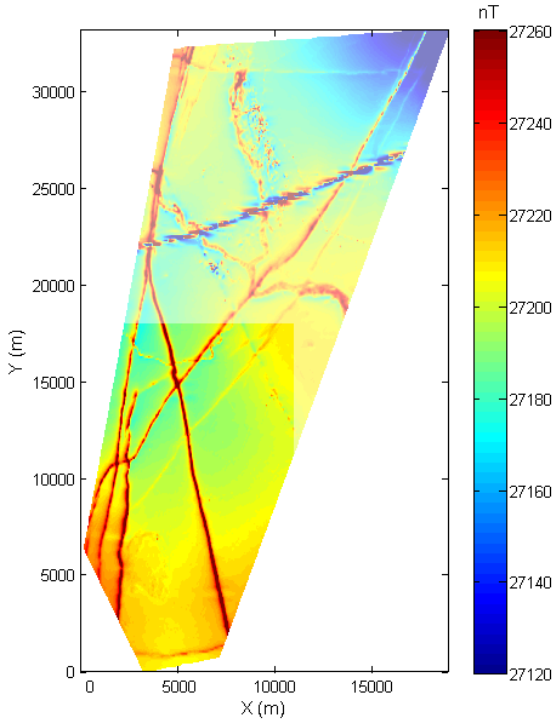


Figure 9.23 Location of subset of the secondary region used for calculating the 3D surface images of the magnetic subsurface.

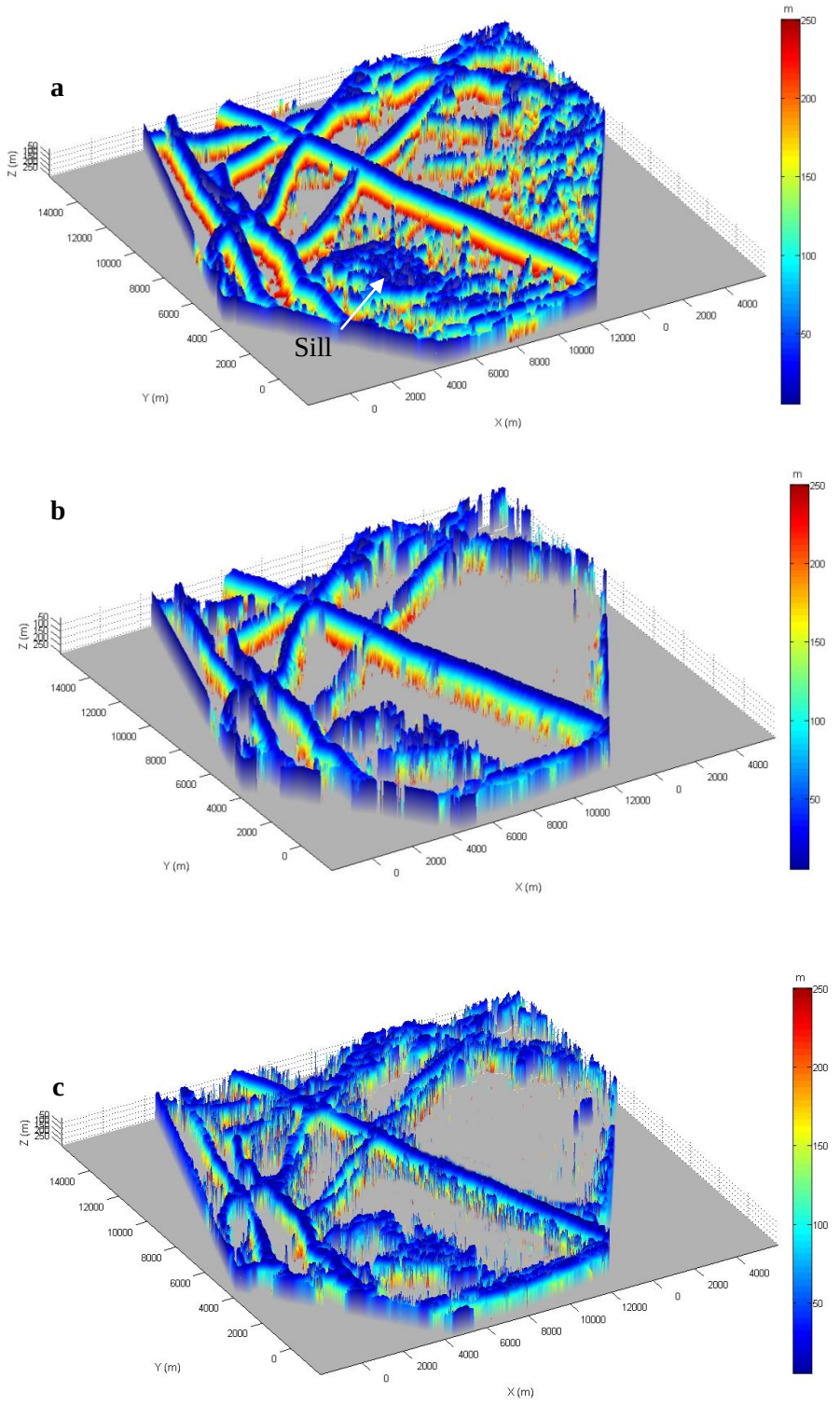


Figure 9.24 Three dimensional images of the magnetic subsurface under the southern portion of the secondary region. a) 3D plot showing the depth of the magnetic dykes calculated by making use of the distance to source method after Cooper, (2014) with *N*=1. b) Rescaled distance to source after scaling the distance to source by the structural index calculated by making use of the analytic signal fall-off method. c) Depth of magnetic bodies calculated by the non-constrained inversion method presented in Chapter 7.

Chapter 10: Ensuring Repetition of Results

10.1 Justification and presentation of second dataset

The scientific method relies on replication of results. In this case it should be ensured that the application of the proposed methods results in reasonable output when applied to real datasets. I.e. there applicability should not be unique to the dataset previously discussed, namely the Kuruman Military Area. To evaluate this applicability the discussed depth and structural index inversion methods were applied to aeromagnetic data collected over the Bushveld Complex, South Africa.

The data were collected on an east-west flight lines direction at a draped flight height of 50 m above the ground. The available data were gridded on a 15 m grid spacing. The TMI image of the region is presented in Figure 10.1. The region is dominated by a SW-NE dyke swarm with clear remnant magnetisation. This dataset was used by Cooper (2014) for describing the application of the distance to source method for real data.

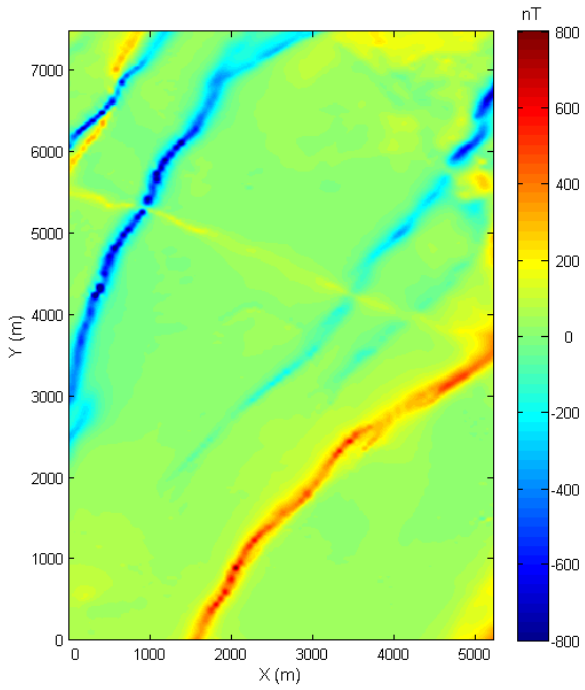


Figure 10.1 Total magnetic intensity image over part of the Bushveld Complex, South Africa.

10.2 Distance to source and structural index determination over secondary dataset

Since the region is dominated by magnetic dykes a structural index of 1 was used when calculating the distance to source after Cooper (2014). Prior to the calculation of the distance to source the data were upward continued by a height of 60 m to reduce the effect of high frequency noise. This upward continuation height was subtracted from the resultant distance to source estimations. The generated distance to source image (Figure 10.2) is equivalent to the distance to source image produce by Cooper, (2014).

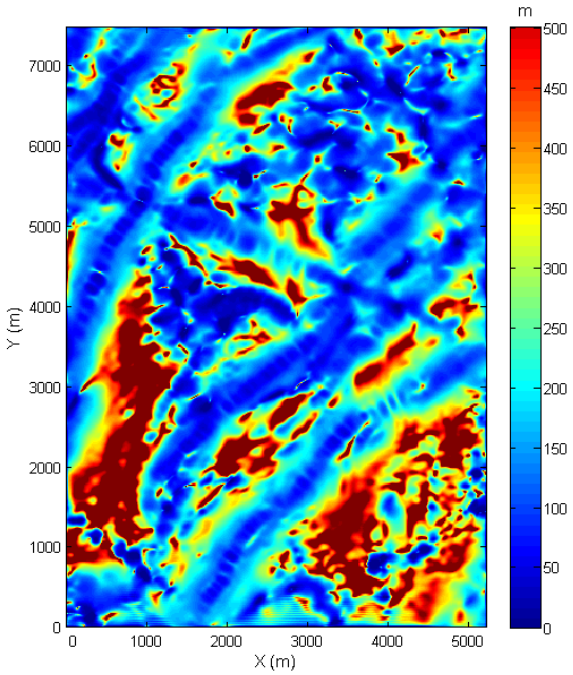


Figure 10.2 Distance to source calculated using a structural index of 1 over part of the Bushveld Complex, South Africa. The resultant image is equivalent to that found in Cooper, (2014).

As expected the distance to source image reaches local minima directly over the dykes, indicating the depth of the dykes to be between 60 and 100 m below the sensor height, i.e. 10 to 50 m below surface (assuming a constant flight height of 50 m).

The structural index image of the region was then produced by making use of the analytic signal fall-off method (presented in Chapter 6). The data were upward continued by a height of 60 m to calculate the variation in the analytic signal with distance to source. The resultant structural index map (Figure 10.3) shows values approaching 1 over the contacts. Structural index values outside of the range of [0, 3] were rejected as invalid

solutions and shaded in grey on the image. The beaded high-low pattern observed along the strike of the dykes indicates aliasing of the data due to a coarse sampling interval and that the dykes do not strike perpendicular to the flight lines.

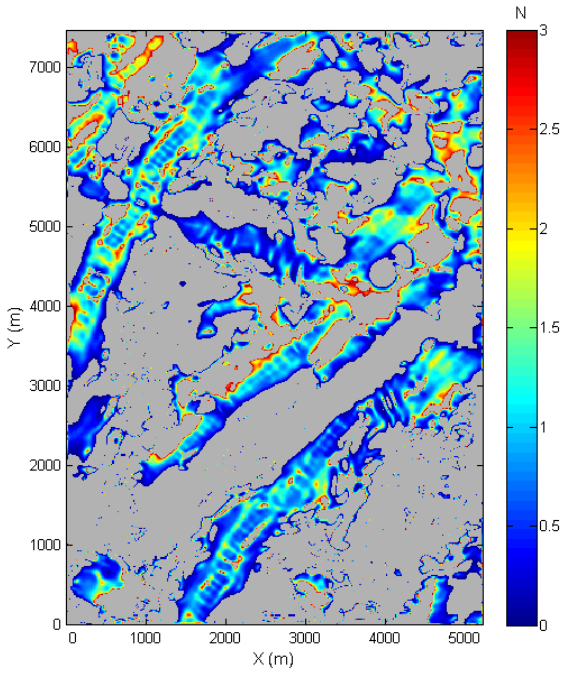


Figure 10.3 Structural index image produced by making use of the analytic signal fall-off method (Chapter 6) dykes in the Bushveld Complex, South Africa. Structural index values outside of the range of [0, 3] were considered to be invalid and rejected (shaded in grey on the image).

The rescaled distance to source (presented in figure 10.4) was then calculated by scaling the distance to source by the structural index values calculated by making use of the analytic signal fall-off method.

In areas away from the magnetic dykes the distance to source calculated by assuming a structural index of 1 (Figure 10.2) and the the rescaled distance to source (Figure 10.4) vary significantly as expected. However; directly over the magnetic dykes the difference between the two images is minimal, indicating that the structural index was well estimated.

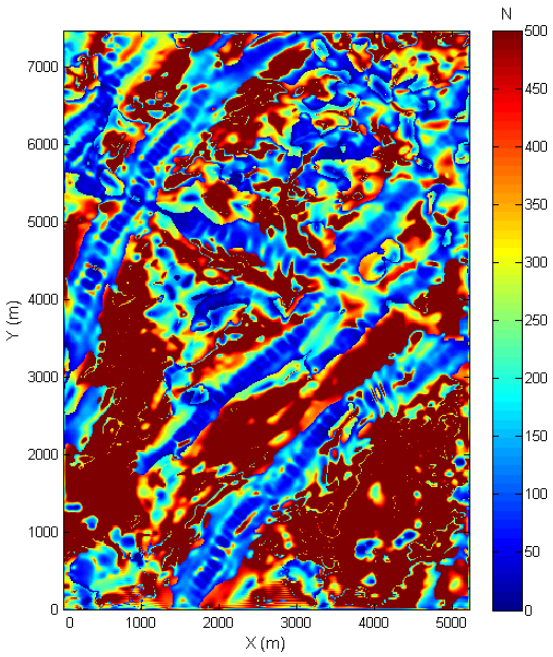


Figure 10.4 Rescaled distance to source after scaling the distance to source by the structural index values calculated by making use of the analytic signal fall-off method over dykes in the Bushveld Complex, South Africa.

The depth of the magnetic dykes was found by making use of the non-constrained inversion procedure presented in Chapter 7. The depth solutions (Figure 10.5) were filtered based on rejecting depth solutions associated with structural index values outside of the range of [0, 3]. Rejecting depth solutions in this manner ensured that only the magnetic dykes were imaged. Furthermore the method gave similar depths (between 10 m and 50 m below surface) to the distance to source method (Figure 10.2).

Finally, R_h values were calculated over the region to highlight the edges of the magnetic units. The R_h image (Figure 10.6) clearly delineates the magnetic dykes in the region as expected.

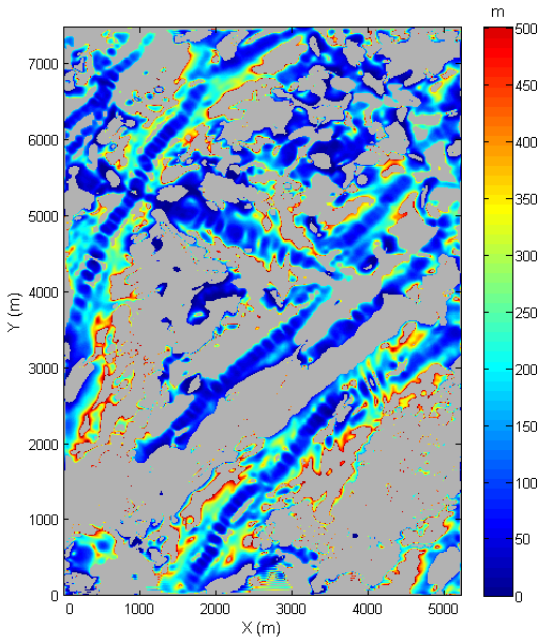


Figure 10.5 Depth to source calculated by making use of the non-constrained inversion method (Chapter 7) over dykes in the Bushveld Complex, South Africa.

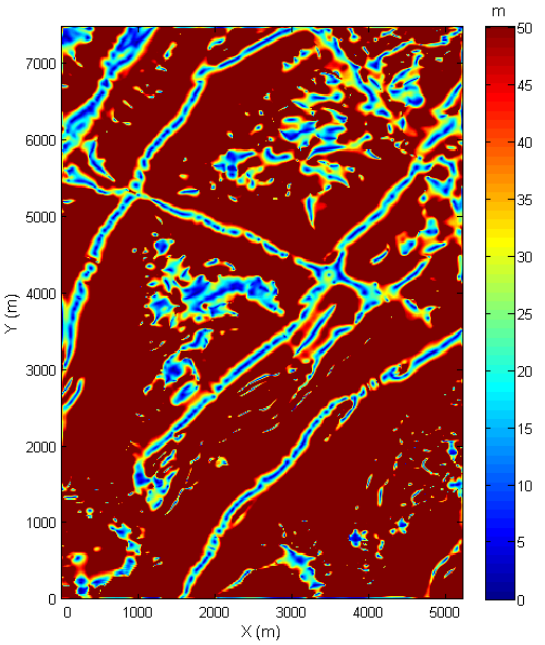


Figure 10.6 R_h values calculated over dykes in the Bushveld Complex, South Africa clearly delineating the magnetic dykes in the area.

10.3 Three dimensional subsurface images showing the magnetic depths of the secondary dataset

For completeness the calculated distance and depth inversions calculated over the Bushveld Complex dataset were also imaged in a 3D format (Similar to Section 9.3) to display the change in depth and intersecting nature of the dykes. The distance to source (with N=1) and the rescaled distance to source after calculating the structural index via the analytic signal fall-off method show good resemblance to one another. The non-constrained depth inversion shows higher noise levels but is also associated with increased resolution. Again all depths are similar indicating good correlation and consistency between the methods.

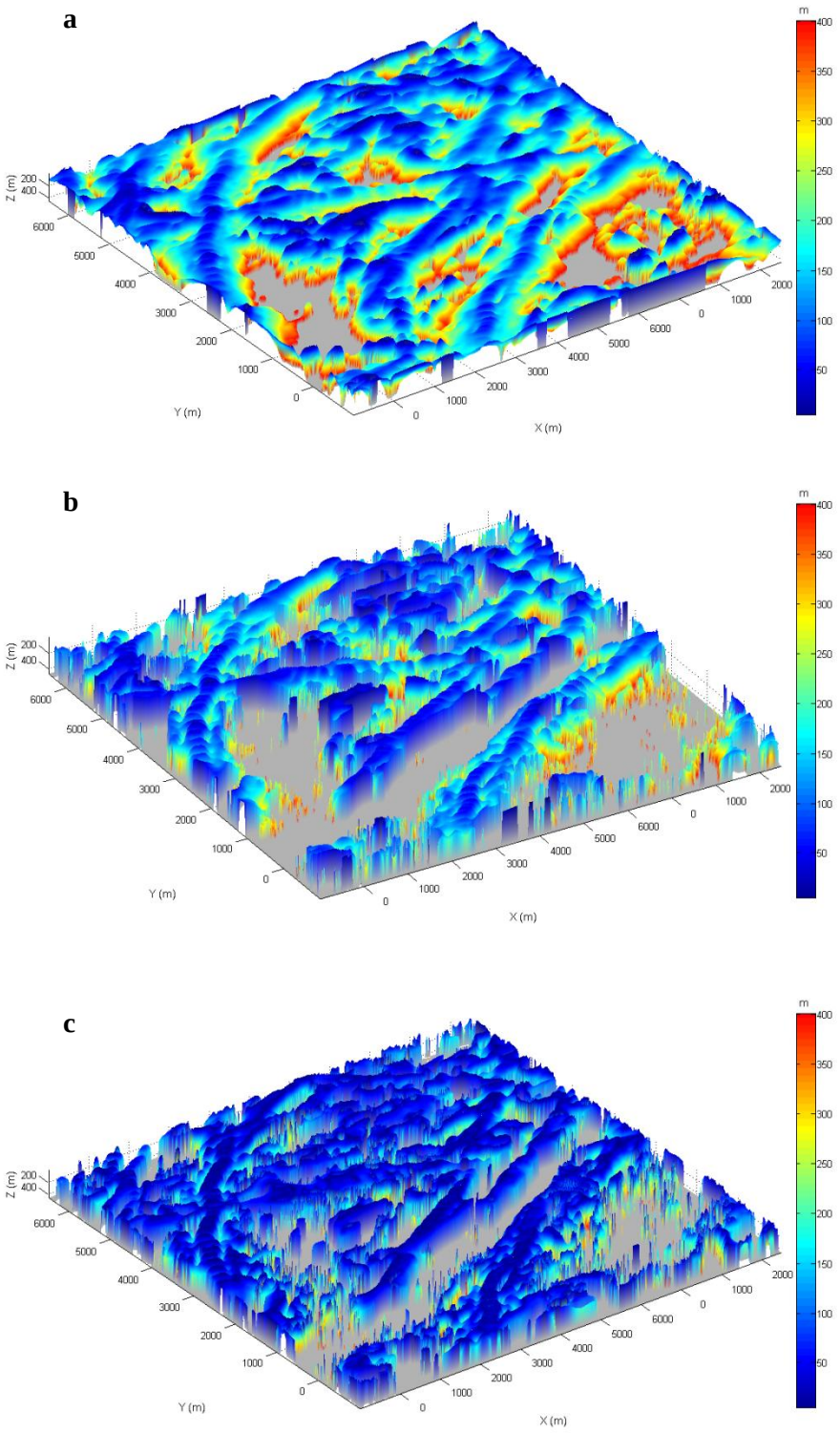


Figure 10.7 Three dimensional images of the magnetic subsurface under part of the Bushveld Complex, South Africa. a) 3D plot showing the depth of the magnetic dykes calculated by making use of the distance to source method after Cooper, (2014) with *N*=1. b) Rescaled distance to source after scaling the distance to source by the structural index calculated by making use of the analytic signal fall-off method. c) Depth of magnetic bodies calculated by the non-constrained inversion method presented in Chapter 7.

Chapter 11: Conclusions

Transforming magnetic data into source location estimates has clear applicability since the general purpose of a magnetic survey is to gain a better understanding of the subsurface geology. Estimating the horizontal position of the magnetic source is a relatively easy task. For example, to a good estimation, the source will be located directly under the maxima of the analytic signal or can be estimated by tracing the correct contours of the tilt angle (under certain assumptions). In this dissertation a new method was proposed that can be used to estimate the horizontal location of the source based on simultaneously solving for the horizontal components from the distance to source observed from two different elevations above the source. One of the key advantages of this method is that the solutions take shorter to calculate than conventional methods.

Obtaining the depth of the source is however a much more complex task. Two methods that make use of first order derivatives of the measured magnetic field were reviewed. The first of these methods was the commonly used Euler deconvolution method. Solution sprays are generated in the solution space, with the closest grouping representing the most reliable estimation of the correct location of the magnetic source. Changing the window size used in the least squares inversion resulted in different solution sprays and hence optimal window size (large enough to sample a sufficient amount of gradient change over the feature of interest yet short enough to not sample interference) needs to be considered to ensure that different sized anomalies are sampled correctly. If the structural index of the source or sources is not known then the method is run multiple times with different structural index estimations. The closest grouping of solutions from the multiple iterations then not only give the best estimate of the source location but also of the structural index of the source. The need for the interpreter to assess the solution space in this manner makes the implementation of this method cumbersome. An advantage of Euler deconvolution is that it does not require the data to be transformed in any manner prior to its application and can be used on different source types and dipping bodies. The second, first order derivative based method presented was the Tilt-Depth method. Implementation of this method requires the data to be pole reduced as well as caused by vertical magnetic bodies (both dykes and contacts were presented). The resultant depth estimations are made by measuring the distance between generated contours of the tilt angle. For profile data this is a relatively simple task but may result in additional solutions between interfering bodies. For gridded data, measuring the distance between contours is complex, especially if there are multiple interfering bodies. The need for the

data to be pole reduced, due to vertical bodies and the need to further analyse the solutions obtained make the method unattractive to wide scale application. Both methods however have an advantage in that they do not severely enhance noise in the data since they are based on only the first order derivatives of the magnetic field.

Two methods that make use of the first and second order analytic signal amplitudes of the data are Ma and Du (2012), only applicable to profile data, and the approach proposed by Cooper (2014) which is able to be applied to both profile and gridded data. Making use of the ratio of the analytic signal amplitude to the second order analytic signal amplitude eliminates all terms describing the inducing magnetic field as well as the orientation of the body. The remaining terms only describe the location of the body and the type of body (the structural index). Since, for profile data, the source is located directly below the maxima of the analytic signal amplitude Ma and Du (2012) describe how the depth and structural index of the source can be calculated from points of observation away from this maxima. Cooper (2014) requires that the structural index be known to obtain a distance to source dataset.

The DEXP method requires the calculation of a scaled volume above the observation datum, where maxima within the volume and the source location are symmetrical about the x-y plane. This scaled volume can be constructed under the assumption of different causative source types and from different input datasets by making use of the appropriate scaling function. In the practice this results in 6 scaled volumes, 3 from each of the two different input datasets correlating to the 3 structural index values (N=0,1,2). The minimum difference between the scaled volumes calculated from the two different input datasets was then used to estimate the correct choice of structural index. This method was termed the extended DEXP method. Through the symmetry between the scaled volume and the location solutions it is clear that the maximum height of the scaled volume limits the maximum of the depth solutions obtained. A volume as high as the deepest expected source therefore needs to be constructed to ensure that the maxima due to the source is contained within the scaled volume. Furthermore a minimum of 6 such volumes need to be constructed. Hence the dataset volume can easily be expanded to be many times as big as the original dataset which itself can be sizable. Due to this, application of the DEXP method is cumbersome and prolonged.

All of these methods required that the data be known at a minimum of two different elevations. If the data was only acquired at the one elevation, as is generally the case then a second upward continued dataset can be constructed. The first of the methods solved for

each of the three principle directions independently to within a structural index proportionality factor. Hence if data are known at two points of observation then the structural index can be solved for simultaneously together with the corresponding principle direction. The second method was based on noting that the analytic signal amplitude falls off according to the structural index of the source and the distance to the source. Hence; calculating the ratio of the logarithms of the distance to the source (given by Cooper (2014)) and the ratio of the analytic signal amplitudes at the two different observation heights results in an estimate of the structural index. Through taking the ratio of the distance to source, the need for the correct choice of structural index required in the calculation is eliminated. The final structural index values were then used to generate what was termed a rescaled distance to source estimation. The results were also used to provide better Euler deconvolution solutions. The third and final method assumed that all points of observation at both data elevations were directly over the body. Under this assumption the depth of the body could be calculated independently of the structural index. Furthermore since by definition of the distance to source (Cooper, 2014) the structural index acts a proportionality constant it can be determined correctly over the true location of the body. The structural index is therefore used to reject depth solutions that do not occur in reality over the body which results in an unconstrained depth map of the area of interest.

The distance to source method (Cooper, 2014) and the rescaled distance to source estimation were applied to aeromagnetic data acquired over the Kuruman Military Area, South Arica. For comparison the extended DEXP method was also applied. For the primary area the distance to source estimation yielded results that correlated well to the known regional geology of the area. However both the DEXP and the analytic signal fall-off method yielded structural index estimations that did not represent the known geology. The reason for this is unclear, but may be due in part to the wide gridding interval used (125 m) since better results are produced in the secondary region where the data is represented at a 20 m interval i.e. aliasing. Application of the methods to the secondary region resulted in improved estimations of the structural index from both the analytic signal fall-off and DXP methods. To ensure that the structural index and depth inversion methods could be applied to other datasets they were also tested on aeromagnetic data collected over part of the Bushveld Complex, South Africa, which yielded stable and accurate results, verifying the wide scale applicability of the techniques.

Method	Profile / Grid Data	User Input	Resultant	Comments
Euler Deconvolution	Profile and grid	Yes – Window size and often structural index	Clusters of solutions	Traditionally used, requires significant user input
Tilt-Depth	Profile and grid data	No	Intercepts / contour map	Requires the distance between contours to be calculated
Depth from known points	Profile only	No	Plot of depth against distance	Requires user input and only applicable to profile data
Source-Depth	Profile and grid	Yes – Structural index	Local minima over the source at the depth of the source	Easy identification of source depth if correct structural index is used
DEXP	Profile and grid	No – Although increased processing time	Scaled data volume	Prolonged calculation and interpretation times
Multi-Directional Distance	Profile and grid	No	Plot or image with pseudo-horizontal distance to source.	Good as an edge detector. If N is known can find horizontal distance to source
Analytic Signal Fall-off	Profile and grid	No	Local minima over the source at the depth of the source	Susceptible to noise – no user input
Unconstrained Depth Inversion	Profile and grid	No	Local minima over the source at the depth of the source	Susceptible to noise – no user input. Depth solutions need to be filtered based on N

Table 11.1 Comparison of the different techniques discussed in this project

For theoretical data all of the newly proposed methods for determining the structural index over a source yielded good results. Application to real data however showed more variability, however did not perform any worse than the extended DEXP method. For real data that had low noise levels (the secondary area compared to the primary area) the results were significantly improved. The ease at which all methods can be applied, their wide scale applicability and lack of user control needed justifies implementing them in future inversion projects.

Further work needs to be focused on reducing noise levels in the calculations of the higher order derivative based methods, especially when such methods are applied to real data. For example it is well known that the analytic signal amplitude can be calculated using lower order or even partial derivatives of the field, thereby not requiring the calculation of second order derivatives to calculate the source - distance. Once a way of defining the location of a source, without known structural index, is found, be it from this dissertation or another work, the last parameter that needs to be inverted for is the dip of the body to provide a complete description. It should be noted however that the dip will not be separable from any remnant magnetisation vector that the source may have although may be of interest to the interpreter.

APPENDIX A

Mathematical background to the second order analytic signal amplitude depth / distance determination methods

Method 1: After Ma and Du (2012)

Calculating the ratio of the second to first order analytic signal amplitude.

Given

$$As = \frac{k}{(x^2 + z^2)^{(N+1)/2}}$$

Taking the x derivative,

$$\frac{\partial As}{\partial x} = \frac{\partial}{\partial x}\left(\frac{k}{(x^2 + z^2)^{(N+1)/2}}\right)$$

$$\frac{\partial As}{\partial x} = -k\frac{\partial}{\partial x}\left(\frac{1}{(x^2 + z^2)^{(N+1)/2}}\right)$$

Applying the quotient rule,

$$\frac{\partial As}{\partial x} = k\frac{(N+1)/2(x^2 + z^2)^{\frac{N+1}{2}-1}\frac{\partial}{\partial x}(x^2 + z^2)}{(x^2 + z^2)^{(N+1)}}$$

Simplifying,

$$\frac{\partial As}{\partial x} = k\frac{(N+1)(x^2 + z^2)^{\frac{N+1}{2}-1-(N+1)}2x}{2}$$

$$\frac{\partial As}{\partial x} = k(N+1)(x^2 + z^2)^{\frac{N+1-2-2N-2}{2}}x$$

$$\frac{\partial As}{\partial x} = k(N+1)(x^2 + z^2)^{-\frac{N+3}{2}}x$$

Therefore the x derivative of the analytic signal amplitude defined by Ma and Du (2012) is,

$$\frac{\partial As}{\partial x} = k\frac{(N+1)(x)}{(x^2+z^2)^{\frac{N+3}{2}}}$$

Similarly,

$$\frac{\partial As}{\partial z} = k\frac{(N+1)(z)}{(x^2+z^2)^{\frac{N+3}{2}}}$$

The second order analytic signal amplitude is therefore give by,

$$As_2 = \sqrt{\left(\frac{\partial As}{\partial x}\right)^2 + \left(\frac{\partial As}{\partial z}\right)^2}$$

$$As_2 = \sqrt{\frac{k^2(N+1)^2x^2}{(x^2+z^2)^{N+3}} + \frac{k^2(N+1)^2z^2}{(x^2+z^2)^{N+3}}}$$

Again simplifying yields,

$$As_2 = \sqrt{\frac{(x^2+z^2)(N+1)^2k^2}{(x^2+z^2)^{N+3}}}$$

$$As_2 = \sqrt{\frac{(N+1)^2k^2}{(x^2+z^2)^{N+2}}}$$

Finally,

$$As_2 = k\frac{(N+1)}{(x^2+z^2)^{(N+2)/2}}$$

Therefore calculating the ratio of the second to first order analytic signal amplitude,

$$\frac{As_2}{As} = \frac{\frac{k(N+1)}{(x^2+z^2)^{(N+2)/2}}}{\frac{k}{(x^2+z^2)^{(N+1)/2}}}$$

This simplifies to,

$$\frac{As_2}{As} = \frac{(N+1)}{(x^2+z^2)^{\frac{1}{2}}}$$

Deriving the expressions for the depth and structural index used by Ma and Du (2012)

The ratio of the second to first order analytic signal amplitude at x = 0 is given by,

$$\left.\frac{As_2}{As}\right|_{x=0} = \frac{(N+1)}{(z^2)^{\frac{1}{2}}}$$

Dividing this by the ratio where x~=0 yields,

$$\frac{\left.\frac{As_2}{As}\right|_{x=0}}{\frac{As_2}{As}} = \frac{\frac{(N+1)}{(z^2)^{\frac{1}{2}}}}{\frac{(N+1)}{(x^2+z^2)^{\frac{1}{2}}}}$$

Simplifying,

$$\frac{\left.\frac{As_2}{As}\right|_{x=0}}{\frac{As_2}{As}} = \frac{(x^2+z^2)^{\frac{1}{2}}}{(z^2)^{\frac{1}{2}}}$$

Solving for z,

$$z^2\left(\frac{\left.\frac{As_2}{As}\right|_{x=0}}{\frac{As_2}{As}}\right)^2 = (x^2+z^2)$$

$$z^2\left(\left(\frac{\left.\frac{As_2}{As}\right|_{x=0}}{\frac{As_2}{As}}\right)^2 - 1\right) = x^2$$

Yields,

$$z = \sqrt{\frac{x^2}{\left(\frac{\left.\frac{As_2}{As}\right|_{x=0}}{\frac{As_2}{As}}\right)^2 - 1}}$$

Calculating the difference of the square of the reciprocal of the ratio when x = 0 and where x~= 0 allows for the structural index to be solved for.

The reciprocal of the square when x=0 can be expressed as,

$$\left(\frac{As_2}{As}\Big|_{x=0}\right)^{-2} = \left(\frac{(N+1)}{(z^2)^{\frac{1}{2}}}\right)^{-2}$$

$$\left(\frac{As}{As_2}\Big|_{x=0}\right)^{2} = \left(\frac{(z^2)^{\frac{1}{2}}}{(N+1)}\right)^{2}$$

The reciprocal of the square when x~=0 can be expressed as,

$$\left(\frac{As_2}{As}\right)^{-2} = \left(\frac{(N+1)}{(x^2+z^2)^{\frac{1}{2}}}\right)^{-2}$$

$$\left(\frac{As}{As_2}\right)^{2} = \left(\frac{(x^2+z^2)^{\frac{1}{2}}}{(N+1)}\right)^{2}$$

Taking the difference yields,

$$\left(\frac{As}{As_2}\Big|_{x=0}\right)^{2} - \left(\frac{As}{As_2}\right)^{2} = \left(\frac{(z^2)^{\frac{1}{2}}}{(N+1)}\right)^{2} - \left(\frac{(x^2+z^2)^{\frac{1}{2}}}{(N+1)}\right)^{2}$$

$$\left(\frac{As}{As_2}\Big|_{x=0}\right)^{2} - \left(\frac{As}{As_2}\right)^{2} = \left(\frac{z^2 - x^2 - z^2}{(N+1)^2}\right)$$

Solving for N yields,

$$(N+1)^2 = \frac{-x^2}{\left(\frac{As}{As_2}\Big|_{x=0}\right)^{2} - \left(\frac{As}{As_2}\right)^{2}}$$

$$N = \sqrt{\frac{x^2}{\left(\frac{As}{As_2}\right)^{2} - \left(\frac{As}{As_2}\Big|_{x=0}\right)^{2}}} - 1$$

Therefore in this manner both N and z can be solved for independently of one another. This can however only be applied to profile data.

Method 2: After Cooper (2014)

Calculating the second order analytic signal amplitude

Given,

$$As = \sqrt{\left(\frac{\partial f}{\partial x}\right)^2 + \left(\frac{\partial f}{\partial y}\right)^2 + \left(\frac{\partial f}{\partial z}\right)^2}$$

Taking the x derivative,

$$\frac{\partial As}{\partial x} = \frac{\partial}{\partial x}\left(\left(\frac{\partial f}{\partial x}\right)^2 + \left(\frac{\partial f}{\partial y}\right)^2 + \left(\frac{\partial f}{\partial z}\right)^2\right)^{\frac{1}{2}}$$

Applying the chain rule,

$$\frac{\partial As}{\partial x} = \frac{1}{2}\left(\left(\frac{\partial f}{\partial x}\right)^2 + \left(\frac{\partial f}{\partial y}\right)^2 + \left(\frac{\partial f}{\partial z}\right)^2\right)^{-\frac{1}{2}} \times \frac{\partial}{\partial x}\left(\frac{\partial f}{\partial x}\right)^2 + \frac{\partial}{\partial x}\left(\frac{\partial f}{\partial y}\right)^2 + \frac{\partial}{\partial x}\left(\frac{\partial f}{\partial z}\right)^2$$

$$\frac{\partial As}{\partial x} = \frac{\frac{1}{2}\left(2\frac{\partial f}{\partial x}\frac{\partial f \partial f}{\partial x \partial x} + 2\frac{\partial f}{\partial y}\frac{\partial f \partial f}{\partial x \partial y} + 2\frac{\partial f}{\partial z}\frac{\partial f \partial f}{\partial x \partial z}\right)}{\sqrt{\left(\frac{\partial f}{\partial x}\right)^2 + \left(\frac{\partial f}{\partial y}\right)^2 + \left(\frac{\partial f}{\partial z}\right)^2}}$$

(This is equivalent to the expression given by Florio et al. (2006))

Simplifying,

$$\frac{\partial As}{\partial x} = \frac{\frac{\partial f}{\partial x}\frac{\partial^2 f}{\partial x^2} + \frac{\partial f}{\partial y}\frac{\partial^2 f}{\partial x \partial y} + \frac{\partial f}{\partial z}\frac{\partial^2 f}{\partial x \partial z}}{\sqrt{\left(\frac{\partial f}{\partial x}\right)^2 + \left(\frac{\partial f}{\partial y}\right)^2 + \left(\frac{\partial f}{\partial z}\right)^2}}$$

Similarly,

$$\frac{\partial As}{\partial y} = \frac{\frac{\partial f}{\partial x}\frac{\partial^2 f}{\partial x \partial y} + \frac{\partial f}{\partial y}\frac{\partial^2 f}{\partial y^2} + \frac{\partial f}{\partial z}\frac{\partial^2 f}{\partial y \partial z}}{\sqrt{\left(\frac{\partial f}{\partial x}\right)^2 + \left(\frac{\partial f}{\partial y}\right)^2 + \left(\frac{\partial f}{\partial z}\right)^2}}$$

$$\frac{\partial As}{\partial z} = \frac{\frac{\partial f}{\partial x}\frac{\partial^2 f}{\partial x \partial z} + \frac{\partial f}{\partial y}\frac{\partial^2 f}{\partial y \partial z} + \frac{\partial f}{\partial z}\frac{\partial^2 f}{\partial z^2}}{\sqrt{\left(\frac{\partial f}{\partial x}\right)^2 + \left(\frac{\partial f}{\partial y}\right)^2 + \left(\frac{\partial f}{\partial z}\right)^2}}$$

Therefore the second order analytic signal amplitude is give by,

$$As_2 = \sqrt{\left(\frac{\frac{\partial f}{\partial x}\frac{\partial^2 f}{\partial x^2} + \frac{\partial f}{\partial y}\frac{\partial^2 f}{\partial x \partial y} + \frac{\partial f}{\partial z}\frac{\partial^2 f}{\partial x \partial z}}{\sqrt{\left(\frac{\partial f}{\partial x}\right)^2 + \left(\frac{\partial f}{\partial y}\right)^2 + \left(\frac{\partial f}{\partial z}\right)^2}}\right)^2 + \left(\frac{\frac{\partial f}{\partial x}\frac{\partial^2 f}{\partial x \partial y} + \frac{\partial f}{\partial y}\frac{\partial^2 f}{\partial y^2} + \frac{\partial f}{\partial z}\frac{\partial^2 f}{\partial y \partial z}}{\sqrt{\left(\frac{\partial f}{\partial x}\right)^2 + \left(\frac{\partial f}{\partial y}\right)^2 + \left(\frac{\partial f}{\partial z}\right)^2}}\right)^2 \ldots$$

$$\sqrt{\ldots + \left(\frac{\frac{\partial f}{\partial x}\frac{\partial^2 f}{\partial x \partial z} + \frac{\partial f}{\partial y}\frac{\partial^2 f}{\partial y \partial z} + \frac{\partial f}{\partial z}\frac{\partial^2 f}{\partial z^2}}{\sqrt{\left(\frac{\partial f}{\partial x}\right)^2 + \left(\frac{\partial f}{\partial y}\right)^2 + \left(\frac{\partial f}{\partial z}\right)^2}}\right)^2}$$

APPENDIX B

Matlab code developed during the course of this work. The code for each Chapter is given under the Chapter number.

Chapter 2

```
%%%
```

```
%%%
```

```
clf;
imagesc(tilt);
hold on
contour(tilt,[45,45],'b');
hold on
contour(tilt,[0,0],'k');
contour(tilt,[-45,-45],'r');
h = colorbar;
title(h,'Deg.');
xlabel('X (m)','FontSize',11);
ylabel('Y (m)','FontSize',11);
axis xy equal tight;

%%%%%%%%%%%%%%%%%%%%%%%%%%%%%%%%%%%%%%%%%%%%%%%%%%%%%%%%%%%%%%%%%%%%%%%%%%%%%%%
%%%%%%%%%%%%%%%%%%%%%%%%%%%%%%%%%% END %%%%%%%%%%%%%%%%%%%%%%%%%%%%%%%%%%%%%%
%%%%%%%%%%%%%%%%%%%%%%%%%%%%%%%%%%%%%%%%%%%%%%%%%%%%%%%%%%%%%%%%%%%%%%%%%%%%%%%
```

Chapter 3

```
%%%%%%%%%%%%%%%%%%%%%%%%%%%%%%%%%%%%%%%%%%%%%%%%%%%%%%%%%%%%%%%%%%%%%%%%%%%%%%%
%%%%%%%  Function Profile_R_RW - Calculate the distance to source   %%%%%%%
%%%%%%%  (Cooper, 2014) over profile data                           %%%%%%%
%%%%%%%                                                             %%%%%%%
%%%%%%%  Datasets - step_model_rw.txt                               %%%%%%%
%%%%%%%  By Robert Whitehead - 2015                                 %%%%%%%
%%%%%%%%%%%%%%%%%%%%%%%%%%%%%%%%%%%%%%%%%%%%%%%%%%%%%%%%%%%%%%%%%%%%%%%%%%%%%%%
function Profile_R_RW
clear;
% creating a matrix to image the body
corners(:,1) = [-1000,100,150,250,300,500,550,750,800,2000,2000,-1000];
corners(:,2) = [25,25,75,75,25,25,75,75,25,25,1000,1000];
cnt = 1;
for t = 1 : length(corners(:,1))-3;
    currx = corners(t,1);
    nxtx = corners(t+1,1);
    curry = corners(t,2);
    nxty = corners(t+1,2);
    Y(cnt) = curry;
    for x = currx+1:nxtx-1;
        cnt = cnt+1;
        Y(cnt) = round(interp1([currx nxtx],[curry nxty],x));
    end
    cnt = cnt+1;
    Y(cnt) = nxty;
end
out(:,:,1) = ones(max(corners(:,2)),length(Y)-1);
out(:,:,2) = zeros(max(corners(:,2)),length(Y)-1);
out(:,:,3) = zeros(max(corners(:,2)),length(Y)-1);
for t = 1 : length(Y);
    out(1:Y(t),t,1)= ones(Y(t),1);
    out(1:Y(t),t,2)= ones(Y(t),1);
    out(1:Y(t),t,3)= ones(Y(t),1);
end

% input the data
data = importdata('step_model_rw.txt');
data = data(:,2);
dmax=max(data(:)); dmin=min(data(:));
data=data+(rand(length(data),1)-0.5)*(dmax-dmin)*0.01*0;

% calculation of distance to source
dx = gradient(data,1);
dz = imag(hilbert(gradient(data)));
dxz = gradient(dz,1);
dxx = gradient(dx,1);
dzz = -dxx;
as = sqrt(dx.*dx+dz.*dz);
asxt = dx.*dxx+dz.*dxz;
aszt = dx.*dxz+dz.*dzz;
as2 = sqrt(asxt.^2+aszt.^2)./as;
R = (-1.*as./as2);
```

```
% calculation of Euler solutions
    % By Cooper 2014
n = length(data);
x = 0:length(data)-1;
si = 1;
wsize=11;
w2=floor(wsize/2);
xloc=zeros(n,1); zloc=zeros(n,1);
for point=w2+1:n-w2
 dataw=dz(point-w2:point+w2); dataw=-dataw*(si+1);
 dxw=dxz(point-w2:point+w2);
 dzw=-dzz(point-w2:point+w2);
 grm(:,1)=dxw'; grm(:,2)=dzw';
 sols=grm\dataw;
 xloc(point)=x(point)-sols(1);
 zloc(point)=-sols(2);
end;

% displaying results
figure(1);
clf;
subplot(2,1,1);
plot(1:1000,data,'k');
xlabel('Distance (m)','FontSize',11);
ylabel('Mag (nT)','FontSize',11);
subplot(2,1,2);
image(out(1:100,1002:2000,:));
hold on;
plot(1:1000,-R,'k');
plot(xloc,-zloc,'k+'); hold off;
axis on
hold on
plot([0,100,150,250,300,500,550,750,800,1000],[25,25,75,75,25,25,75,...
    75,25,25],'k','LineWidth',2);
xlabel('Distance (m)','FontSize',11);
ylabel('Distance/Depth (m)','FontSize',11);

%%%%%%%%%%%%%%%%%%%%%%%%%%%%%%%%%%%%%%%%%%%%%%%%%%%%%%%%%%%%%%%%%%%%%%%%%%%%%%%
%%%%%%%%%%%%%%%%%%%%%%%%%%%%%%%%%% END %%%%%%%%%%%%%%%%%%%%%%%%%%%%%%%%%%%%%%
%%%%%%%%%%%%%%%%%%%%%%%%%%%%%%%%%%%%%%%%%%%%%%%%%%%%%%%%%%%%%%%%%%%%%%%%%%%%%%%



%%%%%%%%%%%%%%%%%%%%%%%%%%%%%%%%%%%%%%%%%%%%%%%%%%%%%%%%%%%%%%%%%%%%%%%%%%%%%%%
%%%%%%%  Function Grid_R_RW - Calculate the distance to source      %%%%%%%
%%%%%%%  (Cooper, 2014) over gridded data                           %%%%%%%
%%%%%%%                                                             %%%%%%%
%%%%%%%  Datasets - Box10m.mat etc                                  %%%%%%%
%%%%%%%  By Robert Whitehead - 2015                                 %%%%%%%
%%%%%%%%%%%%%%%%%%%%%%%%%%%%%%%%%%%%%%%%%%%%%%%%%%%%%%%%%%%%%%%%%%%%%%%%%%%%%%%
function Grid_R_RW

spacing = 1;
n = 0; % structural index
% calculating distance to source R - (Cooper, 2014)
data = importdata('Box10m.mat');
[dx,dy]=gradient(data,spacing,spacing);
dz=vertical(data,spacing);
as=sqrt(dx.*dx+dy.*dy+dz.*dz);
[dxdx,dydx] = gradient(dx,spacing,spacing);
[dxdy,dydy] = gradient(dy,spacing,spacing);
[dxdz,dydz] = gradient(dz,spacing,spacing);
dzdz = -dxdx-dydy;
asxt=dx.*dxdx+dy.*dxdy+dz.*dxdz;
asyt=dx.*dxdy+dy.*dydy+dz.*dydz;
aszt=dx.*dxdz+dy.*dydz+dz.*dzdz;
as2=sqrt(asxt.^2+aszt.^2+asyt.^2)./as;
R = (n+1)*as./as2;
figure(1)
imagesc(R,[0,30]);
h = colorbar;
title(h,'m.');
xlabel('X (m)','FontSize',11);
ylabel('Y (m)','FontSize',11);
```

```
axis xy equal tight;

%%%
```

```
Z4val = zeros(size(data));
Z4 = zeros(size(data));
for up = 1 : 30;
    out(:,:,up) = dzz(:,:,up).*up^1.5;
    logic = out(:,:,up)> Z4val;
    Z4val = Z4val.*~logic;
    Z4val = Z4val + out(:,:,up).*logic;
    Z4 = Z4.*~logic;
    Z4 = Z4 + up.*logic;
end
%%%
```

```
dz=vertical(data1,spacing);
asa=sqrt(dx.*dx+dy.*dy+dz.*dz);
[dxdx,dydx] = gradient(dx,spacing,spacing);
[dxdy,dydy] = gradient(dy,spacing,spacing);
[dxdz,dydz] = gradient(dz,spacing,spacing);
dzdz = -dxdx-dydy;
asxt=dx.*dxdx+dy.*dxdy+dz.*dxdz;
asyt=dx.*dxdy+dy.*dydy+dz.*dydz;
aszt=dx.*dxdz+dy.*dydz+dz.*dzdz;
dxasa = asxt./asa;
dyasa = asyt./asa;
dzasa = aszt./asa;
as2_a=sqrt(asxt.^2+aszt.^2+asyt.^2)./asa;
X1 = ((asa).*dxasa)./(as2_a.^2);
Y1 = ((asa).*dyasa)./(as2_a.^2);
Z1 = ((asa).*dzasa)./(as2_a.^2);

% second dataset
data2 = upgrid(data1,spacing,up);
[dx,dy]=gradient(data2,spacing,spacing);
dz=vertical(data2,spacing);
asb=sqrt(dx.*dx+dy.*dy+dz.*dz);
[dxdx,dydx] = gradient(dx,spacing,spacing);
[dxdy,dydy] = gradient(dy,spacing,spacing);
[dxdz,dydz] = gradient(dz,spacing,spacing);
dzdz = -dxdx-dydy;
asxt=dx.*dxdx+dy.*dxdy+dz.*dxdz;
asyt=dx.*dxdy+dy.*dydy+dz.*dydz;
aszt=dx.*dxdz+dy.*dydz+dz.*dzdz;
dxasa = asxt./asb;
dyasa = asyt./asb;
dzasa = aszt./asb;
as2_b=sqrt(asxt.^2+aszt.^2+asyt.^2)./asb;
X2 = ((asb).*dxasa)./(as2_b.^2);
Y2 = ((asb).*dyasa)./(as2_b.^2);
Z2 = ((asb).*dzasa)./(as2_b.^2);

% calculate R,N and Rh
R = asa./as2_a;
N = up./(Z2-Z1)-1;
Rh = sqrt(X1.^2+Y1.^2);

% display results
figure(1);
clf;
subplot(3,2,1);
imagesc(data1);
axis xy equal tight;
h = colorbar;
title(h,'nT','FontSize',11);
text(0.02,0.98,'a','Units', 'Normalized', 'VerticalAlignment',
'Top','FontSize',11);
subplot(3,2,3);
imagesc(N,[0,3]);
axis xy equal tight;
h = colorbar;
title(h,'N','FontSize',11);
hold on;
contour(Rh,0.5,'k');
text(0.02,0.98,'c','Units', 'Normalized', 'VerticalAlignment',
'Top','FontSize',11);
ylabel('Y (m)','FontSize',11);
subplot(3,2,5);
imagesc(R.*(N+1),[0,40]);
axis xy equal tight;
h = colorbar;
title(h,'m','FontSize',11);
text(0.02,0.98,'e','Units', 'Normalized', 'VerticalAlignment',
'Top','FontSize',11);
xlabel('X (m)','FontSize',11);

%%%%%%%%%%%%%%%%%%%%%%%%%%%%%%%%%%%%%%%%%%%%%%%%%%%%%%%%%%%%%%%%%%%%%%%%%%%%%%%
%%%%%%%%%%%%%%%%%%%%%%%%%%%%%%% END %%%%%%%%%%%%%%%%%%%%%%%%%%%%%%%%%%%%%%%%%%
%%%%%%%%%%%%%%%%%%%%%%%%%%%%%%%%%%%%%%%%%%%%%%%%%%%%%%%%%%%%%%%%%%%%%%%%%%%%%%%
```

Chapter 6

```
%%%%%%%%%%%%%%%%%%%%%%%%%%%%%%%%%%%%%%%%%%%%%%%%%%%%%%%%%%%%%%%%%%%%%%%%%%%%%%%%
%%%%%%%  Function FallOff_As - Calculates  S.I over magentic        %%%%%%%
%%%%%%%  sources, using the Analytic Signal fall-off method.        %%%%%%%
%%%%%%%                                                             %%%%%%%
%%%%%%%  Datasets - dyke60_20m.txt and dyke60_30m.txt               %%%%%%%
%%%%%%%  By Robert Whitehead - 2015                                 %%%%%%%
%%%%%%%%%%%%%%%%%%%%%%%%%%%%%%%%%%%%%%%%%%%%%%%%%%%%%%%%%%%%%%%%%%%%%%%%%%%%%%%%
function FallOff_As
clear;

% calculate the analytic signal over both models and distance to source
for cnt = 1:2;
    if cnt == 1;
data = importdata('dyke60_20m.txt');
data1 = data(:,2);
    else
data = importdata('dyke60_30m.txt');
data2 = data(:,2);
    end
data = data(:,2)';
dx = gradient(data,1);
dz = imag(hilbert(gradient(data)));
dxz = gradient(dz,1);
dxx = gradient(dx,1);
dzz = -dxx;
as(:,cnt) = (dx.*dx+dz.*dz);
asxt = dx.*dxx+dz.*dxz;
aszt = dx.*dxz+dz.*dzz;
as2 = (asxt.^2+aszt.^2)./as(:,cnt)';
dxasa = asxt./as(:,cnt)';
dzasa = aszt./as(:,cnt)';
X(:,cnt) = ((as(:,cnt)).*dxasa')./(as2)';
Z(:,cnt) = ((as(:,cnt)).*dzasa')./(as2)';
r(:,cnt) = as(:,cnt)./as2';
end

% calculate N
n = log10(as(:,1)./as(:,2))./log10(r(:,2)./r(:,1));

% display results
figure(1)
clf;
subplot(3,3,1);
plot(data2,'k')
ylabel('nT','FontSize',11);
text(0.02,0.98,'a','Units', 'Normalized', 'VerticalAlignment',
'Top','FontSize',11);
hold on;
plot([0,1000],[0,0],':k');
subplot(3,3,2);
plot(as(:,2),'k');
ylabel('nT/m','FontSize',11);
text(0.02,0.98,'b','Units', 'Normalized', 'VerticalAlignment',
'Top','FontSize',11);
subplot(3,3,3);
plot(sqrt(r(:,2)),'k')
ylabel('m','FontSize',11);
text(0.02,0.98,'c','Units', 'Normalized', 'VerticalAlignment',
'Top','FontSize',11);
ylim([0,40]);
set(gca,'YDir','reverse');
hold on
plot([495,495,505,505],[40,30,30,40],'k');
subplot(3,3,4);
plot(data1,'k');
ylabel('nT','FontSize',11);
text(0.02,0.98,'d','Units', 'Normalized', 'VerticalAlignment', 'Top',...
    'FontSize',11);
hold on;
plot([0,1000],[0,0],':k');
subplot(3,3,5);
plot(as(:,1),'k');
```

```
ylabel('nT/m','FontSize',11);
text(0.02,0.98,'e','Units', 'Normalized', 'VerticalAlignment', 'Top',...
    'FontSize',11);
subplot(3,3,6);
plot(sqrt(r(:,1)),'k');
ylim([0,40]);
ylabel('m','FontSize',11);
text(0.02,0.98,'f','Units', 'Normalized', 'VerticalAlignment', 'Top',...
    'FontSize',11);
set(gca,'YDir','reverse');
hold on;
plot([495,495,505,505],[40,20,20,40],'k');
subplot(3,3,7:9);
plot(n-1,'k');
ylim([0,3]);
xlim([0,1000]);
ylabel('N','FontSize',11);
text(0.02,0.98,'g','Units', 'Normalized', 'VerticalAlignment', 'Top',...
    'FontSize',11);

%%%
```

```
figure(1);
clf;
subplot(4,1,1);
plot(data,'k');
title('a)','FontSize',11);
ylabel('nT');
hold on
plot([0,1000],[0,0],':k');
subplot(4,1,2);
plot(-z,'k');
title('b)','FontSize',11);
ylabel('m');
ylim([-50,0]);
hold on
plot([498,498,503,503],[-50,-20,-20,-50],'r');
xlimits = get(gca,'Xlim');
subplot(4,1,3);
plot(B,'k');
hold on
plot([0,1000],[nup,nup],':r');
plot([0,1000],[nlow,nlow],':r');
title('c)','FontSize',11);
ylabel('N');
ylim([-2,3.5]);

% filter results
B(B>nup) = NaN;
B(B<nlow) = NaN;
filtered = -z.*(~isnan(B));
filtered(filtered==0) = NaN;
subplot(4,1,4);
plot(filtered,'k');
title('d)','FontSize',11);
ylabel('m');
ylim([-50,0]);
xlim(xlimits);
hold on
plot(-r.*2);
plot([498,498,503,503],[-50,-20,-20,-50],'r');
legend('Filtered z','r_N_=_1');
figure(2)
clf;
plot(-z,'k');
ylabel('m','FontSize',11);
ylim([-50,0]);
hold on
plot([498,498,503,503],[-50,-20,-20,-50],'r');
set(gca,'FontSize',11);
h = legend('z','r_N_=_0');
set(h,'FontSize',13);
plot(-r.*2);

%%%
```

Subroutines

```
%%%
```

```
%%%%%%%%%%%%%%%%%%%%%%%%%%%%%%%%%%%%%%%%%%%%%%%%%%%%%%%%%%%%%%%%%%%%%%%%%%%%%%%%
%%%%%%%  Function upward_profile - Upward continues profile data by %%%%%%%
%%%%%%%  a defined distance.                                         %%%%%%%
%%%%%%%                                                             %%%%%%%
%%%%%%%                                                             %%%%%%%
%%%%%%%  By Robert Whitehead - 2015                                 %%%%%%%
%%%%%%%%%%%%%%%%%%%%%%%%%%%%%%%%%%%%%%%%%%%%%%%%%%%%%%%%%%%%%%%%%%%%%%%%%%%%%%%%
function [out,remod] = upward_profile(data,height,spacing)
n = length(data);
if n/2~= round(n/2);
    n = n-1;
    data1 = data(1:n-1);
end
[a,b] = size(data);
if a<b;
    data = data';
end
n = length(data);
if n/2~= round(n/2);
    n = n-1;
    data1 = data(1:n-1);
end
npts = 4^nextpow2(n);
diff = (npts-n)/2;
remod = mean(data(:));
data1 = data;
data1 = data-remod;
paddata = padarray(data1,diff,'replicate');
L = (npts-1)*spacing;
for t = 0 : npts/2;
    f(t+1) = t/L;
end
N = length(f);
for t = 1 : N-2;
    f(t+N) = f(N-t);
end
fdata = fft(paddata);
for t = 1 : length(f);
    fdata(t) = fdata(t)*exp(-2*pi*f(t)*height);
end
out = ifft(fdata);
out = real(out(diff+1:diff+n));
out = real(out +remod);
out = out';
end

%%%%%%%%%%%%%%%%%%%%%%%%%%%%%%%%%%%%%%%%%%%%%%%%%%%%%%%%%%%%%%%%%%%%%%%%%%%%%%%%
%%%%%%%%%%%%%%%%%%%%%%%%%%%%%%%%%% END %%%%%%%%%%%%%%%%%%%%%%%%%%%%%%%%%%%%%%%%
%%%%%%%%%%%%%%%%%%%%%%%%%%%%%%%%%%%%%%%%%%%%%%%%%%%%%%%%%%%%%%%%%%%%%%%%%%%%%%%%
```

REFERENCES

Astrup, J., Hammerbeck, E. C. I., van den Berg, H., 1998 Iron in the Mineral Resources of South Africa (Wilson, M. G. C., Anhaeusser, C.R., (Eds)): Handbook, Council of Geosciences, 16, p. 402-414.

Barbosa, C. F., Silva, B. C., Medeiros, W. E., 1999, Stability analysis and improvement of structural index estimation in Euler deconvolution: Geophysics, v. 64, p. 48-60.

Beukes, N.J., 1986. The Transvaal Sequence in Griqualand West. In: Anhaeusser, C.R., Maske, S. (Eds.), Mineral Deposits of Southern Africa. Geol. Soc. S. Afr., Johannesburg, South Africa, 819–828.

Briener, S., 1973, Applications manual for portable magnetometers: GeoMetrics, Sunnyvale, CA.

Cairncross, B., Beukes, N.J. and Gutzmer, J. (1997). The Manganese Adventure. Assoc. Ore & Metal Corp. Jhb. 236.

Cooper, G. R. J., 2006, Obtaining dip and susceptibility information from Euler deconvolution using the Hough transform: Computers and Geosciences v.32, p.1592-1599.

Cooper, G. R. J., 2012, The semi-automatic interpretation of magnetic dyke anomalies: Computers & Geosciences, v. 44, p. 95-99.

Cooper, G. R. J., 2014, The Automatic Determination of the Location and Depth of Contact and Dykes from Aeromagnetic Data: Pure Appl. Geophys. 171, p. 2417-2423.

Cooper, G. R. J., Whitehead, R. C., 2015, Determining the distance to magnetic sources: Geophysics. In Press.

Durrheim, R. J., Cooper, G. R. J., 1997, Euldep: A program for the Euler deconvolution of magnetic and gravity data: Computers & Geosciences, v. 24, p. 545-550.

Erikson, P. G., Altermann, W., Hartzer, F. J., 2006 The Transvaal Supergroup and its Precursors in The Geology of South Africa (Johnson, M. R., Anhaeusser, C. R., Thomas, R.J., (Eds)), Council for Geosciences. P. 1237-256.

Fedi, M., 2007, DEXP: A fast method to determine the depth and the structural index of potential fields sources: Geophysics, v. 72, p. 1-11.

Florio, C., Fedi, M., Pasteka, R., 2006, On the application of Euler deconvolution to the analytic signal: Geophysics, v. 71, p. 87-93.

Ma, G., U., Du, X., I., 2012, An improved analytic signal technique for the depth and structural index from 2D magnetic anomaly data: Pure Appl. Geophysics, v. 169, p. 2193-2200.

Miller, H.G., Singh, V., 1994, Potential field tilt - a new concept for location of potential field sources: Journal of Applied Geophysics, v. 32, p. 213-217.

Nabighian, M., N., 1972, The analytic signal of two-dimensional magnetic bodies with polygonal cross-section: Its properties and use for automatic anomaly interpretation: Geophysics, v. 37, p. 507-517.

Reid, A. B., Allsop, J. M., Granser, H., Millett, A. J., Somerton, I. W., 1990, Magnetic interpretation in three dimensions using Euler deconvolution: Geophysics, v. 55, p. 80-91.

Salem, A., Ravat, D., Mushayandebvu, M. F., Shijima, K., 2004, Linearized least-squares method for interpretation of potential-field data from sources of simple geometry: Geophysics, v. 69, p. 783-788.

Salem, A., Williams, S., Fairhead, J.D., Ravat, D., 2007, Tilt-depth method: a simple depth estimation method using first-order magnetic derivatives: The Leading Edge, October, p. 1502-1505.

Smellie, D. W., 1956, Elementary approximations in aeromagnetic interpretation: Geophysics, v. 21, p. 1021-1040.

South African Committee for Stratigraphy (SACS), 1980. Stratigraphy of South Africa. Part 1 (Comp. L.E. Kent). Lithostratigraphy of the Republic of South Africa, South West Africa/Namibia, and the Rebublics of Bophuthatswana, Transkei and Venda: Handb. Geol. Surv. S. Afr., 8.

Thompson, D. T., 1982, EULDPH: A new technique for making computer-assisted depth estimates from magnetic data: Geophysics, v. 47, p. 31-37